Platinum and Beyond: Studies of Ultra-heavy Nuclei in the Galactic Cosmic Rays

J. Donnelly

A thesis submitted to
Dublin City University
for a PhD degree

June 2004

Under the supervision of:
Prof. Luke Drury
Dublin Institute for Advanced Studies
School of Cosmic Physics

and

Prof. Eugene Kennedy
School of Physical Sciences
Dublin City University

Dublin Institute for Advanced Studies
Dublin City University

I hereby certify that this material, which I now submit for assessment on the programme of study leading to the award of PhD is entirely my own work and has not been taken from the work of others save and to the extent that such work has been cited and acknowledged within the text of my work.

Signed: Justin Donnelly (JUSTIN DONNELLY)

(Candidate) ID No.: 98970429

Date: 17TH SEPTEMBER 2004

Contents

Abstract

The DIAS-ESTEC Ultra-Heavy Cosmic Ray Experiment (*UHCRE*) flew on board the Long Duration Exposure Facility (*LDEF*) spacecraft in low earth orbit for 69 months. The experiment consisted of a large number (~200) of solid-state nuclear track detector stacks and its objective was to determine the charge abundance spectrum of ultra-heavy ($Z \geqslant 70$) galactic cosmic rays at energies of a few GeV/nucleon. Many hundreds of such ultra-heavy cosmic rays were detected, including 35 actinides ($Z > 88$), making this the largest sample of such data to date.

An overview of our current knowledge of the ultra-heavy cosmic-ray flux is presented in Chapter 1. Charge, energy and isotopic spectra are examined and the clues they present to cosmic-ray origin discussed. Current theories of fractionation of the cosmic-ray source matter during transport and suggested sources of such matter are outlined. The possible insights provided by ultra-heavy cosmic-ray measurements are then suggested. Chapter 2 discusses the configuration of the *UHCRE* and the *LDEF* spacecraft. Solid-state nuclear track detectors, detector processing and data extraction are discussed. Chapter 3 contains information on detector calibration and error analysis and discusses a Monte-Carlo simulation of the apparatus used to corroborate the error estimates. Chapter 4 describes the corrections performed on the raw data for detector bias, detector-processing anomalies and fragmentation within the apparatus. The final charge-abundance spectra are presented. Chapter 5 outlines the conclusions which can be drawn from the data, comparing the results with theoretical predictions and other space-based observations. The experiment's impact on theories of the origin of the cosmic rays is discussed.

Acknowledgments

The LDEF was a immense spacecraft, and while many hands were needed to launch it into the heavens, it also took many to bring it home and transcribe the sagas from its six-year odyssey. In truth, the book you hold in your hands wouldn't exist without the contribution of many people and I would like to extend my thanks to them.

Principal investigators Prof. Alex Thompson and Prof. Denis O'Sullivan for getting the project off the ground. I extend my eternal gratitude to Prof. O'Sullivan for inviting me to DIAS many years ago. Prof. Thompson's hours of advice, guidance and perfectionism helped to wring every last datum from this huge and initially daunting experiment.

My DIAS supervisor, Prof. Luke Drury, for his insight and ingenuity which enabled us to sift flecks of gold from the mud of raw data. With his faith and steadfast support, he provided me with the means and time to continue my research until the project fulfilled its potential. I'd also like to thank him for the rather bracing effect of the disconcerting laughter than floated down from his office on reading my first draft.

The technical assistants who worked so hard at the coal face and without whom I would have nothing to write about: Anne Grace, Eileen Flood, Hilary O'Donnell and Susan Ledwidge.

Jerry Daly for carrying much-needed Victorian-style ingenuity and pride in one's work into the Space Age. One can't help but feel that he is a man whose contribution to knowledge would have been great regardless of the era into which he was born.

Anne Shaw, who generously shared her DIAS office with me on a long-term basis. A graceful Felix to my slovenly Oscar, her kindness enabled me to work and her cheerfulness lit up those times when I wasn't.

The students of DIAS (old and new) who helped make the journey so much more fun and interesting.

Eimhear for the giggles and tachyons, and for balancing my chakras.

Karen for using her project management skills to devastating effect in destroying my thesis-writer's block at the eleventh hour.

Prof. Eugene Kennedy and Prof. Eamonn Cunningham, for their rigorous examination of my work from DCU.

To all the boys – Mr. Teddy, Boris, Tito, Space Panda, Freddie, Jaws, Tom, The Fox, Scratcher, Bill, Betsy and Sachmo – for being so brilliant!

To Catherine for her years of support, patience and energy, whose sails are unfurling for her very own odyssey now. I hope I can return the favour.

To my mother, Eileen.

1. Introduction

Explaining the origin of the galactic cosmic rays is a vast problem. It is difficult to think of another in science which involves time spans of billions of years, distances of galactic (and probably larger) extent, energies across at least 15 orders of magnitude *and* elements from hydrogen to the transuranics.

This chapter has three sections. We begin with a brief history of research into cosmic rays (1.1), then examine what is known about their properties (1.2). Finally, we discuss the currently competing theories of cosmic-ray origin (1.3), a complete explanation of which has eluded us for almost a century.

1.1 A History of Cosmic-Ray Measurements

1.1.1 *Light Cosmic Rays*

The mysterious ionising radiation from space, first reliably evinced by Hess and Kolhörster, was given its current name by Millikan in 1925. By extrapolating the known penetrating power of γ-rays as a function of energy, he claimed the discovery of discrete monoenergetic components in the radiation with energies close to the binding energies of common nuclei. Millikan mistakenly assumed that the cosmic radiation resulted from the Universe's matter formation process, leading him to christen them *cosmic rays*.

The first glimmers of their existence were apparent around the year 1900. The rate at which the leaves of an electroscope converged provided a measure of ionisation and it was found that they discharged even when kept in the dark and away from sources of radioactivity. Though Rutherford later showed that most of the ionisation was due to natural radioactivity, other experiments suggested the presence of a further component. In 1910 a German Jesuit, Fr. Theodor Wulf, conducted an experiment involving the Eiffel Tower. He found that as he ascended the 330 m tall structure, the ionisation fell from 6 ions cm^{-3} to 3.5 ions cm^{-3}. γ-rays were eliminated as candidates since the ions created by γ-rays from the surface of the earth would have halved in intensity at a height of just 80m.

The breakthrough resulted from a series of experiments begun by Hess and Kolhörster in 1912 and 1913 respectively. They both made manned balloon flights; by 1912 Hess had flown to 5 km and by 1914 Kolhörster had reached 9 km. These experiments were often frankly dangerous, and entailed Hess ascending in an open gondola attached to a hydrogen-filled balloon while carrying his electroscopes – all without oxygen.

Hess and Kolhörster discovered that, above about 1.5 km, the average ionisation *increased* with respect to that at sea-level. This was clear evidence of radiation arriving from above the Earth's atmosphere. The radiation's attenuation coefficient implied it was about five times more penetrating than γ-rays from the decay of Radium C. Hess's conclusion came swiftly in 1912:

> *The results of the present observations seem to be most readily explained by the assumption that a radiation of very high penetrating power enters our atmosphere from above, and still produces in the lower layers a part of the ionisation observed in closed vessels.*

FIGURE 1.1 Victor Hess returning from a successful balloon flight.

A seemingly reasonable inference followed: this radiation consisted of γ-rays with slightly more penetrating power than those observed in natural radioactivity and the extra ionisation was caused by elastic scattering with atomic electrons. Hess called this radiation the *Höehenstrahlung* ("high-altitude radiation").

In 1929, Skobeltsyn serendipitously obtained the first pictures of a cosmic-ray track while using a cloud chamber. The same year saw the invention of the Geiger-Müller detector, which allowed the detection of individual cosmic rays. The very fast response time of this instrument also allowed arrival times to be determined very precisely.

1929 was also the year when Bothe and Kolhörster introduced the very important principle of coincidence counting to eliminate background events. The aim was to determine whether cosmic rays were high-energy γ-rays or charged particles. In the experiment, Bothe and Kolhörster used two counters (one placed above the other) to determine whether there were charged particles in the cosmic radiation with sufficient penetrating power to pass through both. The results indicated that such particles were very common. Since it seemed unlikely that separate secondary electrons could be ejected simultaneously into the two detectors, the radiation must be corpuscular in nature. As Bothe and Kolhörster put it:

> *...one can see that a quite exceptional accident must be supposed to happen if two electrons produced by the same γ-ray should display the necessary penetrating power and the correct direction to strike both counters directly.*

Further, on introducing slabs of gold[*] and lead up to 4 cm thick between the coincidence

---

[*] A gold bar was on loan from a local bank and its security was a matter of some concern!

counters, the attenuation of the number of coincidences was measured. It soon became evident that the mass absorption coefficient in the absorbers was in parity with that of the cosmic radiation. Bothe and Kolhörster noted that these particles could account for the bulk of the observed intensity at sea-level and estimated their energies as being between 10^9 and 10^{10} eV.

1.1.2 *Heavy and Ultra-Heavy Cosmic Rays*

Though it is now widely believed that diffusive shock acceleration from supernova remnants powers the galactic cosmic rays (GCRs) up to 10^{15} eV, one of the longest extant mysteries in astrophysics is the exact origin of their matter. Measurements of the ultra-heavy cosmic-ray (UHCR) flux can provide many unique insights. Though the definition of 'ultra-heavy' is somewhat arbitrary, it can be assumed to be $70 \leqslant Z \leqslant 92$ for our purposes. The relative abundance of these nuclei in the GCRs can be used to constrain their possible sites of origin in a number of ways.*

FIGURE 1.2 A heavy cosmic-ray track in a photographic emulsion. (Freier *et al.*, 1948). Note the large number of slow electrons (δ-rays) issuing from the dense filament of silver grains which constitute the track core.

However, nuclear binding energy falls with increasing mass beyond iron, with the result that the actinides ($Z > 88$) are seven orders of magnitude less abundant than iron. Consequently, information on this very important region of the charge spectrum is still scarce, despite decades of research. Indeed, it was only in the late 1940s that the existence of nuclei as heavy as iron was first discerned in the primary radiation. Balloons carried both a cloud-chamber and photographic emulsion plates to heights of about 27 km (90,000') for up to three hours (Freier *et al.*, 1948). The photographic emulsion recorded tracks many times denser than those recorded from fragments in nuclear interactions. In some cases, the range of the particles in the plates was > 20 g cm^{-2}. Freier *et*

---

* The actinides (Z>88) and the elements of the platinum group ($75 \leqslant Z \leqslant 79$) are mainly synthesised by the *r-process*, while the elements of the lead group ($80 \leqslant Z \leqslant 83$) are mainly *s-process* products. Consequently, enrichment of either process in the GCRs may indicate their site of nucleosynthesis. At higher charges, anomalies may be revealed by comparing the actinide/subactinide ratio of the GCRs to those of the current and primordial solar system (obtained from analysis of the solar photosphere and meteorites respectively; Grevesse and Sauval 1998). The relative abundances of cosmochronological pairs such as $_{90}$Th and $_{92}$U can allow one to infer the mean time between their nucleosynthesis and subsequent acceleration. The transuranics can also be used as excellent cosmic-ray 'clocks' since the relative abundances of $_{93}$Np, $_{94}$Pu and $_{96}$Cm fall drastically ~10^7 yr after nucleosynthesis (Blake and Schramm 1974).

1.2 The Cosmic-Ray Flux at the Top of the Atmosphere

1.2.1 *Energy Spectrum*

One of the more striking properties of the cosmic rays is the broad span of their energy spectrum. Particles have been detected from the lowest energies unaffected by solar modulation up to 10^{20} eV nucleon^{-1}. Fig 1.3 shows the differential particle flux for hydrogen, helium, carbon and iron nuclei as a function of particle kinetic energy per nucleon.*

E < 10⁹ eV nucleon⁻¹

At the very lowest energies (below about 60 MeV nucleon^{-1}), there is a rise in the number of helium nuclei. These are the *anomalous cosmic rays*, which are believed to be accelerated in the outer regions of the heliosphere.

Clearly, there is a general attenuation of all four species at energies < 1 GeV nucleon^{-1}. This is because particles traveling from the interstellar medium (ISM) towards the Earth must diffuse against the out-flowing Solar Wind. Disturbances in the interplanetary magnetic field (which vary with the solar cycle) baffle the particles' progress and reduce the flux at Earth. On removing this solar modulation from the proton flux (the solid line in figure 1.3) the cut-off all but vanishes.

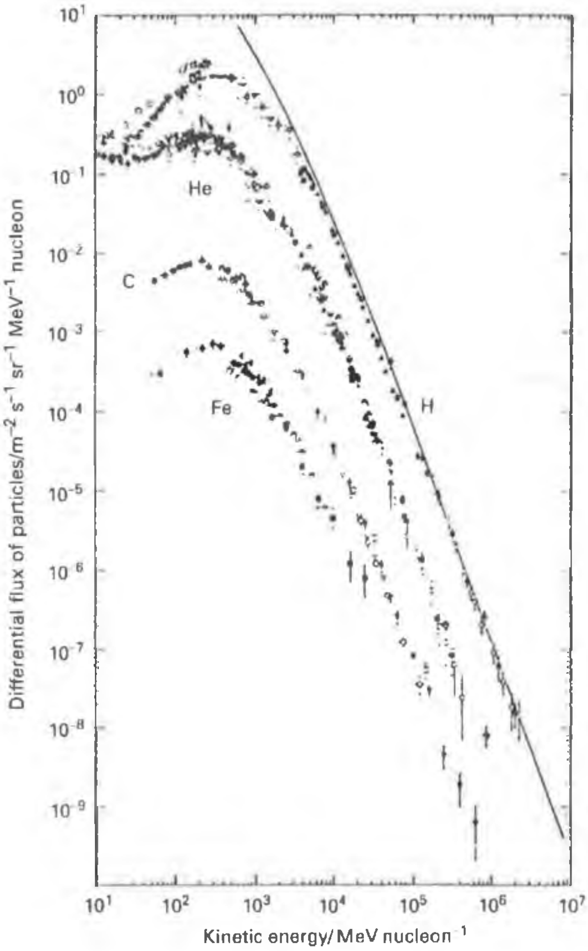

FIGURE 1.3 Differential energy spectrum of H, He, C and Fe cosmic rays as measured above the Earth's atmosphere (Simpson, 1983). The solid line is the unmodulated H spectrum.

One other low-energy component are the *solar energetic particles* or *solar*

---

[*] Since the dynamics of high-energy particles in any magnetic field depend on their magnetic rigidity, different elements (lighter than iron) will be influenced in similar ways. So provided energies are expressed in kinetic energy per nucleon, the relative abundances of the different elements are unaffected by solar modulation and fig 1.4 remains valid.

cosmic rays. These are locally created, originating mostly from Solar flares, coronal mass ejections and shocks in the interplanetary medium. Their composition is similar to that of the GCRs, though very few have energies above 1 GeV nucleon^{-1}.

10^9 *eV nucleon*$^{-1}$ $\leqslant E \leqslant 10^{19}$ *eV nucleon*$^{-1}$

At energies > 1 GeV nucleon^{-1} the differential energy spectra of the various cosmic-ray species approximate power-law distributions of the form: $N(E)dE = KE^{-x}dE$, where E is the kinetic energy per nucleon. A compilation of still-higher energy (10^{14} to 10^{15} eV) results is shown in fig 1.4.

The slope of the energy spectrum from 10^{16} to 10^{19} eV, is well represented by a power law: $N(E) \propto E^{-3.08}$. This is steeper than at lower energies, where the exponent is between -2.5 and -2.7. This 'knee' in the spectrum occurs at about 10^{15} eV. One of the remarkable properties of the knee is the relative smoothness of the transition from a soft to hard spectrum. We will later see that supernova remnants can accelerate GCR particles approximately to this knee. Another explanation is that the knee represents the energy at which cosmic rays can escape more freely from the Galaxy. Greater anisotropy in cosmic-ray arrival directions above this energy would confirm this. At energies above the knee and up to about 10^{16} eV, an anisotropic flux of cosmic rays is observed, which supports the theory.

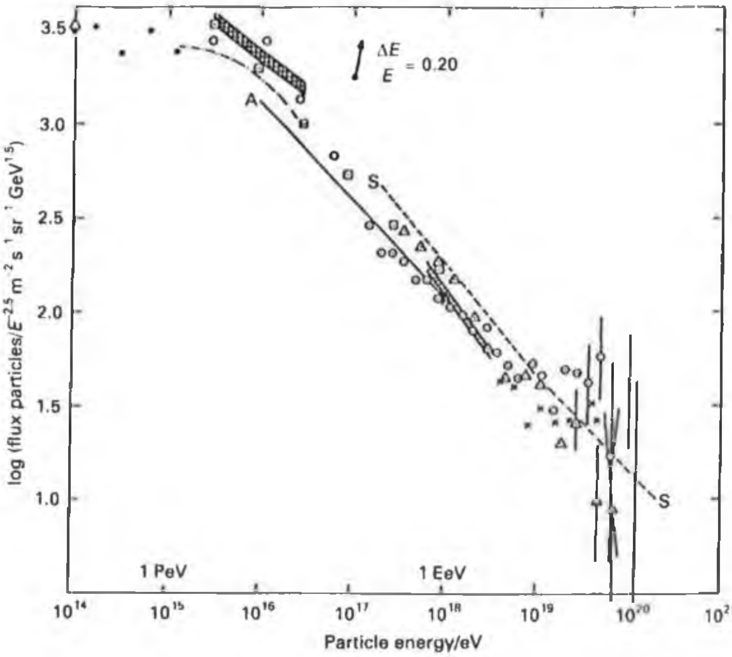

Figure 1.4 A compilation of $10^{14} \leqslant E \leqslant 10^{20}$ eV results from Watson (1985), Hillas (1984), Wdowczyk and Wolfendale (1989). Since the low-energy cosmic rays follow the law $j(E) \propto E^{-2.5}$, the high-energy results are multiplied by $E^{2.5}$ on the assumption that the function $j(E)E^{2.5}$ they follow the same law. This makes the results independent of E. (Source: Longair, 1997)

$E > 10^{19}$ *eV nucleon*$^{-1}$

Small statistics and calibration difficulties make exploring the highest energies problematic. There is some indication of a flattening of the flux again ($\propto E^{-2.5}$) at energies > 2 × 10^{19} eV. At this 'ankle' there is strong anisotropy which lies suggestively close to the direction of the Local Supercluster of galaxies. Above the ankle, some cosmic rays attain enormous energies, in the region of 10^{20} eV[*]. These particles are extremely rare and have arrival rates of approximately 1 km^{-2} sr^{-1} century^{-1}. Their origin is unknown but topological defects (cosmic strings, domain walls and monopoles) have been proposed. A further conundrum arises if we suppose them to be extra-galactic: as yet there is no explanation for how these ultra-high energy particles could survive intergalactic travel through the microwave background radiation that pervades the universe.

Other energy measurements

The energy spectra provide powerful diagnostic tests of cosmic-ray origin models. The ratio of secondary particles (those produced by nuclear interactions in the ISM) to primary particles decreases with increasing energy above a few GeV nucleon^{-1}. If the acceleration was continuous, particles with greater energy would have been traversing the Galaxy for longer and so would have a *higher* secondary-to-primary ratio. Thus continuous acceleration models (like the Fermi mechanism in interstellar clouds) can be eliminated.

Recent *Pioneer* and *Voyager* measurements in the outer heliosphere suggest that the local cosmic-ray energy density is ~2 MeV m^{-3} (Webber, 1987 and 1997; Webber & Mc Donald, 1994) and the amount of matter traversed is inferred to be ~10 g cm^{-2} at 1 GeV nucleon^{-1} (Webber, 1993). These values are roughly twice as large as previous estimates and imply that cosmic rays are energetically much more important in the Galaxy than previously assumed. γ-ray measurements from *Comptel* aboard the Compton Gamma Ray Observer (CGRO) show that 20-30% of this energy is invested in electrons, several times that previously presumed.

The value of the GCR power (~10^{34} W) dramatically shortens the list of astrophysical phenomena which could serve as acceleration mechanisms. The most likely candidate so far is diffusive shock acceleration in supernova remnants, which is effective up to ~10^{15} eV.

Re-acceleration of previously accelerated cosmic rays has been considered as far back as Fermi (1949). If cosmic rays are accelerated in supernova remnant shocks, re-acceleration will take place when previously accelerated particles encounter these shocks. Data from the *Voyager* and *ISSE* spacecraft show that ^{49}V and ^{51}Cr have decayed by ~25-30% in the GCRs, much more than the 10% expected (Soutoul *et al.*, 1998). These results imply an

---

[*] This is about 16 J – a macroscopic amount of energy contained in a single atomic nucleus.

upper-limit on re-acceleration of ~20% in contrast to earlier values.[†] Preliminary *ACE* measurements of ^{49}V and ^{51}Cr and their daughter products ^{49}Ti and ^{51}V indicate only a weak re-acceleration of Galactic cosmic rays. Further data are imminent.

One intriguing final congruence is that between the total energy densities of the $E > 1$ GeV nucleon^{-1} cosmic rays (~2 MeV m^{-3}) and those of the interstellar magnetic field ($\beta^2/\mu_0 \approx 0.2$ MeV m^{-3}), the Microwave Background Radiation (≈ 0.3 MeV m^{-3}) and the local energy density of starlight (≈ 0.3 MeV m^{-3}). Which of these are physical correlations and which mere coincidences is still under debate.

[†] Electron capture decay is only possible following electron pickup after particle acceleration. Some nuclides such as ^{49}V and ^{51}Cr (largely resulting from spallation of ^{55}Fe) are entirely secondary in origin. During their propagation they have a probability for electron re-attachment and subsequent K-capture decay of up to 50% at 200 MeV nucleon^{-1}. Such probabilities are a strong function of energy. Therefore, if cosmic rays are subject to significant re-acceleration, the electron-capture isotopes will have spent some time at lower energies and hence will have suffered significantly more K-capture decay. Simon et al. (1986) examined the cosmic-ray B/C ratio and found that its rigidity dependence was best explained with re-acceleration amounting to a factor of ~2. Re-acceleration, however, ultimately seems to create as many theoretical problems as it solves.

1.2.2 *Charge Spectrum*

A simple count of the cosmic-ray flux arriving at the top of the atmosphere reveals that it is 85% protons, 12% helium nuclei, 1% heavier nuclei and 2% electrons. The elemental abundances of the cosmic rays provide clues as to their origin, acceleration and subsequent propagation to the Earth. Anomalies in the flux are identified by comparing them with 'typical' cosmic abundances and two such sources are commonly used.

The first is the photosphere of the Sun, the brightness of which means that faint absorption lines are readily observable. The relative abundances of the elements are then determined from these lines. The second reference source is meteorites, which have not undergone terrestrial fractionation and so should have chemical abundances similar to the primordial Solar nebula. The chondritic meteorites have chemical abundances similar to those of the Solar photosphere and can fill gaps in our knowledge of the rarer elements.

The elemental abundances in the GCRs at the top of the atmosphere and in the Solar System are shown in fig 1.5 from J.A. Simpson (1983), both given relative to silicon. Measuring the chemical composition above about 10^{14} eV is problematic due to the need to stop the particles in a space-based instrument and obtain a large enough collecting area.

The main features of the cosmic-ray spectrum in comparison to the Solar System spectrum are:

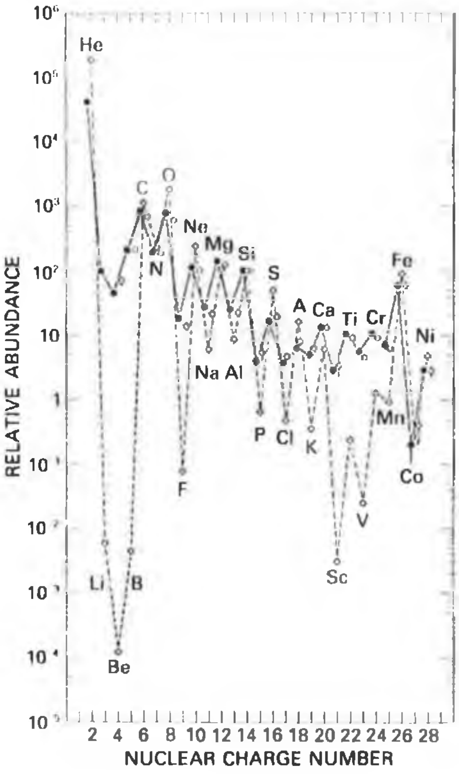

FIGURE 1.5 The abundances of the elements in the GCRs at the top of the Earth's atmosphere (Simpson, 1983). The solid circles are low-energy data (70-280 MeV nucleon^{-1}), the open circles are high-energy data (1-2 GeV nucleon^{-1}) and the diamonds are Solar System abundances. All are normalized to [Si] = 100.

- Hydrogen and helium are underabundant in the cosmic rays relative to the heavy elements by a factor of ~20-30. Since heavier nuclei have much larger cross-sections, this cannot be an artifact of propagation through the ISM. Theories usually maintain that it is caused by fractionation of the source material due to a bias in the acceleration process or its injection mechanism.

- The light elements lithium, beryllium and boron are grossly overabundant in the cosmic rays. These elements are not produced in nucleosynthesis and so presumably originate from spallation of heavier cosmic rays. There is also an excess of scandium, titanium, vanadium, chromium and manganese – elements just lighter than iron ($21 \leqslant Z \leqslant 26$), again probably due to spallation of the iron peak.
- Abundance peaks at carbon, nitrogen, oxygen and iron are present in both the cosmic rays and Solar System.
- An odd-even effect* in the relative stabilities of the nuclei according to atomic number is present in the cosmic rays, though not to as pronounced an extent as in the Solar System.

Though these differences are prominent and real, more remarkable still is the relative similarity of both sets of data, particularly as the second features on the list are due mainly to well-understood spallation during propagation through the Galaxy. See Section 1.2.4 for a discussion on the UHGCR abundances gathered by space-borne experiments.

1.2.3 *Isotopic Measurements*

Studies of isotopic anomalies have proven insightful. To determine the source composition, these data must be corrected at an isotopic level for galactic propagation. One problem with this is the effect of relatively large uncertainties in semiempirical nuclear cross-sections. These uncertainties make any such correction for spallation in the ISM difficult. However, the advantage of isotopic studies is that differential cross sections should be similar for isotopes of the same element.

Some nuclides (e.g. ^{22}Ne, ^{25,26}Mg, ^{29,30}Si and ^{54}Fe) contain comparable amounts of primary and secondary material and source abundances can be inferred from propagation models to eliminate secondary spallation contributions. Another useful aspect of isotopic studies is that some of the species created in spallation reactions are radioactive and hence, can provide information about the transit time of the particles from their site of origin to the Earth. Measurements of secondary-to-primary ratios (e.g. B/C) can indicate the average

---

* There are two reasons why most elements with even Z are more abundant. Firstly, elements with even Z simply have more isotopes. Secondly, nuclei are especially stable if nucleons can "pair up" with their spins in opposite directions. This works for neutrons as well as for protons, but if Z is even, every proton in the nucleus can pair up, while if Z is odd, there must always be an unpaired proton.

amount of ISM material traversed. The cosmic-ray confinement time (and thus mean path length, λ_{esc}*) can then be estimated by measuring the abundance of long-lived β-decay secondary radionuclides.

Such data have recently been measured with increasing accuracy. Until recently, isotopic differences were thought to be widespread between the GCRs and the solar system abundances (with the exception of the ^{22}Ne/^{20}Ne ratio, that shows a well-established excess in the cosmic rays). *Voyager*, *Ulysses* and now *ACE* have challenged this assumption.† *ACE* in particular provides 10 times the statistical accuracy of previous spacecraft measurements and is finally providing sturdy constraints for theoretical work.

The *ACE* data (fig 1.6) have been used to derive GCR source abundances relative to ^{56}Fe for 11 isotopes. They agree well (to within ~20%) with Solar abundances over four orders of magnitude in energy (Weidenbeck *et al.*, 2001). However some differences are present and the more notable anomalies, which will inform our later discussion on cosmic-ray origin, are discussed below.

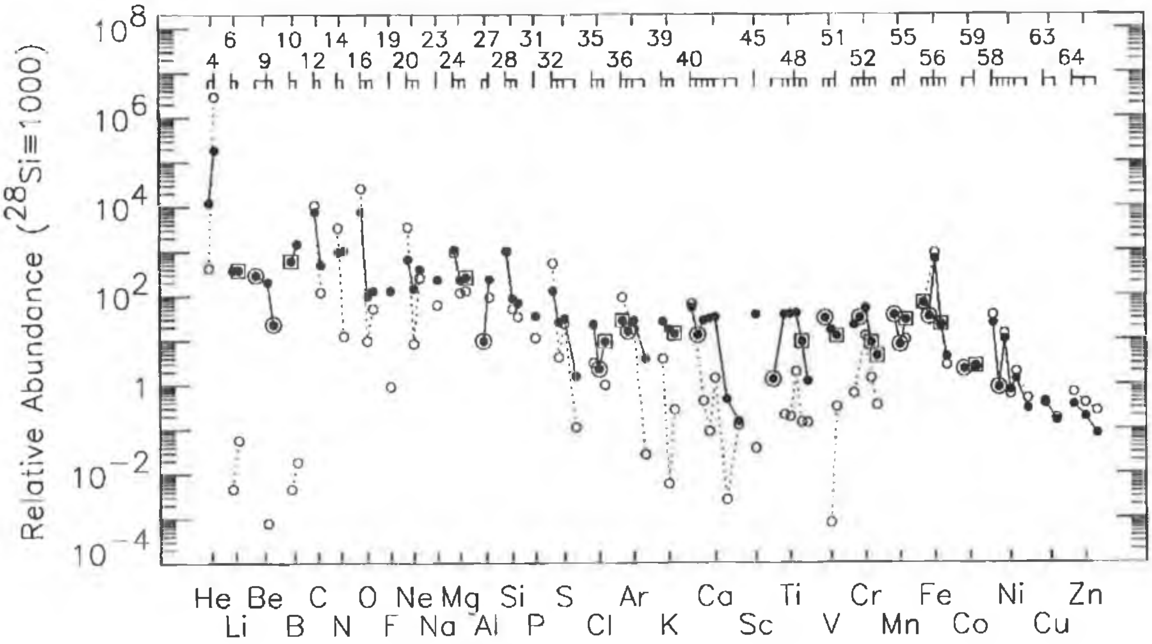

FIGURE 1.6 Relative abundances of low-energy galactic cosmic rays arriving near Earth. Shown are the cosmic-ray composition at ~100-200 MeV nucleon^{-1} as measured by *ACE* (●), the Solar-system composition (○) (Anders and Grevesse, 1989) and cosmic-ray isotopes involved in radioactive decays as parents (◉) or daughters (▣). (Source: Wiedenbeck *et al.*, 2001)

---

* λ_{esc} is related to the mean ISM density traversed by the particles and the mean confinement time by $\tau = \lambda_{esc} / A\, n_{ISM}\, \beta c)$ where βc is the mean GCR velocity, n_{ISM} is the mean ISM density number and A is the mean atomic weight of the ISM.

† *Ulysses* is a joint NASA and ESA project. The spacecraft was launched into a Solar orbit with a high heliographic latitude (~80° north and south). Part of its mission was to measure the isotopic cosmic ray composition at a few hundred MeV nucleon^{-1}. The *Advanced Composition Explorer* (ACE) spacecraft carried a suite of high-resolution mass and charge spectrometers (measuring energies from ~1 KeV nucleon^{-1} to ~1 GeV nucleon^{-1}).

^{59}Ni Electron (or K-) capture decay occurs when a parent nucleus captures one of its own electrons from the (innermost) K-shell and emits a neutrino. However, once an atom is stripped of electrons, as happens during acceleration to GCR energies, it is effectively stable with respect to K-capture decay. This phenomenon can be used to estimate the time between nucleosynthesis of the GCR seed nuclei and their subsequent acceleration. (If the time delay is much longer than the electron-capture half-life, the nuclei will have largely decayed into their daughter products.) Earlier data from the *ISEE 3* (Leske, 1993), *Voyager* (Lukasiak *et al.*, 1997; Webber, 1997) and *Ulysses* (Connell & Simpson 1997) spacecraft hinted at the decay of ^{59}Ni in the GCRs due to the electron K-capture decay $^{59}\mathrm{Ni} \rightarrow {}^{60}\mathrm{Co}$ ($T_{1/2} = 1.1 \times 10^5$ yr), though with insufficient resolution to be definitive.

One of the *ACE* instruments, the *Cosmic-Ray Isotope Spectrometer (CRIS)* has recently detected significant depletion of ^{59}Ni in the GCRs (Wiedenbeck *et al.*, 1999). This implies that the time from nucleosynthesis to acceleration is $>\sim 10^5$ yr. This important result is most pertinent to the debate on cosmic ray origin. If the *ACE/CRIS* data are taken at face value*, models in which cosmic rays attain their energies directly as a result of supernova ejecta ***must be rejected***. The data are, however, consistent with models which imply an old seed material or with models which somehow avoid mixing supernova ejecta with ambient interstellar material for at least $\sim 10^5$ yr before acceleration.

^{22}Ne One of the more striking anomalies in isotopic composition is the GCR $^{22}\mathrm{Ne}/^{20}\mathrm{Ne}$ ratio which is about three times larger than that of Solar material. One proposed explanation is an admixture of material from Wolf-Rayet (WR) stars. According to both theoretical models and observation, the strong stellar winds from these stars are enhanced in ^{22}Ne.

The dominant process of WR formation appears to be mass loss due to radiation-driven winds in massive stars. By removing the stellar envelope, these winds reveal the products of nucelosynthesis and thus become enriched in C and O (with respect

---

* One way to reconcile the *ACE/CRIS* measurements with a short delay between nucleosynthesis and acceleration is to hypothesise that the cross-section for the reaction $^{60}\mathrm{Ni}(p, pn)^{59}\mathrm{Ni}$ has been overestimated. However, this value was extrapolated from measured cross-sections of analogous reactions of neigbouring nuclei so Wiedenbeck *et al.* regard this as unlikely, while stressing the need for direct cross-section measurements in this charge region.

Another possibility is the prompt acceleration of Fe-group nuclei to moderate energies (~150 MeV nucleon^{-1}) where they would be only partially ionised. They would then continue to accrue energy over timescales $\geqslant 10^5$ yr, enough time for K-capture of ^{59}Ni, while preserving the source abundances of the seed nuclei in the GCRs. Since 10^5 yr of travel constitutes only ~1% of the cosmic rays' total path length, the abundances will be preserved over this time period, while giving ^{59}Ni time to decay.

to both H and He and the other heavier elements, which are synthesised deeper in the star and during the subsequent supernova explosion). This enrichment of heavy elements (including ^{22}Ne) has been observed in practice (Willis *et al.*, 1998; Dessart, 2000).

^{10}Be
^{26}Al
^{36}Cl

Radioactive secondaries can survive in the cosmic rays either because of their long half-lives or K-capture suppression after acceleration. The most well-known of these 'cosmic-ray clocks' is ^{10}Be, which has a half-life of 1.5×10^6 years. (See Chapter 5 for a more detailed discussion of cosmic-ray clocks.)

The ^{10}Be, ^{26}Al and ^{36}Cl data from *Ulysses* imply that the cosmic rays travel through a mean interstellar density of 0.25 to 0.45 atoms cm^{-3}. Since the Galactic disc has an average density of ~1 atom cm^{-3}, this result suggests that the cosmic rays spend some time out of the Galactic disc and extend into the (lower density) Galactic halo. If so, these abundances are the best constraints available on halo size. These results also correspond to a mean cosmic-ray confinement time of $\sim 26^{+4}_{-5}$ Myr (Connell, 1998).

Other Nuclides

ACE results show a ^{58}Fe/^{56}Fe ratio ~70 ± 30% over that of the solar system, a factor 1.9 ± 0.3 higher than that reported by *Ulysses*, which otherwise showed values close to solar. Previously reported ^{25}Mg, ^{26}Mg, ^{29}Si and ^{30}Si overabundances in the cosmic rays are not apparent in newer *Ulysses* data. *ACE* data on these isotopes have not yet been published.

In summary, isotopic data have revealed:

- A delay between nucleosynthesis and acceleration of > ~10^5 yr, as suggested by ^{59}Ni K-capture decay.
- A mean confinement time of ~15-26 Myr and propagation through a mean interstellar density of 0.25 to 0.45 atoms cm^{-3}, inferred from ^{10}Be, ^{26}Al and ^{36}Cl data from *Ulysses*.
- A weak (< ~20%) re-acceleration effect, from GCR ^{49}V and ^{51}Cr decay of ~25-30%.

Forthcoming results from *ACE* and further empirical cross-section data from particle accelerators promise more insights in the near future.

1.2.4 *UH Spectra from Spacecraft*

Nuclear interactions in the Earth's atmosphere means that the cosmic rays arriving at the surface are mainly secondary, tertiary and higher order reaction products. To obtain a sample of the primary flux, experiments must be deployed above the atmosphere.

Ariel 6 was launched by a NASA scout rocket on 3rd June 1979 into a near-circular 625 km orbit inclined at 55°. The Bristol University cosmic-ray detector aboard the satellite consisted of a spherical aluminium vessel of diameter 75 cm containing a gas scintillation mixture. This sphere formed a single optical cavity viewed by 16 photomultipliers. Individual particle charges were inferred by separately measuring the gas scintillation and the Cerenkov emission from the plastic shell. This was possible because of the quite different distribution in time of these emissions. Power supply problems meant that the data collection was restricted to 352 complete days at 100% efficiency. This corresponds to an exposure outside the South Atlantic Anomaly and auroral zones of approximately 635 m^2 sr days, allowing for Earth-shadowing and selection effects on particle geometry.

The deconvolved abundances retained the overall overabundance throughout the $60 \leqslant Z \leqslant 80$ region. Three actinide candidates were detected, in comparison to the 0.5 predicted by Brewster *et al.* (1983) for propagated Solar System material.

The *High Energy Astronomical Observatory* (HEAO) was a United States satellite launched on 20th September 1979 into a 495 km circular orbit inclined at 43.6°. The *Heavy Nuclei Experiment* (HNE) on the satellite consisted of six ionisation chambers, one Cherenkov counter and two Pilot 425 plastic radiators viewed by eight photomultiplier tubes. Experiment C2 consisted of five Cherenkov detectors, while HEAO-C3 was designed to measure the abundances of the elements beyond the iron peak and up to the actinides. The resolution of the experiment was insufficient to resolve individual elements and so the data were appropriately binned. In HEAO*'s* case, the binning was quite broad and in ARIEL's even-charge nuclei were presented.

The similarity of the HEAO and ARIEL data has led to their combination to reduce statistical uncertainties (fig 1.7). The HEAO dataset was deconvolved to remove anomalous width and asymmetry in its point spread function. The abundances reported were for charge pairs, the abundance of each even charge being combined with that of the (generally less abundant) odd charge immediately below it.

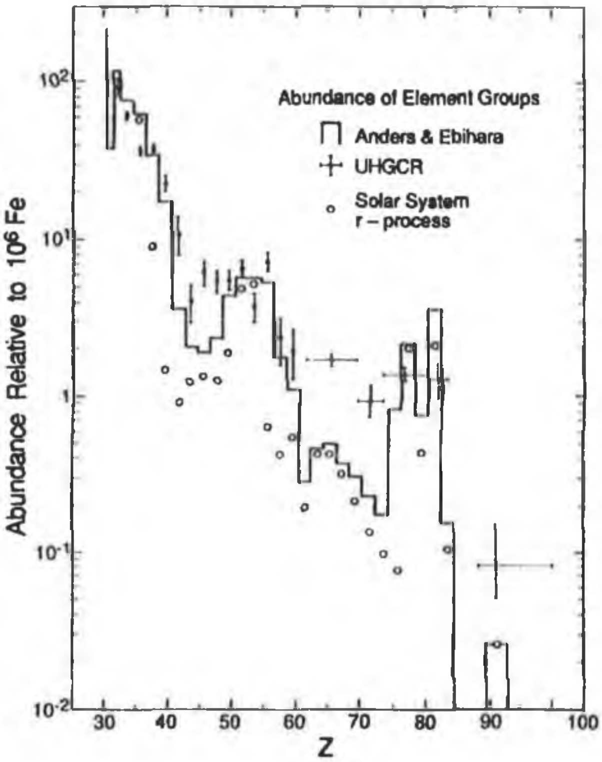

FIGURE 1.7 Compilation of observed UHCR abundances. The Solar system abundances are meteoric (from Anders and Ebihara, 1982). Abundances over Z=60 are normalized to the width of the charge bins. UHGCR represents the combined Ariel VI and HEAO 3 data. (Source: Binns *et al.* 1989)

Significant features of the combined *HEAO* and *ARIEL* spectra are:

- Agreements up to about $Z = 42$, ($50 < Z < 58$) and the ($78 < Z < 84$) peak.
- Again, spallation of elements in these peaks seems to have increased the abundances at lower charges relative to the Solar System elements.
- The abundances of the heavy elements relative to iron are (with some notable exceptions) similar in both the cosmic rays and in the Solar System.

Table 1.1 UHCR relative abundances normalized to Fe (≡ 10^6)

Elements (Z)	**Meteoritic**[*]	**Ariel VI**	**HEAO 3**	**Ariel VI + HEAO 3**
62 - 69	1.697 ± 0.009	7.3 ± 0.9	3.54 ± 0.63	6.9 ± 0.6
70 - 73	0.514 ± 0.006	1.9 ± 0.5	$1.04^{+0.45}_{-0.33}$	1.9 ± 0.4
74 - 80	3.76 ± 0.14	5.7 ± 0.8	4.38 ± 0.71	5.4 ± 0.6
81 - 83	3.86 ± 0.28	2.0 ± 0.6	$1.04^{+0.45}_{-0.33}$	1.6 ± 0.4
>83	0.0472 ± 0.0023	0.4 ± 0.2	$0.06^{+0.14}_{-0.05}$	$0.13^{+0.12}_{-0.05}$

---

[*] Grevesse and Anders (1989).

- HEAO-C3 yielded little evidence of actinides ($89 \leqslant Z \leqslant 103$) while ARIEL VI detected three actinide candidates (of charges 88.5, 93.5 and 97.0). The overabundance of actinides reported by previous experiments was not seen.

Despite the differences, the overall impression is that the cosmic rays have been accelerated from material of similar composition to the Solar System.

The combined results agree with a step FIP-biased Solar System source (to within ±35%) for $32 \leqslant Z \leqslant 60$, but differ significantly for $Z > 60$ elements (with a substantially low "Pb"/"Pt" ratio[*] and substantially high "actinide" abundances). $Z > 60$ GCRs are ~3 times more abundant than expected from a Solar System r-process source (relative to iron). This overabundance is mainly due to Pt-group abundances (actinide enhancement exerting little influence). A pure r-process source would go some way to explaining the $Z > 60$ abundances but fails to address the gross overabundance of the $Z < 60$ elements, $_{38}$Sr, $_{40}$Zr and $_{56}$Ba.

Though there is some evidence of r-process Pt enhancements, s-process Pb depletion is less certain as the Pb Solar abundances are not as well determined. Binns *et al.* (1989) interpret the large GCR Pt/Pb ratio as direct evidence of r-process enhancement at the GCR source. They suggest that although the composition is qualitatively similar to that of the Solar System, there are quantitative differences indicative of a different nucleosynthetic history for material in the cosmic-ray source regions of the Galaxy. (See Section 1.4.3)

The US/Russian *Trek* was an array of glass track-etch detectors deployed on the outside surface of the *Mir* space station in 1991. *Trek* also detected a depleted Pb/Pt ratio (fig 1.8).

The experiment with the largest exposure factor in the ultra-heavy region, however, was the *Ultra Heavy Cosmic Ray Experiment* (UHCRE). During its 69 months aboard the earth-orbiting *Long Duration Exposure Facility* (LDEF) it collected ≃3000 ultra-heavy cosmic-ray events in a solid-state nuclear-track detector array.

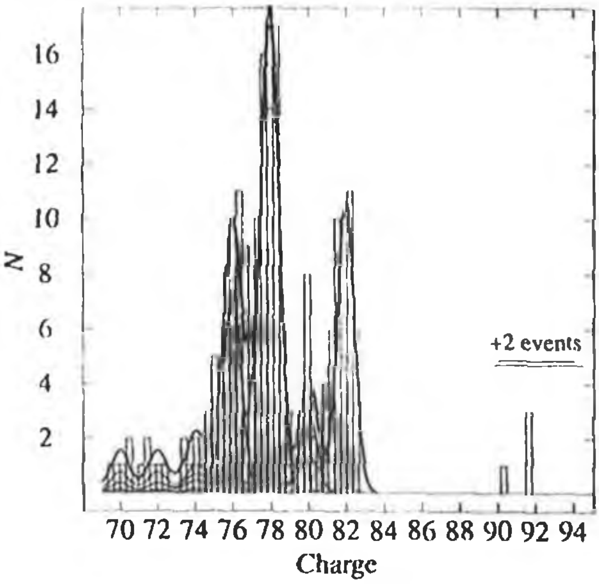

Figure 1.8 Charge spectrum of >0.9 GeV nucleon^{-1} GCRs from the *Trek* experiment, including six actinides (Westphal et al. 1998).

---

[*] Where "Pb" ≡ ($80.5 \leqslant Z \leqslant 83.5$) and "Pt" ≡ ($73.5 \leqslant Z \leqslant 80.5$)

1.2.5 *Overview*

In summary, the more interesting GCR characteristics to have been discovered are:

1) Some elemental deviations relative to the Solar system abundances. The most significant include a paucity of: H and He (by factors of between 20 – 30), N (by a factor of ~10) and O, S, Ar and Kr (by factors of ~4). The cosmic rays also show enhancements in: the ^{22}Ne/^{20}Ne ratio (greater by ~3), Pt and the r-process lanthinides (both enriched by ~2) and (to an uncertain extent) the actinides.[*]
2) A low "Pb"/"Pt" ratio.[†]
3) A delay between nucleosynthesis and acceleration of $> \sim 10^5$ yr.[‡]
4) A mean confinement time of ~15-26 Myr.[§]
5) A mean local energy density of ~2 MeV m^{-3}.[||]
6) A weak (< ~20%) re-acceleration effect.[¶]
7) Traversal of ~10 g cm^{-2} of ISM matter at 1 GeV $nucleon^{-1}$.

Points 1), 2) and 3) pose specific challenges for models which attempt to explain cosmic-ray injection, acceleration and possible fractionation. Point 4) provides a useful constraint on propagation models. Points 5), 6) and 7) indicate that the cosmic rays are energetically more important than previously assumed – more energy is both required of their source and subsequently dissipated in the ISM.

In terms of their elemental composition, the Galactic cosmic-rays and solar system abundances are broadly similar with three major GCR enrichments: i) elements with small first ionisation potential (FIP) or low volatility, ii) ^{22}Ne and iii) nuclei heavier than H and He. The next section discusses models which address these anomalies.

---

[*] Anders and Grevesse, 1989; Grevesse and Sauval, 1998; Binns *et al.*, 1985 and 1989.

[†] Where "Pt" ≡ $(74 \leqslant Z \leqslant 80)$ and "Pb" ≡ $(81 \leqslant Z \leqslant 83)$. See Binns *et al.*, 1985 and 1989.

[‡] Weidenbeck *et al.*, 1999.

[§] See for example, Yanasak *et al.*, 2001; Brunetti *et al.*, 2000; Connell, 1998.

[||] Webber, 1997.

[¶] Soutoul *et al.*, 1998.

1.3 Cosmic Ray Origin

The cosmic-ray spectrum observed at Earth is a palimpsest which is written on at the cosmic-ray source, inside the acceleration mechanism and during the long journey through the Galaxy. Deciphering the earliest imprint, that of the source material, is challenging.

The Energetic Gamma Ray Experiment Telescope (EGRET) on board the Compton Gamma-Ray Observatory (CGRO) observed the distribution of diffuse ~100 MeV γ-ray emission that is produced mainly by cosmic-ray proton collisions with the ISM (fig. 1.9). These collisions produce π^0 mesons which rapidly decay into >70 MeV γ-ray pairs.

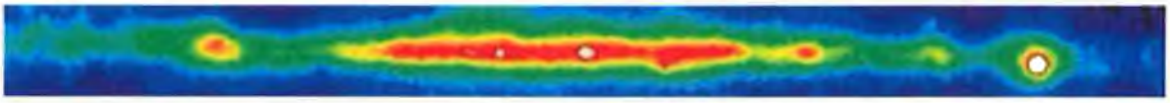

FIGURE 1.9 EGRET observations of the ~100 MeV gamma-ray sky. These gamma-rays are probably due to decaying π^0 particles created by cosmic-ray interactions with the interstellar medium.

Clearly, diffuse γ-ray emission, and thus presumably the cosmic rays, pervade our Galaxy and so play an important part in heating and ionising the interstellar medium, effecting an interstellar exchange of matter and energy and altering the chemical evolution of the Galaxy. In this Section, we will examine the current theories which are advanced to explain their origin.

1.3.1 *Supernova Remnant Shock Acceleration*

The current consensus is that most of the cosmic rays of $E < \sim 10^{15}$ eV are Galactic in origin. Somehow, $\sim 10^{34}$ W must be imparted to these particles and the mere fact that the mechanical power supplied by Galactic supernovae (SNe) is about one order of magnitude greater than this is suggestive. In our Galaxy, SNe occur once every 30 years or so; each one yields $\sim 10^{44}$ J of mechanical energy and ejects several solar masses of material. However, adiabatic losses mean that SNe cannot *directly* power the GCRs. The particles of a supernova (SN) explosion are coupled to the ISM and so are forced to push it outwards, performing considerable 'PdV' work in the process, which makes direct acceleration from SNe energetically untenable.

It is necessary to invoke an acceleration model efficient enough to power the GCRs but which also fractionates the initial injected 'seed' material to explain the anomalies in the

GCR composition. The currently favoured mechanism is diffusive shock acceleration in supernova remnants (SNRs). This has two advantages.

Firstly, the adiabatic energy loss problem can be sidestepped by locating the acceleration not in the SN itself, but in the strong shocks of the subsequent SNR. Most of the explosion energy is processed through shocks when the remnant has a radius of a few parsecs (where the maximum adiabatic loss is reduced by about an order of magnitude). Secondly, collisionless shocks have been observed in the heliosphere with parameters similar to those in SNRs, though these are on smaller time and energy scales and so cannot generate ultra-relativistic particles.

The Fermi mechanism[*] can accelerate mildly supra-thermal particles to ultra-relativistic energies. The fact that this mechanism can work to such low energies creates much less stringent demands on the injection properties of the seed particles. In nonlinear shock acceleration the shock-heated particle distribution has a nonthermal tail that extends to very high energies. Therefore, the process does not require a separate injection mechanism. In this model, then, any nonthermal seed nuclei in the upstream medium will be picked up and accelerated by the shock with essentially no fractionation.

The interactions of the cosmic rays with shocks has been explored in detail (Ellison and Reynolds, 1991) and it now seems quite plausible that fully ~10-20% of the initial energy of the SN explosion can be transferred into accelerated particles (Drury, 1983), as required by the energy arguments.

At energies below about 10^{15} eV, diffusive shock acceleration is largely successful in explaining the origin of the GCR energy.[†] However, there is significantly less concord in models of the origin of GCR *matter*. Recent efforts have addressed cosmic-ray anomalies in terms of injection biases rather than exclusively acceleration effects. Explanations for the anomalies tend to invoke either nucleosynthetic or atomic biases at the source.

---

[*] Fermi (1949) first postulated that diffusion among interacting interstellar clouds could statistically cause particle acceleration. One way to think of this is that the particles are coming into thermal equilibrium with the ISM. It was realised that collisionless shocks in space plasmas could also power diffusive acceleration and transfer the shock's kinetic energy to a non-thermal particle population. Collisionless shocks are those non-linear disturbances which facilitate energy and momentum transfer between particles mediated purely by plasma processes. One appealing aspect of the Fermi mechanism in shock acceleration is that it naturally produces the power law dependence in energy as seen in the GCRs, albeit with a slightly harder spectrum (Drury, 2001).

[†] Most energy is processed through the outer remnant shock, which accelerates only ambient ISM particles. A smaller amount is processed by a reverse shock that propagates back through the supernova ejecta. The result is that between 90% to 99% of the cosmic rays produced are accelerated from the surrounding pre-supernova ISM and the remainder from the supernova ejecta. The implication is that the injected nuclei should have essentially the ISM abudances (which are still, of course, subject to fractionation in the acceleration process). If the UH abundances in the GCRs indicate a pure r-process source (as suggested by Binns *et al*, 1989), this could present a serious challenge to conventional acceleration models.

1.3.2 *Nucleosynthetic Biases*

Early reports of an enhancement of heavy elements in the cosmic rays fueled speculation that discrepancies between cosmic-ray and solar system material could be due to a nucleosynthetic bias at the source (Binns *et al.*, 1989).

For elements of $Z \geqslant 30$, neutron capture is the dominant form of nucleosynthesis. This may be modeled as either the *s(slow)-process* in which the neutron capture rate of a nucleus is low relative to the β-decay rate, or as the *r(rapid)-process* in which neutron capture occurs quickly (~seconds). Because of its long time-scale and synthesis through the β-stability valley, the s-process is incapable of producing those naturally radioactive elements beyond ^{209}Bi, as it is curtailed by falling neutron binding energy and (γ, n) reactions.* Transbismuth elements are thus predominantly r-process.

Both s- process and r-process abundances are sensitive to the physical characteristics of the site of nucleosynthesis, such as temperature and neutron fluence. Thus GCR nucleosynthetic enhancements provide constraints for the physical conditions where the nuclei are synthesised. Locating the s- and r-process sites is important to such an interpretation.

The s-process occurs in asymptotic giant branch (AGB) stars which have degenerate carbon-oxygen cores. A helium-burning shell surrounds the core and supports the star with reactions which release neutrons. S-process elements formed with these neutrons eventually convect to the surface where they may be released in a stellar wind or subsequent supernova explosion.

The r-process occurs in extreme environments when a large flux of neutrons is available, creating transbismuth elements. This process continues up to $A \simeq 260$, when fission occurs. In stars about half of the trans-iron elements are produced by the r-process. At least ten r-process nucleosynthesis sites have been proposed over the last fifty years, falling into two broad categories. Firstly, sites in which elements are produced as primary products directly in a star (e.g. shock or jet ejection of material from neutron-rich SNe cores). Secondly, sites

---

* The quantum-mechanical effects in the s-process impose certain features on the heavy GCR charge spectrum. For certain neutron numbers – $N = 28$, 50, 82 and 126 – neutron-capture cross-sections are much smaller than with neighbouring neutron numbers. These "magic" neutron numbers, then, act as bottlenecks for nucleosynthesis and elements corresponding to them (e.g. $_{88}$Sr, $_{138}$Ba, $_{208}$Pb) will be especially abundant. A similar effect occurs with the r-process nucleosynthesis, but the nuclei created are often highly unstable and β-decay back to the line of stability, which creates peaks at slightly lower neutron numbers than those of the s-process. It is these peaks which contribute significantly to spallation products in the GCRs seen at Earth. S-process peaks are seen at $A = 90$, 138 and 208 while r-process peaks are seen at $A = 80$, 130 and 195.

in which the r-process elements are secondary and which require pre-existing ‘seed’ nuclei which then capture neutrons (e.g. nova outbursts or neutron-star accretion discs).[*]

Spallation from the GCR $_{78}$Pt peak should increase the abundance of its so-called heavy secondary (HS: $70 \leqslant Z \leqslant 73$) and light secondary (LS: $62 \leqslant Z \leqslant 69$) elements. Because the cross-sections with large mass difference are smaller in the LS (eqn. 1 of Shapiro & Silberberg, 1970), we would expect them to have a lower abundance than the HS elements. Binns *et al.* (1989) report that the reverse is the case, with the (predominantly r-process) LS events per unit charge outnumbering HS events by a factor of ~2 in the HEAO data. They also report that the overabundance in the GCR (r-process) Pt-peak detected by HEAO could be fitted by an admixture of heavy ($Z > 60$) r-process material in a medium which is otherwise similar to that of the solar system. Binns *et al.* suggest that this implies an unusual nucleosynthetic history for the cosmic rays.

However, the first and second r- and s-process peaks (up to $Z \simeq 60$) show no particular nucleosynthetic enhancement or deficiency. This, coupled with the lack of an s-process deficiency implies that GCRs do not primarily originate from SN-processed material, since no type of SN synthesises s-nuclei. Explanations for the low “Pb” (s-process) / “Pt” (r-process) ratio[†] which do not require the GCRs to be biased by nucleosynthetic processes are available. These theories organise the cosmic-ray abundances on the basis of *atomic* properties such as volatility and first ionisation potential.

1.3.3 *Atomic Biases*

In the 1970s, it was noticed that the detailed GCR source heavy-element composition could be ordered in terms of the first ionisation potential (FIP)[‡] of its elements (Cassé & Goret 1978; Meyer 1985; Arnaud & Cassé 1985; Silberberg & Tsao 1990). As shown in fig

---

[*] On the basis of β-decay measurements, the r-process probably occurs in a high neutron density ($n_n \geqslant 20$ cm^{-3}) classical (n, γ) equilibrium environment. Furthermore, the observed stellar abundances indicate that the r-process occurs in a single unique environment. The most likely candidate appears to be the ejection of neutron-rich core material from low-mass type II supernovae, but more nuclear and astronomical data are necessary. Tsujimoto & Shigeyama (2001) have determined that the overabundance of barium in the outer layer of the SN1987A ejecta is due to r-process production synthesised during the explosion in the deepest layers of the ejecta. They conclude that 20 $M_\odot$ supernovae are the predominant production site for the r-process elements. The elemental abundance of neutron catpure-rich stars CS 22892-052 and CS 31082-001 are very similar to that of SN 1987A, from which they infer that these stars are born from the ejecta of 20 $M_\odot$ supernovae such as SN 1987A in the early Galaxy.

[†] Where “Pb” ≡ ($80.5 \leqslant Z \leqslant 83.5$) and “Pt” ≡ ($73.5 \leqslant Z \leqslant 80.5$).

1.10, low-FIP elements (FIP ⩽~8.5 eV) are enhanced by a factor of ~5 relative to high-FIP (FIP ⩾~11 eV) elements.

The Solar corona is also known to be overabundant in elements with FIP values < 10 eV, an effect which has been observed in some other cool stars. This fractionation of the solar energetic particles similar to that in the GCRs has lead some to posit coronal mass ejections from sun-like stars[*] as major contributors to the cosmic-ray source material. However, stellar flares are unable to accelerate the bulk of the GCRs up to GeV energies. The supposition is that FIP-biased, supra-thermal material is accelerated to MeV energies and then later preferentially accelerated by a second mechanism (probably SNR shocks) to GeV and TeV energies.

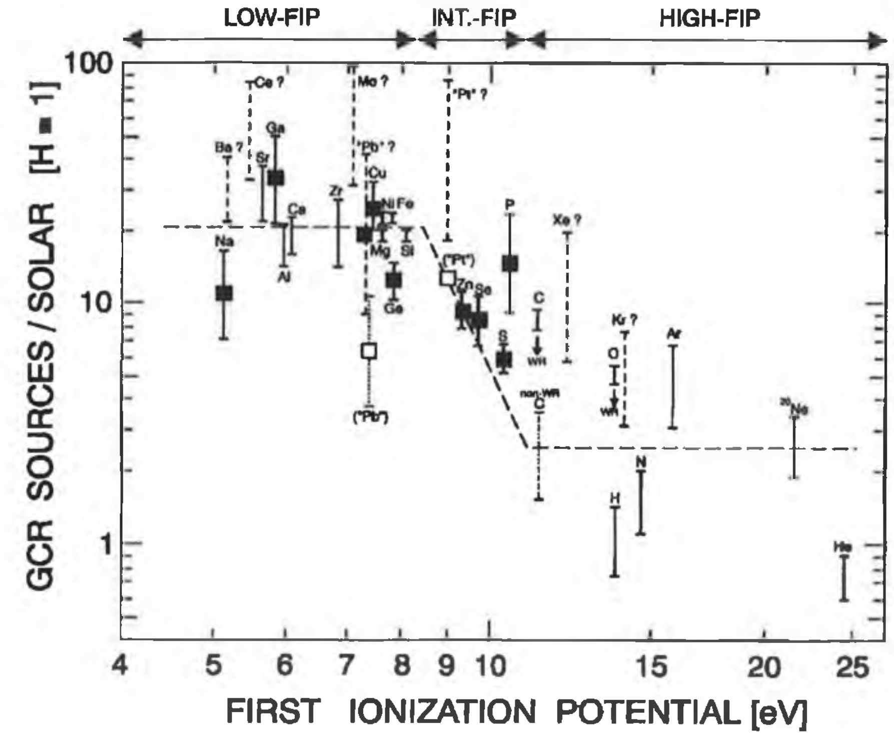

FIGURE 1.10 GCR source/solar abundances vs. FIP in the GeV nucleon^{-1} range. The solar system abundances are mainly from meteorite studies and are normalized to H. Elements denoted by filled squares violate the general FIP-volatility correlation and so can serve as 'clue' elements to determine which parameter fractionates the GCRs. C and O are upper limits as these values may contain surplus contributions from Wolf-Rayet winds. For ^{12}C, a non-Wolf-Rayet source abundance is estimated. UH elements whose abudances relative to iron are not unambigously known are identified by a dashed bar with a question mark. The "Pb" and "Pt" points are plotted arbitrarily where they would fit, assuming a standard FIP pattern (filled squares). Three FIP domains are defined: "low-FIP" (FIP < 8.5 eV), "intermediate-FIP (8.5 eV < FIP < 11 eV) and "high-FIP" (FIP > 11 eV). (Source: Meyer, Drury and Ellison, 1997).

[‡] The FIP is a measure of an element's resistance to being ionised in a ~10^4 K gas (or in radiation of similar energy).

[*] Later-type stars with cool, neutral-H chromospheres.

The GCR ^{22}Ne enrichment[*] cannot come from coronal-gas stars and so a *third* (and unrelated) component is required by this theory. The data imply the presence of a pure He-burning material component, possibly from Wolf-Rayet (W-R) winds. Though the material expelled in a SN explosion is independent of the SN Type, the circumstellar environment is not. Type I SNe (and Type II's with weak winds), will be surrounded by ordinary ISM material, presumably of solar composition. However, the more massive the SN progenitor star, the more important wind ejections become. Significant wind contributions imply that the circumstellar grains will be newly-formed and presumably of a different composition. The most massive W-R stars have winds fierce enough to feed on their He-burning layers and so enrich the circumstellar environment with the products of such reactions (including ^{22}Ne, ^{12}C and possibly ^{16}O). This material can later be accelerated by the W-R star's SNR shock.

However, recent *Ulysses* results (Connell and Simpson, 1997) show little, if any, enhancement of the neutron-rich isotopes of Mg and Si, even though W-R models (Maeder and Meynet, 1993) predict sizeable enhancements (factors of ~1.4 to ~1.9). It remains to be seen if the W-R winds can accelerate the enriched material with enough efficiency to sufficiently contaminate the ISM.

In the FIP model, then, the low temperature of the parent gas (~10^4 K) coupled with the lack of a depletion of the GCR refractory elements locked in grains, implies that the GCR nuclei do not originate in the ISM, but in stellar surfaces.

The FIP model is based on the assumption that only atoms from the *gaseous* ISM are efficiently accelerated. Meyer, Drury and Ellison (1997; see also Ellison, Drury and Meyer, 1997) invert this assumption by invoking an old idea of Epstein's (1980) – the preferential acceleration and sputtering of dust grains. They model the entire process of cosmic-ray injection and acceleration in one mechanism. They assume that the observed FIP-bias in the GCR abundances is actually a *volatility*-based bias. This helps explain specific cosmic ray abundances while taking non-linear acceleration into account.

The more refractory elements in the ISM condense into dust grains which constitute about 1% of the Galactic ISM by mass. These grains are partially-ionised and can be considered to behave as extremely heavy ions. Their large *A*/*Q* (mass-to-charge) ratio means that although they are injected very efficiently[†], they are not accelerated quickly, but

---

[*] This is the only known significant GCR source isotopic anomaly, besides possibly low ^{13}C/^{12}C and ^{18}O/^{16}O ratios and a high C/O ratio.

[†] One early concern with diffusive shock acceleration at SNRs is that the process could actually be *too* efficient and that there might not be enough energy to accelerate many of the particles to relativistic energies. The solution is found when one considers that protons (which dominate the energy budget) have small gyroradii and so are more prone to dissipative processes in the (contd.)

slowly reach energies of about 0.1 MeV nucleon^{-1}. Friction with the ambient gas-phase ISM induces sputtering in the grains, the products of which are swept back into the shock and again accelerated (with little further fractionation) to GeV and TeV energies.

Gas-phase elements (with relatively low condensation temperatures) are exalted directly from the thermal plasma and accelerated to become cosmic rays.

This model then, predicts two components in the GCR composition: a general enhancement of the refractory elements relative to the volatile ones (by a factor of ~10 relative to H; fig 1.11) and b) among the volatile elements, an enhancement of the heavier elements relative to the lighter ones (or, more probably, an *A/Q* enhancement; fig 1.12). These two components may have separate injection and/or acceleration processes, though in their analysis Ellison, Drury and Meyer assume both are subject to the same shock acceleration.

Thus the low H, He and N GCR abundances are explained as *A/Q* (or rigidity) depletions and the high ^{22}Ne, ^{12}C and ^{16}O abundances as contributions from Wolf-Rayet stars. In this model, however, the W-R wind component need not be unrelated to the GCR source nuclei. If the W-R star itself becomes a supernova, the resulting shock will presumably accelerate atoms from its ^{22}Ne-, ^{12}C- and ^{16}O-enriched circumstellar envelope as well as from standard ISM material. This accounts for the over-abundances of these elements in a natural and continuous way.

The GCR source abundances relative to solar used in this discussion derive from measurements made between roughly 1 and 30 GeV nucleon^{-1}. The composition does not appear to change much up to at least 1000 GeV nucleon^{-1} (except possibly for H, see Shibata 1996). The observations for $Z > 60$ have limited charge resolution and so charge groups are usually used. Furthermore, the abundances of (for example) "Pt" or "Pb" relative to Fe have uncertain significance[*]. This is because (in view of the increase in the total nuclear cross-sections with mass) the derived source abundances of these elements with respect to Fe are very sensitive to the propagation parameters, many of which may have large errors.[†] Thus, though Solar values are generally well known, the GCR abundances are known to varying satisfaction.

---

shock. These mechanisms essentially act as a magnetic rigidity filter: particles of high rigidity are preferentially injected into the acceleration mechanism while those of small rigidity (such as protons) are not. The reason is that high-rigidity particles do not react strongly to the small-scale fields and structures that cause this suppression. This *A/Q* fractionation is a key consideration in the volatility-bias model of Meyer, Drury and Ellison (1997).

[*] Here, "Pb" ≡ $(81 \leqslant Z \leqslant 83)$ and "Pt" ≡ $(74 \leqslant Z \leqslant 80)$.

[†] An excess of very short path lengths relative to the generally assumed exponential path-length distribution could yield an observed excess unrepresentative of the source composition.

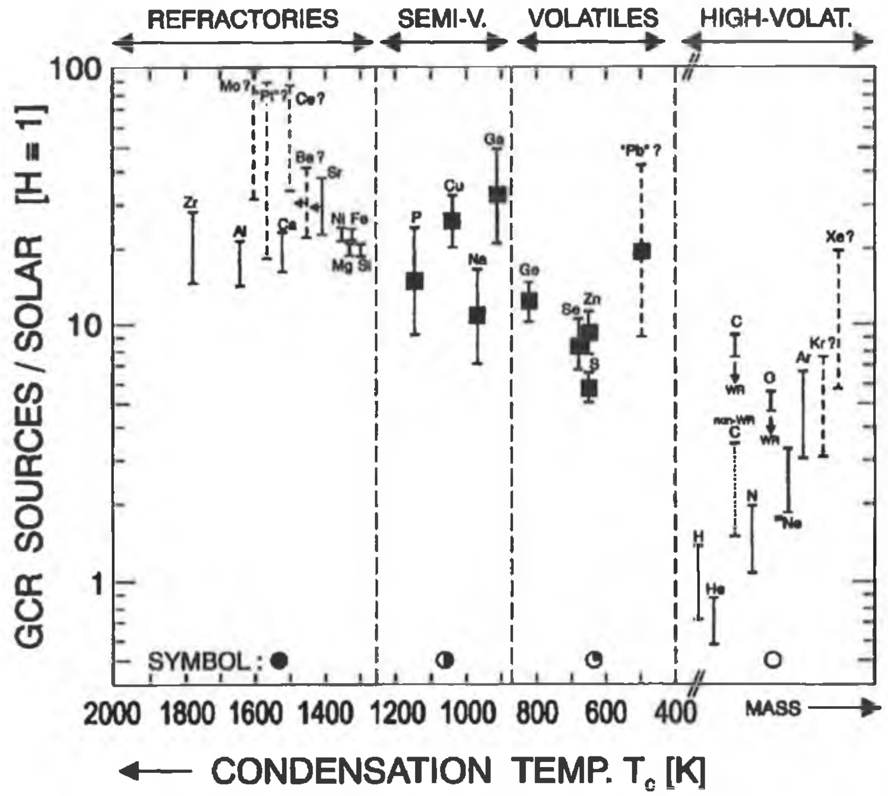

FIGURE 1.11 The same GCR source solar abundances as in figure 1.10, this time plotted against condensation temperature, T_c. The enhancements decrease with increasing T_c, except for the "highly-volatiles". Here, plotting against T_c is not helpful and they are plotted in order of increasing mass. For these elements, the A/Q bias is evident (except for H). O and C are plotted as upper-limits to indicate possible W-R enhancement. The large spread of enhancements in the "semivolatiles" and "volatiles" can also be interpreted as a mass effect. (Source: Meyer, Drury and Ellison, 1997).

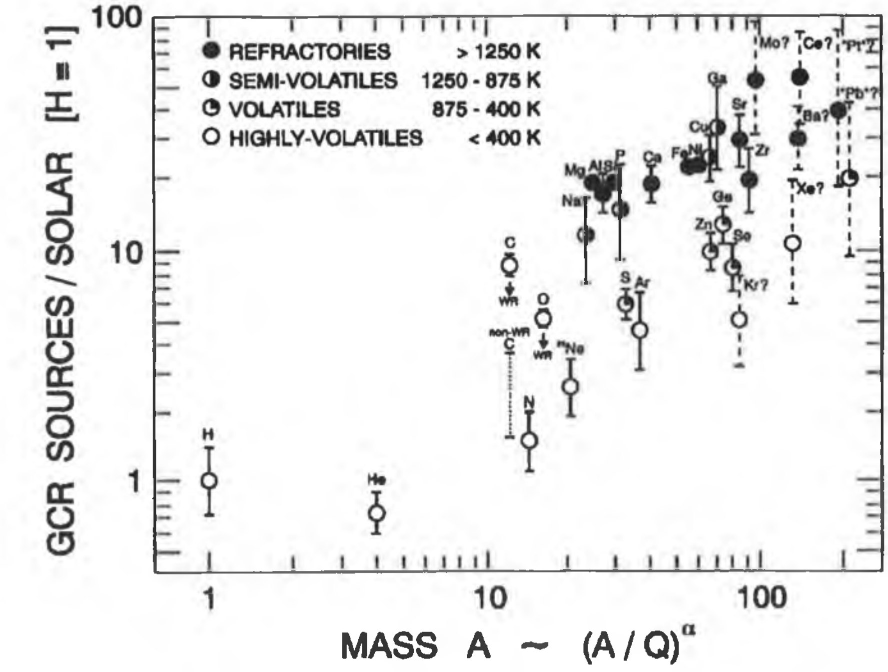

FIGURE 1.12 The same GCR source solar abundances as in figures 1.10 and 1.11, plotted against element atomic mass number, A. The more refractory elements appear generally more enhanced than the volatile ones. The "highly-volatile" GCR source elements seem enhanced roughly $\propto A^{0.8\pm0.2}$ over solar abundances, with the exception of H. This (most likely A/Q) enhancement is not evident in the refractories (which are in any case enhanced overall with respect to the gas-phase or volatile elements). (Source: Meyer, Drury and Ellison, 1997).

An important question is whether the GCR nuclei are, broadly speaking, the flotsam (grains) or jetsam (low-FIP particles discarded from stars) of the Galaxy. Volatility and FIP are, of course, related by chemistry – high FIP elements (hydrogen, non-metals and noble gases) form volatile compounds which condense at quite low temperatures, if at all. Fig 1.13 illustrates the correlation and also shows those elements which violate it – low-FIP volatiles or high-FIP refractories. These 'clue' elements can help determine which type of fractionation has affected the GCR population – FIP or volatility.

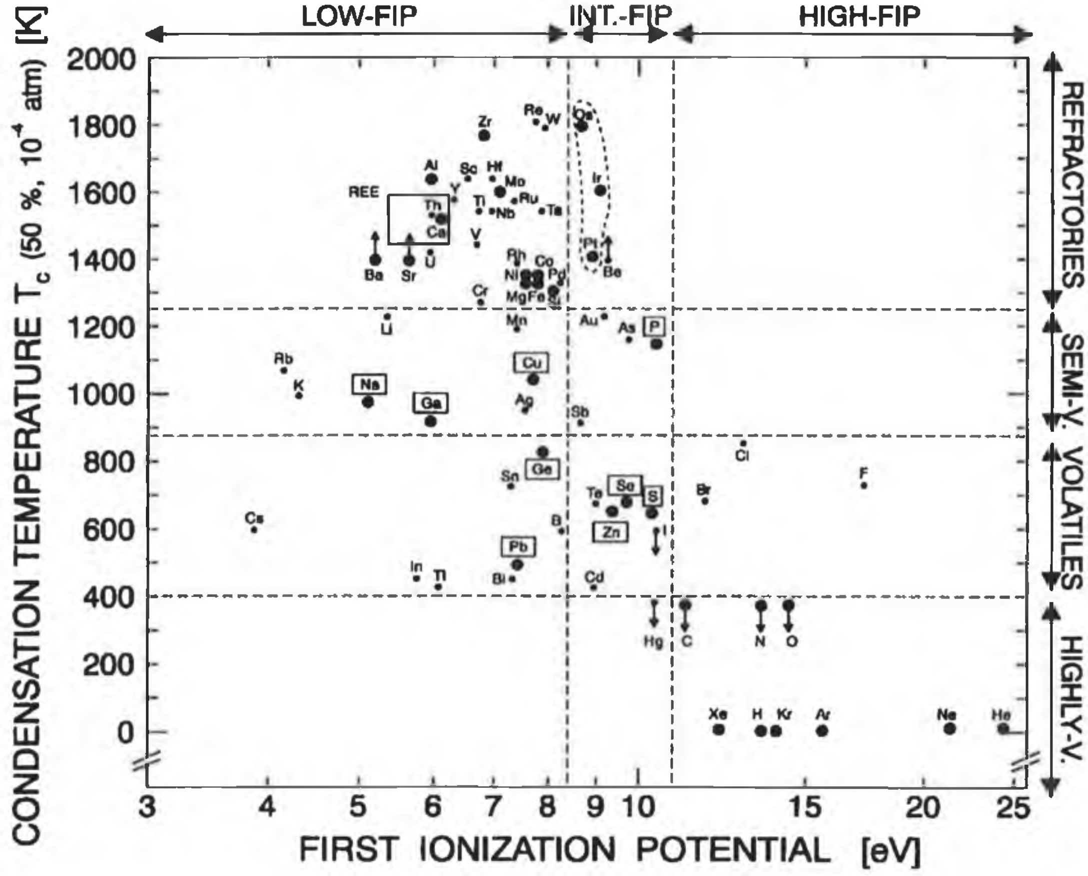

FIGURE 1.13 A cross-plot of the condensation temperature T_c of each element against its FIP. T_c is defined as the 50% condensation temperature of the dominant solid compound formed by the element at a solar initial gas composition of 10^{-4} atm. There are four classes of volatility: "highly volatiles" ($T_c < 400$ K), "volatiles" (400 K< $T_c < 875$ K), "semivolatiles" (875 K < $T_c < 1250$ K) and "refractories" ($T_c > 1250$ K). Large filled dots indicate elements whose GCR source abundances are well known while those enclosed in boxes violate the general FIP-volatility correlation and are useful as 'clue' elements. (Source: Meyer, Drury and Ellison, 1997).

The abundances of nine of these elements are relatively well determined. Of these, five ($_{16}$S, $_{29}$Cu, $_{30}$Zn, $_{31}$Ga, $_{34}$Se) are more or less equally consistent with FIP or volatility (though some initially appear to support the FIP model, these can also be explained as an *A*/*Q* effect). The remaining four – $_{11}$Na, $_{32}$Ge and $_{82}$Pb (low-FIP volatiles) and $_{15}$P (a high-FIP refractory) – are consistent with volatility fractionation.

$_{11}$Na Sodium has a very low FIP (5.1 eV) but is relatively volatile (T_c = 970 K). It seems deficient by a factor of 2.0 ± 0.8 relative to Si (Ferrando 1993; Du Vernois and Thayer 1996). These abundances are excellently measured and indicate that volatility is the more relevant controlling parameter. However, the combination of uncertainty in its spallation cross-sections and the large number of Na secondaries in the GCRs complicates the interpretation.

$_{15}$P Phosphorus is an intermediate-FIP (10.5 eV) semivolatile (T_c = 650 K) element. It seems to be depleted by a factor of 1.5 ± 0.7 (consistent with being undepleted). Though it seems to slightly favour the volatility model, this interpretation has the same caveat as that of Na.

$_{32}$Ge Germanium is a low-FIP (7.9 eV) volatile (T_c = 825 K) which has been observed with adequate statistics and good charge resolution by both the HEAO-C2 and HEAO-C3 experiments. The Ge/Fe ratio seems depleted – 0.57 ± 0.10 of solar values (Lund, 1984; Binns *et al.*, 1989; Binns 1985). The derivation of the source Ge/Fe ratio from the observed one is solid, since the secondary contribution to the observed Ge is minimal and Ge and Fe have similar cross sections. The Ge/Fe ratio is a strong argument in favour of volatility-bias in the GCRs.

$_{82}$Pb Lead is reliably observed both by HEAO-3, Ariel-6 and *Trek*. "Pb-group" elements are mostly low-FIP (~7.4 eV), volatile ($T_{c,\,Pb}$ = 727 K) and primarily s-process while elements in the "Pt-group" are intermediate-FIP (~9 eV), refractory ($T_{c,\,Pt}$ = 1408 K) and r-process. The low "Pb"/"Pt" ratio seems quite well established and interpreting this value as a low s-process abundance seems unlikely given the lack of any such effect in the first and second s-nuclei and r-nuclei peaks. Depending on propagation conditions the FIP model predicts a GCR source enhancement of between ~1.3 and ~2.6 of solar. The GCR source value is about 3.9 ± 1.1 times lower than the FIP prediction, and so indicates a volatility-bias. (Clinton & Waddington, 1993; Waddington, 1996, 1997)

One problem with the FIP proposal is that the dwarf star ejection must survive long enough to encounter SNR shocks while simultaneously avoiding being swamped by other ISM particles accelerated in the shock. The volatility model maintains the advantage of elegance; the same process both fractionates and accelerates the source material in concord with observed abundances.

1.3.4 *Light Element Evolution*

The light elements which are abundant in the GCRs (Li, Be and B) are largely bypassed by stellar nucleosynthesis, and are in fact destroyed rather than produced in stars. Though some of the isotopes of these elements are believed to be primordial in origin (e.g. ^{7}Li, ^{11}B), most are almost certainly products of nuclear interactions in the ISM. In cosmic ray spallation, high-energy protons and helium nuclei collide with C, N and O atoms in the interstellar medium to produce ^{6}Li, Be and B daughter products.[*]

It is assumed that as the Galaxy ages, the incremental increase of heavy SN nucleosynthesis products in the ISM (and thus in the stellar population) will cause a steady increase in stellar metallicity, Z[†]. As a consequence, there is an accumulation of Galactic carbon and oxygen with time. This would make the spallation process more efficient, as H and He GCRs would have a greater number of carbon and oxygen 'targets'. Galactic chemical evolution should, therefore, mean that carbon and oxygen abundances (and so the Li, Be and B production *rates*) will be proportional to Galactic metallicity. In other words, ^{6}Li, Be and B *abundances* will be proportional to $(Z_{\mathrm{Galaxy}})^2$.

Observations have been made to confirm this. The halo phase of the Galaxy corresponds to a metallicity of $< \sim 10^{-1}$ (i.e. in this epoch the Galactic iron abundance is less than 10% that of the current Solar abundance). Galactic halo stars (most easily observed in globular clusters) provide much of our observational data on the early Galaxy. The halo stars observable today are small, metal-poor and roughly as old as the Galaxy. Their compositions should be little changed from the early Galactic epochs.

The observations revealed that for stars of $10^{-3} \leqslant Z \leqslant 10^{-1}$ the Be/Fe abundances rise proportionally with Z (and not Z^2 as expected). If metallicity is taken as a measure of time, the implication is that Be production has been more or less constant throughout the evolution of the Galaxy.[‡] How can sufficient Be be produced in the early Galaxy? It can

---

[*] In actuality, *inverse* spallation is thought to be the dominant effect (i.e. high-energy C and O nuclei interacting with H and He at rest in the ISM). Under inverse spallation, the ^{6}Li, Be and B production rate depends only on the properties of the high-energy 'projectile' particles rather than the ISM 'target' particles (which are largely H and He in the metal-poor early Galaxy). This scenario makes for a more efficient Li, Be and B production process – no energy is imparted to those H or He particles which do not interact with interstellar C or O. Thus in the early Galaxy, the C and O parent nuclei are present not in the ISM, but in the GCRs.

[†] Here, stellar metallicity is normalized to Solar values; i.e. $Z \equiv \mathrm{Fe/H} = (\mathrm{Fe/H})_{\mathrm{star}} / (\mathrm{Fe/H})_{\odot}$.

[‡] Type Ia supernovae were relatively rare in the early Galaxy. During this epoch, most of the iron is thought to have been produced in Type II and Type Ib supernovae, which produce an average of about 0.1 $M_{\odot}$ of iron each, independent of epoch. The implication is that Galactic metallicity increased at a linear rate and so the constant Be/Fe ratio with metallicity could not be due to low iron content of the early Galaxy and so implies a linear production rate for Be.

only be generated in GCR spallation with the ISM, but the Galaxy was C- and O-poor in this era.

Ramaty *et al.* (1998) used these data to surmise that the cosmic rays of the early Galaxy (or at least their C and O) must have been accelerated from freshly-nucleosynthesised matter rather than the metal-poor ISM. They argued that if all the GCRs were accelerated from the ISM, an unacceptably high amount of energy would be needed per supernova to produce the observed Be/Fe ratio at the lowest metallicities (earliest epochs). Their conclusion was that the volatility (grain) and FIP (coronal mass ejection) scenarios are invalid in the early Galaxy without a component of fresh nucleosynthetic matter.

Lingenfelter, Ramaty & Kozlovsky (1998) argued that the GCRs, at least in the early Galaxy, originate from supernovae accelerating their own ejecta, specifically: freshly-formed high-velocity refractory grains.* After this point, the theory resembles the volatility-based scenario of Meyer, Drury & Ellison (1997), namely the acceleration of grains to ~0.1 MeV nucleon^{-1} resulting in atomic sputtering and subsequent acceleration of the resulting suprathermal atoms in the SNR shock.

Furthermore, Lingenfelter *et al.* rejected the possibility of contributions from Wolf-Rayet winds to the C and O population because the presence of these winds is a function of metallicity (Maeder and Meynet, 1994). If one accepts that metallicity is related to Galactic age, this would imply a varying production of C and O (and so Li, Be and B production rates), at odds with the observed constant Be/Fe output.

SNe do indeed eject huge amounts of C and O, as required by the light element data, but these ejecta must somehow reach SN shocks in order to be accelerated. Two possibilities present themselves. Either a) the CRs accelerated by the forward shock are somehow confined and interact in the SNR (which contains a lot of C and O) or b) the reverse shock accelerates material that contains large fractions of C and O. However, Parizot and Drury (1999) show that the required surplus of C and O cannot be accelerated by either the forward or reverse shocks of an isolated SNR.

---

* The rapid optical dimming and simultaneous infrared brightening of the Type II SN1987A (e.g. Moseley *et al.* 1989b) was cited as evidence of dust grain absorption beginning 450 days after the explosion. Lingenfelter *et al.* (1998) have estimated that of the 0.23 $M_\odot$ ejecta which condensed into grains during the first two years after SN1987A, only ~2 × 10^{-4} is necessary to account for the average injection of cosmic-ray metals per supernova.

Lingenfelter *et al.* discuss the ^{59}Ni decay data (see Section 1.2.3) in terms of a false assumption. The ^{59}Co/Ni ratio of 10 ± 3.3% was interpreted (Lukasiak *et al.*, 1997) as excluding, at the 2σ level, the acceleration of fresh SN ejecta less than 3 × 10^4 yr after the explosion. This interpretation assumed that the GCR ^{59}Co resulted solely from the decay of ^{59}Ni and a 2% spallation contribution. Lingenfelter *et al.* dispute the ^{59}Co/Ni interpretation, citing Woosley & Weaver (1995) predict an *equal* production of ^{59}Co and ^{59}Ni during SN nucleosynthesis.

1.3.5 *Superbubbles*

A riposte to the SN ejecta origin model is to *not* accept that stellar metallicity is related to age. Higdon *et al.* (1998) instead posit the acceleration of enriched material within superbubbles.

Most supernovae are not isolated but occur in OB-type stellar associations in the ISM. When several SN explosions occur in proximity in both space and time, a 'superbubble' forms – an area which is surrounded by a shell of swept-up ambient ISM gas. The bubble interior contains a mixture of the ejecta of previous SNe (with a possible wind contribution from massive stars) and some interstellar material. These hot, low-density shells of SN-enriched matter can reach dimensions of several hundred parsecs. A new supernova inside the bubble accelerates those particles which ultimately create Li, Be and B through spallation. In this model, cosmic rays are accelerated by the recurrent (every ~3×10^5 yr) SNR shocks inside the bubble.[*] Acceleration takes place predominantly after 10^5 yr and up to the bubble's lifetime of 5×10^7 yr (to allow the necessary decay of ^{59}Ni).

This theory avoids a slow and simultaneous buildup of light elements (e.g. C, O, and thus Li, Be and B) and metals and implies a discontinuous increase in Li, Be and B due to each supernova. Parizot and Drury (1999)[†] estimate that after about 30 Myr a superbubble will supply ~8×10^4 $M_\odot$ of high metallicity ($Z \simeq 10^{-1}$ $Z_\odot$) matter which mixes with the relatively metal-poor ($Z \simeq 10^{-4}$ $Z_\odot$) ambient ISM. The superbubble will break up and, depending on how well its matter is diluted with ISM material, the metallicity of subsequent stars will vary over about three orders of magnitude and *not as a function of the stellar age*. These stars will therefore have varying metallicities but similar abundance ratios (i.e. those of the parent superbubble). The result is that two stars forming from the same superbubble-processed gas can exhibit different metallicities, depending on the degree of dilution of the high metallicity material. The Be/Fe ratio (for example) will be constant even though metallicity (e.g. Fe/H) varies over a wide range. Seen this way, a large Fe/H ratio will almost always be accompanied by a large Be/H ratio, as the former indicates a small amount of dilution by the (mostly H) ISM. Under this model, the linear

---

[*] The basic idea is to use the collective effort of many SNe exploding close to one another, so that the C- and O-rich ejecta of one of them is accelerated by all subsequent SNe. This should also optimise the production of Li, Be and B since *forward* shocks (which are ten times stronger than reverse shocks) can perfom most of the acceleration.

[†] Note that in the Parizot and Drury model, the accelerated particles are not necessarily identified with the GCRs, but are simply labelled energetic particles (EPs). The volatility-bias mechanism of Meyer, Drury & Ellison (1997) should work similarly inside a superbubble or in an isolated SNR surrounded by standard ISM material.

increase in Be/Fe with metallicity can be seen as a dilution by Fe, rather than an increase in Be.

For most SN explosions inside superbubbles, a well-ordered SNR will not last very long (due to pre-existing magnetic turbulence). Nor will much matter be processed by the shock (in the low-density environment, a 10 parsec sphere will contain only ~ 1 $M_{\odot}$). However, particle acceleration by shock turbulence is still thought to be very efficient (Bykov and Fleishmann, 1992; Parizot, 1998, Higdon *et al.*, 1998).

The superbubble model can account for the current observational constraints arising from the evolution of the light elements. According to the MacLow and McCray (1988) model of superbubble evolution, the bubble interior consists of swept-up ISM with a few percent of material enriched by SN ejecta and W-R stellar winds, in good agreement with the GCR data.

1.3.6 *Summary*

A final caveat on all discussions of cosmic-ray 'anomalies' is to consider the reference abundances against which they are identified. The cosmic rays are relatively young (probably a few tens of Myr) and are not influenced by Galactic chemical evolution, unlike the (~4.6 Gyr-old) Solar system.* The assumption that the local Solar values are somehow 'normal' is motivated mostly by our thorough knowledge of these abundances.

Space-borne instrumentation has improved to the point where one of the larger uncertainties in determining the GCR source abunances is now due to ill-defined isotopic and elemental cross-sections of the nuclei in question. These energy-dependent partial and total cross-sections are vital to models of GCR propagation. Simpson (1998) esimates that current propagation calculations are in error by as much as ±20-30%. These factors limit the precision with which source abundances can be deduced, no matter how accurately the local abundances are known (unless these abundances are measured at energies at which the cross-sections do not vary with energy). There is an urgent need for further cross-section measurements from particle accelerators, particularly for the ultra-heavy and actinide elements.

---

* Previously, it was believed that stellar photospheric conditions (at least for low-mass stars like the Sun) were generally unaffected by the activity in their cores and so would reflect the composition of the primordial nebula from which they formed. Recent models indicate a fractionation of the heavier elements with respect to H as they settle towards the sun's core during its evolution. This means that the proto-solar and current photospheric elemental abundnaces differ. See reviews by Christensen-Dalsgaard (1998; 2002) and Section 1.4.2 of this volume.

It remains to be seen whether GCR composition is representative of the ISM as a whole or merely characterises particular Galactic regions (e.g. superbubbles). Metallicity* is higher towards the Galactic core (a consequence of higher star-formation and SN rates) and Wielen *et al.* (1996) suggest that the Sun actually formed ~ 2 kpc closer to the core than it is now. Ultimately, the anomalous nature or otherwise of the Solar abundances will be determined by improved spectroscopic observations of other stars and the ISM.

The models outlined in this chapter are all models of *matter* origin, since no theory other than acceleration by SNe can yet account for the Galactic cosmic rays' energy. Though each of the theories have their strengths and weaknesses, some become more cogent than others. The *Trek* data (Westphal, *et al.* 1998) which confirm the low "Pb"/"Pt" ratio in the GCRs disfavour a stellar-chromospheric source (i.e. the FIP model) and are equally consistent with a volatility-biased or r-process enhancement model. The superbubble model could be ruled out if a delay between nucleosynthesis and acceleration of much greater than a few tens of Myr (the mean lifetime of these formations) could be established. Minimum GCR 'age' limits (from isotopic *ACE* data) are currently two or three orders of magnitude below this limit.

The observational data are steadily improving, but are still too porous to conclusively support a single model of cosmic-ray origin. However, measurements of the actinide and transuranic abundances can provide a new set of quite strong constraints. Though they cannot address specific nucleosynthetic, FIP or volatility biases (all actinides being r-process, low-FIP, refractory elements), their relative abundances make excellent chronometric pairs. For example, the nucleosynthesis production ratio of $_{96}$Cm/$_{90}$Th is 1.06 (Pfeiffer *et al.*, 1997), but 10^7 yr later most of the $_{96}$Cm will have decayed and the ratio will have dropped dramatically to less than 0.2. A large number of transuranics ($_{94}$Pu or $_{96}$Cm) relative to $_{90}$Th in the GCRs would imply a relatively fresh r-process enhanced source. The Ultra Heavy Cosmic Ray Experiment (UHCRE) recorded the largest ever sample of GCR actinides. We examine the impact of these unique data on theories of cosmic-ray origin.

---

* In practice, [Fe/H] is the principal measurement of metallicity, Z. Stellar metallicity in our Galaxy covers a broad range ($10^{-4} < Z/Z_{\odot} < 3$; McWilliam, 1997) and for its age, $Z_{\odot}$ is ~60% higher than that of the surrounding local neighbourhood. The Sun may be on the iron-rich side of a wide (~3 orders of magnitude) distribution in Galactic metallicity.

1.4 Insights from Ultra-heavy GCR Abundance Measurements

In this section, we outline what can be inferred from measurements of ultra-heavy GCRs.

1.4.1 *Propagation of ultra-heavy GCRs*

A cosmic-ray nucleus will interact with atoms of both the interstellar medium and the detector apparatus itself. The cross-sections of these charge-changing nuclear interactions depend on the projectile type – heavier elements are particularly susceptible. The result is that the charge-frequency histogram of GCRs observed at Earth is distorted from that at the source. Obtaining the cosmic-ray source abundances is thus critically dependent on using accurate cross-sections for the appropriate projecile, projectile energy and target.[*]

The model which is adopted to simulate GCR propagation is also important. The confinement time along a line of sight through the disk of our galaxy is roughly 10^3 years, so evidence of a much longer confinement time (e.g., ~10^7 years) implies a diffusive transport process.[†] The ratio of secondary to primary elements implies that the GCRs have traversed a medium of lower density than that of the average galactic ISM. This indicates that GCR diffusion occupies a halo beyond the disk of the galaxy itself. In the diffusion halo model (DHM) of cosmic-ray propagation, one expects a gradient in GCR density away from the galactic disk, implying a constant infusion of cosmic rays from the disk into the halo.

The DHM competes with the Leaky Box Model (LBM), which is an equilibrium model in which the cosmic-ray sources are held in a confinement volume, are constant in time and have no density gradient in any direction. Thus, the LBM transport process is based not on diffusion but on an invoked leakage process at the (imaginary) boundaries of the confinement volume. The physical size of the confinement volume and the escape mechanism (though related to the CR energy) are not addressed.[‡] Though the DHM is more physically realistic, the LBM is more popular, possibly due to its simpler mathematical structure.

---

[*] For example, the abundance of Pt with respect to Pb can drop by ~50% when projectile energy varies from 1.5 GeV nucleon^{-1} to 4.0 nucleon^{-1} (Waddington, 1996).

[†] This idea is strengthened by the isotropy of the GCRs, that implies that the initial trajectories of the cosmic rays have been scrambled by Galactic magnetic fields.

[‡] Also, though energy loss processes in the ISM are generally acknowledged, reacceleration is not so well accepted even though there are good physical reasons to do so – particles scattering on turbulent magnetic field irregularities will naturally encounter acceleration via 2nd order Fermi processes.

Standard calculations from such models indicate that the source "Pb-group"/"Pt-group" ratio is ~1.65 times higher than that observed at Earth (Binns *et al.*, 1989; Meyer, Drury & Ellison, 1997; Lingenfelter *et al.*, 2003). Uncertainties in propagation parameters, however, mean that this factor could be anywhere between ~1.3 and ~2.6 (Clinton & Waddington, 1993; Waddington, 1996, 1997; Meyer, Drury & Ellison, 1997).

Though cross-sections for some ultra-heavy (i.e. $60 \leqslant Z \leqslant 82$) nuclei have been determined using heavy-ion accelerators, little is known about the cross-sections of the actinides ($Z > 88$). Actinide nuclei have extremely short mean free paths (~1.0 g cm^{-2})[*] and so their observed elemental abundance relative to much lighter nuclei will alter significantly from that at the source.[†]

An absence of transuranic elements in the GCR actinides would simplify actinide propagation, as it would reduce the number of channels for the production of fragments. The only adjustment necessary would then be that for $_{92}$U production of $_{90}$Th, which is expected to be small, since $_{90}$Th posesses only one long-lived isotope (^{232}Th) and most $_{92}$U interactions should remove several neutrons for every proton.

The fact that most actinide interactions will result in fission, precludes the production of secondary actinide fragments and further simplifies GCR actinide propagation. Cherry *et al.* (1994) showed that the probability for fission of a $_{79}$Au nucleus in a composite medium (such as a nuclear emulsion or polycarbonate) is 5% at 0.92 GeV nucleon^{-1}. Though little is known about the fission cross-sections of the actinides, at similar energies the fission probability for $_{92}$U in hydrogen is about 70% (Greiner *et al.*, 1985). Also, since the actinides have simliar interaction cross-sections, they will largely maintain their relative source abundances after propagation through the ISM.

Hence, given the current statistical weight of GCR actinide measurements, the abundances of the GCR actinides *relative to each other* are not strongly affected by propagation.

---

[*] The destruction path-length for Th and U nuclei at 1 GeV nucleon^{-1} is ~0.6 g cm^{-2} in a pure hydrogen environment (Wenger *et al.*, 1999). In the local interstellar gas, this corresponds to a mean propagation time of about 1 Myr (for a typical diffusion mean free path of about 0.3 to 1 parsec; Higdon and Lingenfelter, 2003a). This implies that cosmic-ray actinides travel only 300 to 500 parsecs [$d \sim (\lambda ct)^{-½}$] before succumbing to spallation or fission, and must therefore derive from our own Galactic neighbourhood. There are several OB associations within this distance which should be sites of supernovae within the last few Myr. Lighter-nuclei have propagation times of about 10 or 20 Myr (Yanasak *et al.*, 2001; Brunetti *et al.*, 2000; Connell, 1998).

[†] This situation is further complicated by the paucity of data on actinide cross-sections and fission probabilities (both of which are energy-dependent).

1.4.2 *Reference Values*

There are three types of elemental abundance reference values: "meteoritic", "photospheric" and "Solar System" (or "proto-Solar").[*] "Meteoritic" refers to elemental abundances from type C1 carbonaceous chondrites, "photospheric" refers to spectroscopic measurements of the Sun's photosphere and "Solar System" (or "proto-Solar") abundances refer to those from the Sun at the time of its formation.

Compared with results from photospheric spectroscopy, C1 carbonaceous meteorites are depleted in elements which readily form gaseous compounds (e.g. noble gases, H, C, N and O) and are enriched in elements processed in the Sun (e.g., Li). Otherwise, they have comparable elemental abundances and in previously reported data[†] photospheric and meteoritic abundances were assumed to represent Solar System abundances.

Recent models of the Suns's evolution show that helium and other heavy elements have settled towards the Sun's interior since its formation 4.55 Gyr ago. Thus the photospheric abundances of these heavy elements have fractionated relative to hydrogen (but *not* relative to each other). Proto-Solar abundances are therefore representative of the Solar System's average composition while *contemporary* photospheric abundances are not.

Lodders (2003) has provided updated and comprehensive photospheric and meteoritic elemental abundances, recommended values of which are collated in Table 5.2.

1.4.3 *$_{78}$Pt and $_{82}$Pb Ratios ($70 \leqslant Z \leqslant 87$)*

The relative abundance of elements with Z similar to $_{78}$Pt and $_{82}$Pb provide useful constraints on models of cosmic-ray origin. Elements in the Pt-group[‡] are mainly intermediate-FIP, refractory and r-process, while in the "Pb-group"[§] low-FIP, volatile and primarily s-process elements predominate. Thus an anomalous GCR "Pb-group"/"Pt-group" ratio (relative to Solar values) would show up any nucleosynthetic (s- or r-process) or atomic (FIP or volatility) bias in the source abundances. This ratio is more enlightening than (for example) the Pt/Fe or Pb/Fe ratios as it is relatively unaffected by interstellar propagation.

---

[*] The term "cosmic" abundances, used in older literature to denote Solar System abundances, is avoided here.

[†] Specifically, Cameron (1973, 1982), Anders & Ebihara (1982), Anders & Grevesse (1989) and Grevesse & Sauval (1998).

[‡] Where "Pt-group" ≡ ($73.5 \leqslant Z \leqslant 80.5$).

[§] Where "Pb-group" ≡ ($80.5 \leqslant Z \leqslant 83.5$).

Fowler *et al.* (1987) and Binns *et al.* (1985) have measured GCR abundances with the *Ariel 6* and *HEAO C3* experiments respectively. Binns *et al.* (1989) combine the samples from both spacecraft to derive a GCR "Pb"/"Pt" ratio[*] at Earth of 0.30 ± 0.08. Westphal *et al.* (1998) report a value of $0.27^{+0.05}_{-0.05}$.

The most prominent findings to date in this charge region have been:

1. An overabundance of Pt, the Pt-secondaries ($62 \leqslant Z \leqslant 73$) and the actinides. Binns *et al.* (1989) claimed that the Pt and Pt-secondaries were best fit by a predominantly r-process source with a step FIP fractionation. Pt elements are primarily the result of one or more r-process events, which would cause general r-process enhancement in the GCRs of this charge region. Binns *et al.* suggest an admixture of heavy ($Z > 60$) r-process material in a medium otherwise similar to that of the Solar System. However, while invoking such an r-process enhancement fits the data above $Z = 60$, it does not fit that of the lower charges.

2. An apparent underabundance of Pb ($81 \leqslant Z \leqslant 83$). A difficulty with interpreting this is that the Pb-group abundances are not as well-determined as those of the Pt-group. Grevesse & Meyer (1985) suggest that the photospheric abundance of Pb is about 0.63 of the standard meteoritic abundances (Anders & Ebihara, 1982).[†] If this is true, the observed GCR Pb abundances are in agreement with those of the Solar photosphere, but *not* with meteoritic abundances. The smallest recorded Solar System Pb abundance comes from the photospheric data of Grevesse & Meyer (1985) or Anders & Grevesse (1989). A Pb Solar System abundance over this value would indicate (from the data of Binns *et al.*) depletion of Pb in the GCRs.

Binns *et al.* assert that the low Pb/Pt ratio in the GCRs is more likely to indicate a Pt enhancement relative to Fe, than a Pb deficiency. This conclusion is based on the measured Pt/Fe and Pb/Fe ratios. The problem with this assumption is that (in view of the increase in the total nuclear cross-sections with mass) the derived source abundances of these elements with respect to Fe are very sensitive to the propagation parameters, many of which may have large errors.[‡]

---

[*] Here, "Pb"/"Pt" = $(81 \leqslant Z \leqslant 83) / (74 \leqslant Z \leqslant 80)$.

[†] See Section 1.4.2.

[‡] For example, an excess of very short propagation path lengths relative to the generally assumed exponential path-length distribution could yield an observed excess unrepresentative of the source.

The *HEAO 3*, *Ariel 6* and *Trek* experiments (Binns *et al.*, 1985, 1989; Westphal *et al.*, 1998) observed "Pb"/"Pt" values about 3.9 ± 1.1 times lower than Solar, implying a *source* value about 2.4 ± 1.3 times lower than Solar.[*] However, based on a plain Solar source, one would expect a FIP-biased "Pb"/"Pt" value ~1.6 times *higher* than Solar.[†] The measured value is therefore 3.9 ± 2.0 times *lower* than a FIP-biased source would suggest. With a FIP-bias rendered unlikely, other theories which explain the differences between Solar System and GCR composition must be examined. The remaining theories compatible with the GCR's low Pb/Pt abundance are either nuclear (i.e. an enhancement of r-process components like Pt)[‡] or atomic (i.e., a paucity of volatile elements in interstellar dust grains).[§]

The number of ultra-heavy (i.e., $Z > 70$) events collected by *HEAO C3* and *Trek* amounted to just a few dozen and 192 respectively. The UHCRE would collect many hundreds of ultra-heavy GCRs (with a commensurate improvement in statistical significance) and provide the best estimate yet of the relative abundances of Pb and Pt in the cosmic rays.

1.4.4 *Actinide Ratios ($89 \leqslant Z \leqslant 103$)*

Various theories have been advanced for the apparent overabundance of actinides in the cosmic rays. It may be due to an overall r-process enhancement, indicating that the source material could be freshly-nucleosynthesised SN ejecta. It may also be an acceleration bias wherein easily ionised (i.e., low-FIP) elements are more readily accelerated, or one in which refractory elements found in interstellar dust grains are preferentially accelerated.

The cosmic-ray actinide ratios cannot address these models directly (since all actinides are r-process, low-FIP and refractory). However, due to their radioactive nature, their relative abundances can provide unique information about the age of the cosmic-ray matter; a young age would indicate a fresh (probably r-process enriched) component while an older age would imply origin from the ordinary interstellar medium. Thus, the main use of GCR actinide abundance ratios is to "date" the cosmic-ray matter.

---

[*] Adjusting for propagation, the "Pb"/"Pt" ratio is believed to be ~1.6 times higher at the CR source than at Earth (Binns *et al.*, 1989; Meyer, Drury & Ellison, 1997; Lingenfelter *et al.*, 2003).

[†] Pb elements are all low-FIP (~7.4 eV) while Pt elements are mostly intermediate-FIP (~9 eV).

[‡] As in Binns *et al.*, 1985, 1989.

[§] Meyer, Drury & Ellison, 1997.

To do this requires knowledge of r-process elemental production yields and their evolution with time. If these initial abundances (and radioactive decay parameters) are accurately known, the GCR actinide abundances can be used to estimate the time elapsed between nucleosynthesis and acceleration. This helps determine whether the cosmic rays were accelerated out of fresh supenova ejecta, superbubble material or old, well-mixed galactic matter.

GCR actinide measurements can also be compared with the abundances of lighter nuclei, as in the propagated actinide/Pt-group or actinide/"sub-actinide" ratios reported by Westphal *et al.* (1998) and Brewster *et al.* (1983) respectively.

Of all the actinide isotopes, only seven have lifetimes which exceed 10^6 yr and which are therefore likely to be detectable in the GCRs (Table 1.2). As discussed earlier, these nuclei must be nucleosynthesised through the r-process, within an environment of high neutron density. However, direct r-process production accounts for only a small fraction of the later abundances of the most stable actinides, which depend on heavier α-decaying parent nuclei.

Table 1.2 The Actinide isotopes with significant half-lives

Isotope	**Half-life (Myr)**
^{232}Th	14, 100
^{235}U	704
^{236}U	23
^{238}U	4,470
^{244}Pu	81
^{247}Cm	15.6

Initial r-process production abundances must be calculated from theoretical models. Subsequent decay can then be simulated by chemical evolution models and these predictions can be compared to GCR measurements to help date the cosmic ray material in the following ways:

$_{90}$Th and $_{92}$U[*] The relative abundance of chronometric pairs such as $_{90}$Th and $_{92}$U can provide an estimate of the time elapsed since their nucleosynthesis. Goriely *et al.* (2001) have calculated a U/Th r-process yield of 0.96.

Lingenfelter *et al.* (2003) derive an r-process U/Th yield of ~0.86.[†] They have also calculated the evolution of this ratio (and others) after nucleosynthesis (see Fig 1.14). Note that $_{92}$U/$_{90}$Th initially rises due to the rapid decay of transuranic isotopes. However, it drops again when the $_{92}$U isotopes begin to decay (~10 Myr after the r-process event). In agreement with other models (e.g. Blake and Schramm, 1974) Lingenfelter *et al.* predict that $_{92}$U/$_{90}$Th will then remain above unity until approximately 1 Gyr after the initial nucleosynthesis.

Transuranics After an r-process event, the abundances of $_{93}$Np, $_{94}$Pu and $_{96}$Cm are each initially comparable to (or greater than) that of Th.[‡] The transuranics are excellent nucleosynthetic 'clocks' because about 10^7 yr after nucleosynthesis, their abundances plummet dramatically relative to $_{90}$Th and $_{92}$U (Blake & Schramm, 1974; Goriely & Arnould, 2001). About 10^9 yr after nucleosynthesis, all three of these elements have essentially vanished and $_{90}$Th becomes more abundant than $_{92}$U. Detection of elements beyond $_{92}$U in the GCRs (most likely $_{94}$Pu or $_{96}$Cm) would therefore imply the presence of freshly synthesised material.

The unambigous presence of $_{96}$Cm ($t_{½} \approx 10^7$ yr) would also suggest the presence of younger material in the GCRs. If the material is sufficiently fresh, then the observed abundances of the actinides would reflect the primary nucleosynthetic yields of the r-process. These yields are very important, as they are unmeasured (and poorly constrained) parameters in cosmochronological models which aim to discover the age of the Galaxy itself.

---

[*] The astrophysical importance of the GCR abundances of these elements has been additionally enhanced by the observation of Th in some very metal-poor stars and U in one of them (Sneden *et al.*, 1996; Cayrel *et al.*, 2001). These measurements make plausible a nuclear-based evaluation of the age of individual stars other than the sun.

[†] Thielemann *et al.* (1983) report calculations of ^{238}U / ^{232}Th (i.e. isotopic) r-process production ratios varying from approximately 0.52 to 0.71 depending on the mass law used and the β-delayed fission assumptions made.

[‡] Most recent r-process calculations predict, for example, Cm/Th yields of ~1 (Pfeiffer, 1997).

To date, a total of only nine cosmic-ray actinides have been detected. *HEAO C3* detected three and *Trek* six (two of these were of indeterminate charge, three were U and one Th). The UHCRE's exposure factor means that it should have collected dozens of actinides, enough to form a rudimentary actinide Z spectrum.

A note on r-process production yields:

Recent calculations of r-process yields in core-collapse supernovae* (Kratz *et al.*, 1993; Pfeiffer *et al.*, 1997) use the Thomas-Fermi plus Strutinsky integral and quenching (ETFSI-Q) nuclear mass model. These models predict values comparable to those found in metal-poor halo stars (e.g. Cowan *et al.*, 1999 and 2002) and to Solar System r-process abundances. Goriely & Arnould (2001) have examined 32 different combinations of models for the calculation of nuclear masses, β-decay rates, β-delayed probabilities and fission processes. Their collated results show that the important isotopes (^{232}Th, ^{238}U and ^{235}U) are within 5 to 10% of the ETFSI-Q model. The predicted variation of elemental abundances after a single r-process event is shown in fig 1.13.

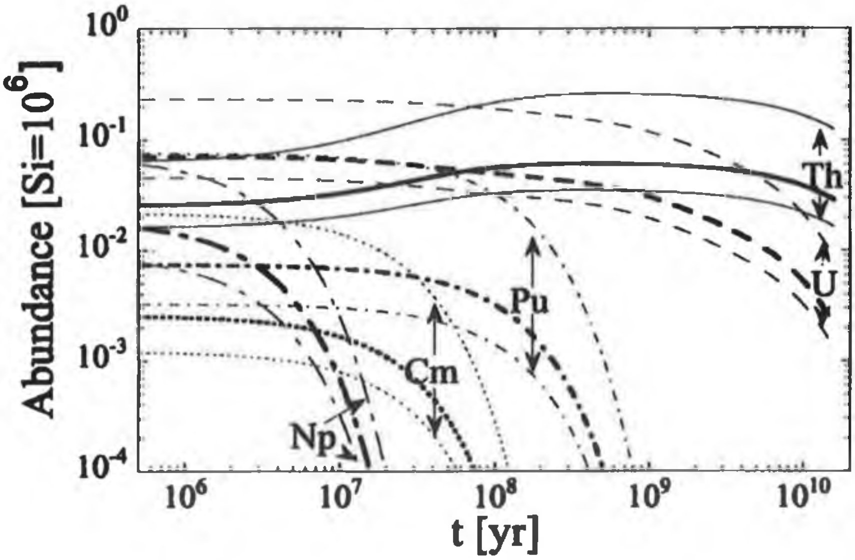

FIGURE 1.13 Theoretical evolution of actinide abundances after an r-process event at $t = 0$ (Goriely & Arnould, 2001).

The authors acknowledge that their model is problematic due to uncertain astrophysical and nuclear-physics parameters. Astrophysically simplifying the model seems unavoidable given the lack of knowledge about the site(s) of the r-process and the physical conditions

---

* The r-process nucleosynthesis yields from core-collapse supernovae are believed to be independent of the mass of the supernova progenitor star.

therein. Compounding the astrophysical uncertainties, the required nuclear properties[*] of most nuclei involved in the r-process remain unknown. Goriely & Arnould conclude by noting that even obtaining reliable error bars on r-process actinide production remains an elusive goal and that much work still lies ahead.

Lingenfelter *et al.* (2003) have used calculated r-process yields from core-collapse supernovae[†] to determine actinide abundances averaged over different time intervals. They then used a standard Galactic chemical evolution model for the actinides (e.g., Fowler, 1972; Thielemann, Metzinger & Klapdor, 1983) to predict actinide abundances in the present interstellar medium. They assert that since the bulk of core-collapse supernovae occur in the supernova-active cores of superbubbles, the material in these cores should comprise the bulk of the GCR source material. They then calculate U/Th and other actinide abundances expected in the SN-active cores of superbubbles. Finally, they derive expected galactic cosmic-ray actinide ratios from a mix of acceleration sites and SN types (see fig 1.14).

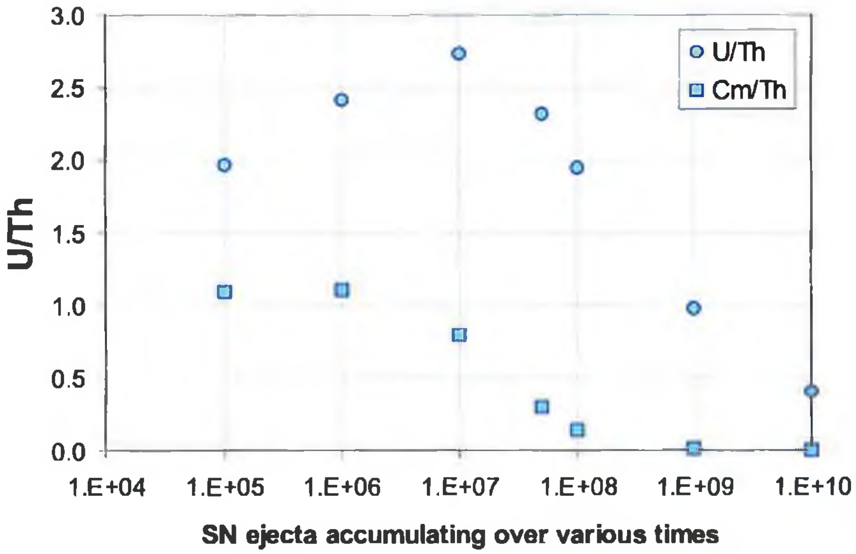

FIGURE 1.14 Calculated Evolution of U/Th Abundnace from r-process yields in accumulating core-collapse SNe ejecta (Lingenfelter *et al.*, 2003).

---

[*] Such as the (n, γ) and (γ, n) probabilities, α- and β-decay half-lives and fission probabilities.

[†] Developed by Kratz *et al.* (1993) and Pfeiffer *et al.* (1997).

2. Experimental Configuration

2.1 LDEF Mission and Configuration

The Long Duration Exposure Facility (LDEF) was designed and built by the NASA Langley Research Centre to accommodate experiments for long-term exposure to the space environment. It was a low-cost, reusable, unmanned and free-flying spacecraft designed to transport experiments into space via the Space Shuttle, free fly in Earth orbit for an extended period and be retrieved on a later flight for analysis. The 57 experiments aboard the LDEF addressed the fields of basic science, technology and applications problems. They measured specific space environments (meteoroids, man-made debris and radiation levels) and the effects of the space environment on both typical spacecraft hardware and on simple forms of life.

The LDEF was launched on 6th April 1984 on the STS-41C *Challenger* mission and deployed in Earth orbit on the following day (fig. 2.1). The *Challenger* accident and consequent scheduling problems meant that the LDEF was not retrieved on 19th March, 1985 as planned. Instead, it was retrieved on 9th January 1990 by STS-32 (shuttle *Columbia)* after spending 69 months in space – 58 more than planned.

LDEF deployment and retrieval occurred close to solar-minimum and solar-maximum respectively. The orbit was almost circular (perigee 473.9 km, apogee 480.0 km) and at an inclination of 28.5°. The geomagnetic cutoff for ultra-heavy GCRs in this orbit was ~1.5 GeV nucleon^{-1} or $\beta \approx 0.92$ (Thompson *et al.*, 1993).

The facility was in a gravity-gradient stabilised orbit: gravity gradient torques maintained the LDEF in a position in which the axis of minimum moment of inertia was aligned with the local vertical – one end of the LDEF always pointed towards the centre of the Earth and the other out to deep space. Coupling torques stabilised the facility about the longitudinal axis and resulted in one of the sides always pointing forward in the direction of travel.

FIGURE 2.1 LDEF deployment in orbit.

The LDEF was configured as a 12 sided, 4.3 m diameter, 9.1 m long aluminium open grid frame [fig. 2.2(a); Levine, 1991]. The structure had 72 equal-sized rectangular openings on the sides and 14 openings on the ends which were designed to mount experiment trays. The total mass of the spacecraft was approximately 9,700 kg (4,000 kg of which were structure and systems and the remaining 5,700 kg trays and experiments). At 1,250 kg (over 20% by mass of the entire payload), the largest LDEF experiment was the Ultra-Heavy Cosmic-Ray Experiment (UHCRE).

The LDEF thermal control was completely passive, relying on surface coatings and internal heat paths. The stable attitude of the spacecraft (one end Earth-pointing and a leading and trailing side) resulted in one side facing the Sun or space for extended periods of time. All interior experiment and structure surfaces were painted with an emissivity black paint, Chemglaze Z306 ($\varepsilon = 0.90$), to allow maximum radiation coupling across the facility and to minimise the thermal gradients around it. The intention was to maintain an average interior temperature of between 10°F (-12 °C) and 120°F (49 °C).

2.2 The Ultra-Heavy Cosmic-Ray Experiment (UHCRE)

The UHCRE was housed in experimental trays, 1.2 m^2 in area, which were distributed around the surface of the LDEF. There were 16 UHCRE-designated trays and each contained three aluminium cylinders, each cylinder in turn containing four SSNTD stacks [fig. 2.2(b)]. Thus the experiment totalled 192 detector stacks which yielded a total surface area of ~10.2 m^2. Allowing for Earth shadowing, the total UHCRE exposure factor for high-energy ultra-heavy GCRs was 170 m^2 sr yr.

To provide both mechanical stability and thermal insulation, the detector stacks were embedded in sets of four inside cylindrical rigid polyurethane foam resin (Eccofoam) mouldings. These were then placed inside the experiment's 48 cylindrical aluminium pressure vessels (diameter 25.4 cm, length 117 cm and wall thickness 0.24 cm) (Thompson *et al.*, 1979). 47 of these vessels contained a dry oxygen-nitrogen-helium mixture (20:70:10) at 1.0 bar, while one was vented to space. Examination of the vented detector stacks revealed poor signal strength, probably due to a lack of oxygen, which rendered them unusable. Post-flight analysis revealed that no gas leakage had occurred in the sealed cylinders after 5.8 years in space. The UHCRE spent 69 months in orbit at a mean temperature of –20 °C After disassembly, the UHCRE detectors spent approximately eight months at NASA and ESTEC facilities at room temperature before entering long-term storage at the Dublin Institute for Advanced Studies (DIAS) at a temperature of –31 °C.

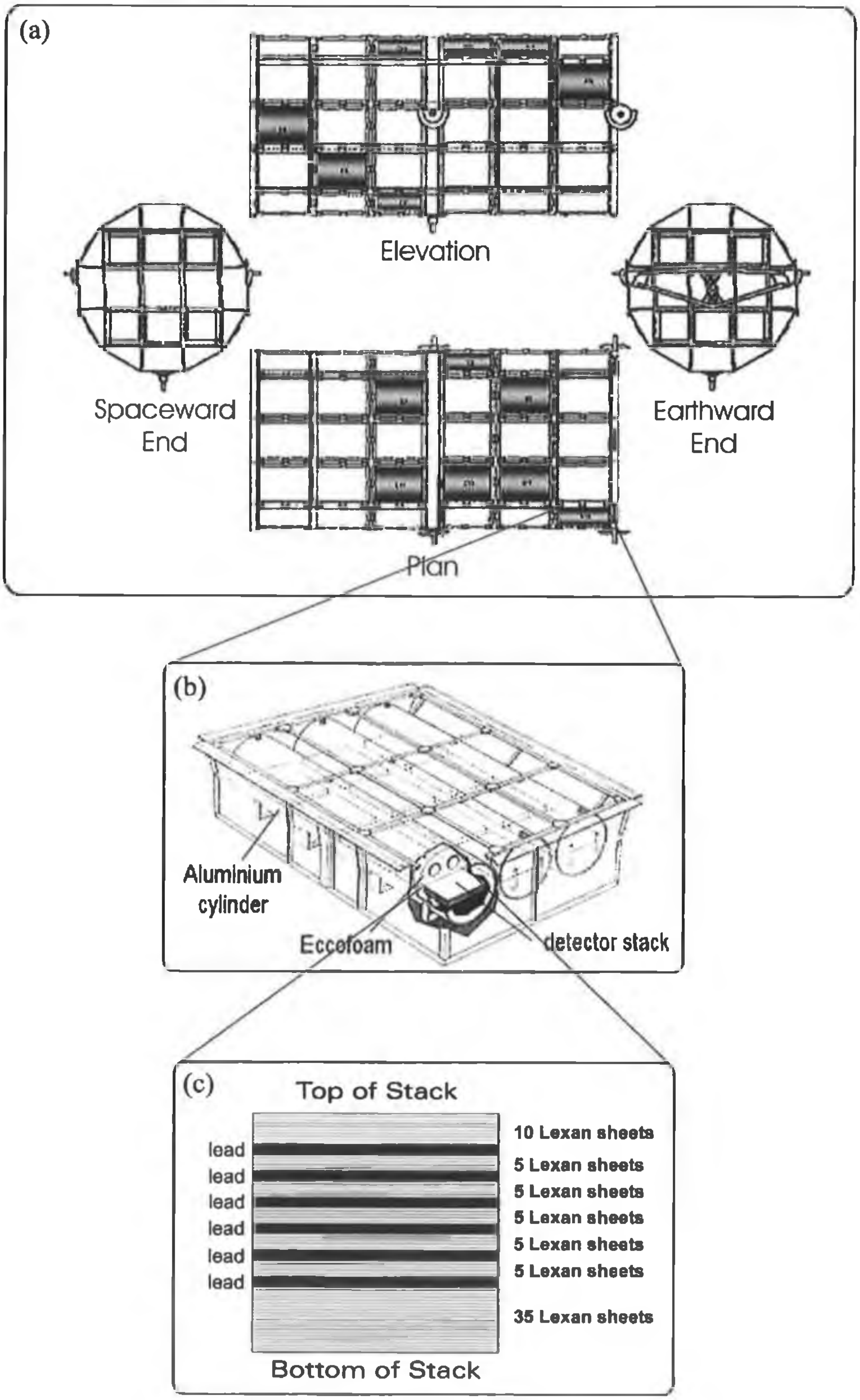

FIGURE 2.2 (a) The LDEF spacecraft with the locations (shaded boxes) of UHCRE experiment trays. (b) A typical UHCRE-designated experiment tray. (c) A typical UHCRE stack configuration, in this case, type *A*.

De-integration of the detector in a clean room was carried out at the Kennedy Space Centre in early 1990. The UHCRE experimental trays were shipped to the European Space

Research & Technology Centre (ESTEC) in Noordwijk, Holland, except for six which were sent to be calibrated at the Berkeley Bevelac particle accelerator in California. At ESTEC, the aluminium cylinders were opened and examined and in August 1990, the detector stacks were sent to the DIAS for analysis.

The UHCRE's cylindrical pressure vessels were secured to the supporting tray frame by insulating washers, and the detectors radiatively decoupled from the support tray by low-emissivity bare aluminium on the bottom half of the detector cylinders. Black paint (Primer Pyrolac 123, Chemglaze Z306) on the top halves of the cylinders thermally coupled them to the underside of a thermal control blanket which covered each tray (Levine 1991). Further discussion of the UHCRE's temperature monitoring can be found in Section 3.2.1. See also Appendices *C* and *D*.

2.3 Solid-state Nuclear Track Detectors

Solid-state nuclear track detectors (SSNTDs) were developed on the principle that the passage of a heavily ionising particle through matter creates a narrow damaged region along its path. This damage trail (or *track*) possesses a higher chemical reactivity than the undamaged parts of the detector and when chemically etched becomes visible in an optical microscope. Fleisher, Price and Walker (1975) have written a thorough description of the technique.

A particular detector plate will yield a signal which depends on the incident particle's Z/β. Note that particles of different Z and β may cause an identical response in the same plate. To separate these parameters (i.e. determine the particle's Z), measurements must be made of the same particle in a number of juxtaposed plates (a detector 'stack'). The resultant series of measurements will yield a response curve which is a unique shape for each value of Z.

In the UHCRE, both Lexan and Tuffak polycarbonates were used to record incident cosmic rays of $Z/\beta > 65$. Lexan (stoichiometric formula $C_{16}H_{14}O_3$, density 1.2 g cm^{-3}) has a high registration threshold ($Z/\beta \cong 60$) making it ideal for studying ultra-heavy cosmic rays while filtering out the more abundant lower-charge nuclei. Particles in the $Z/\beta < 70$ charge region were also recorded using ADC polymers such as CR-39 (plain), CR-39 (DNP), CR-39 (DOP) and CR-39 (DIOP).

Each UHCRE SSNTD stack had a surface area of 26.5 × 20.0 cm and they consisted of combinations of plates of Lexan polycarbonate (each of thickness ~250 μm), lead (~500 μm), CR-39 (~500 μm) and Tuffak polycarbonate (~250 μm).

The stacks were of three main types: *A*, *B* and *C*. *A* stacks consisted of 70 plates of Lexan polycarbonate interleaved periodically with 6 lead plates, which served as velocity degraders and electron strippers [fig. 2.2 (c)]. Since the nuclear interaction length (for a given absorber mass) of fast ultra-heavy nuclei is ten times greater in lead than in polycarbonate, the lead plates increased the probability that cosmic rays would penetrate the entire stack without interaction. *B* stacks contained 60 plates of Lexan and 4 of lead. Some *A* and *B* stacks also contained CR-39 plates in various combinations. *C* stacks, however, had no lead plates and consisted of 24 different combinations of Lexan, CR-39 and Tuffak polycarbonate.

In all, an average stack had a thickness of approximately 5.6 g cm^{-2} (2.0 g cm^{-2} of which was polycarbonate, 0.3 g cm^{-2} ADC and 3.3 g cm^{-2} lead), the Lexan equivalent thickness for a 1.0 GeV $nucleon^{-1}$ particle being 4.1 g cm^{-2} (Thompson *et al.*, 1979).

2.4 Detector Processing

When immersed in a suitable etchant, the plastic of a SSNTD undergoes two simultaneous processes: chemical dissolution along the particle track at a linear rate (V_T, the track etch rate) and general attack on the etched surface at a lesser rate (V_G, the bulk etch rate). It is this preferential etching along the particle track (due to its higher chemical reactivity) that forms characteristic cone-shaped pits at an ion's entry and exit points in a detector plate. Optical measurements of these 'cone pairs' allows geometrical calculation of the cosmic ray's V_T, and inference of its ionisation at that point. Both etch rates are directly involved in the determination of a cosmic ray's charge and were carefully monitored. Etching conditions can be influenced by the normality and temperature of the etchant and the concentration of etch products.

2.4.1 *Etching*

Etching of the UHCRE stack detectors was performed in three etch tanks, each with a capacity of 150 litres. The etchant was an aqueous sodium hydroxide (NaOH) solution of normality 6.25 ± 0.01 N. The solution also consisted of 5.0 ± 0.2% Dowfax 2A1 surfactant which provided superior surface quality to the etched Lexan plates. The solution was maintained at 40.00 ± 0.01 °C by a negative feedback temperature transducer and kept circulating by a stirring propeller connected to an uninterruptable power supply.

The solution was saturated with Lexan polycarbonate etch products by immersing several unused plates into the etch tanks for a suitable time (typically several days). Earlier work (e.g. Peterson, 1970) has demonstrated a relationship between V_G and the concentration of etch products. Though the bulk etch rate initially rises with the concentration, there follows a plateau in V_G beyond the solubility saturation value (at a concentration of ~2.2 g/l). All actinide etches for this work lay on this plateau (where concentration of etch products > ~3 g/l and $V_G \approx 0.15$ microns hour^{-1}). The concentration (and so V_G) was kept stable by regularly replacing a fraction of the solution with fresh (i.e. unsaturated) NaOH.

V_G values were obtained from three sample pieces of Lexan detector placed in every etch. The thickness change in each of these was measured under an optical microscope by three technical assistants.

The effects of random etch-tank variations on V_T values were monitored with track etch-rate monitors (TERMs). TERMs were plates from SSNTDs which had been exposed to particle accelerator beams (both 10.5 GeV nucleon^{-1} $_{79}$Au and 158 GeV nucleon^{-1} $_{82}$Pb beams were used). These plates were etched along with all actinide etches and served as a standard reference. The resulting TERM cone-pairs were measured after each etch to obtain a measure of the tank's etching strength. Sections 3.2.3 and 4.3.2 detail the methods by which these results were used to normalize the events. No statistically significant variation of V_T with etch-product concentration, etching time or dip angle (the angle of the cosmic ray's trajectory relative to the surface of the detector plate) was observed.

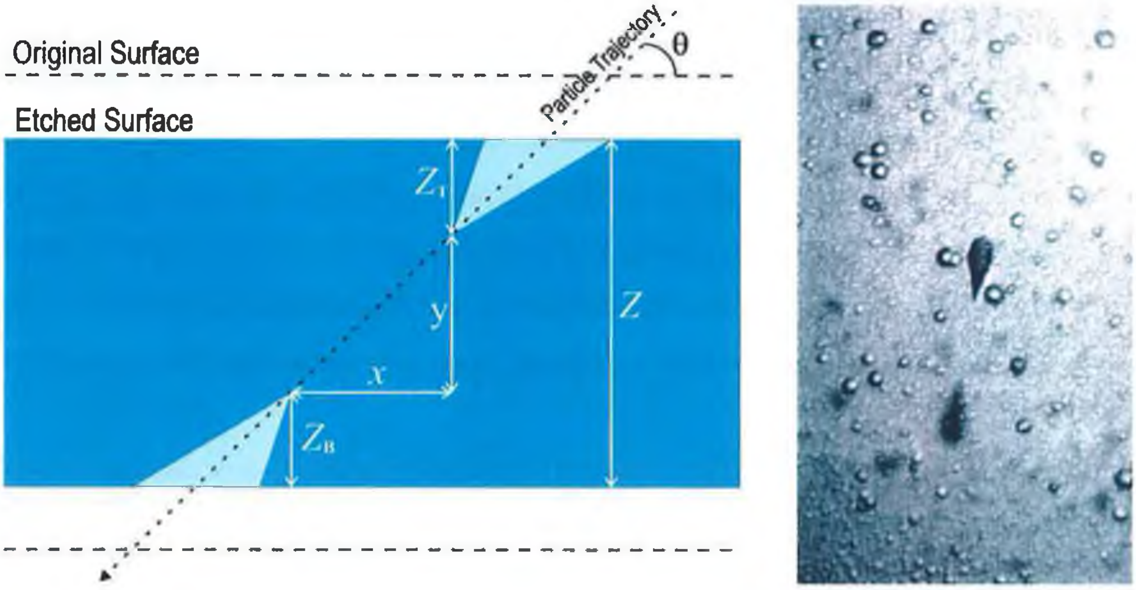

FIGURE 2.3 (a) The formation of etch cones in the surface of a solid-state nuclear track detector due to an incident nucleus of $\theta = 45°$ (where θ is the dip angle – the angle of the cosmic ray's trajectory relative to the surface of the detector plate). (b) A conical etched track as seen under an optical microscope.

Etch times varied with the function of the etch. Ammonia-scanning etches (see below) took many days. Etches to gather data on cosmic-ray events of Z similar to Pt and Pb typically took 120 hours and etches intended to reveal highly-ionising actinide events were much shorter (as low as 12 hours). A tank containing an aqueous HCl solution was used to terminate etching.

2.4.2 *Data Selection*

A semi-automatic ammonia gas-scanning technique was implemented to locate cosmic-ray events in each stack. During an etch, cone pairs with sufficiently high vertical V_T components (i.e. $V_T \sin\theta > \sim 1.6$) will co-join to form a 'tunnel' from one side of the detector plate to the other. After etching, the plates were bonded to ammonia-sensitive paper and exposed to an ammonia-gas environment. The ammonia gas reacted with the paper at points concurrent with etched 'tunnels', indicating the presence of a cosmic-ray event. This technique was applied to a sub-sample of plates from each stack. These plates were overlaid on measurement plates to provide location and direction information for every cosmic-ray event.

Of the UHCRE's 192 detector stacks, only 162 were directly accessible. The remainder, which were exposed to calibration beams from particle accelerators, proved to be saturated with events and were eliminated from the sample. 58 of these stacks were pseudo-randomly selected for full processing – providing an unbiased sample from all sides of the LDEF spacecraft. The ammonia-scanning technique was used to locate all ultra-heavy events in these stacks, which would provide a relative-abundance charge spectrum from $Z \geqslant 70$. Shortening the ammonia-etch time meant that only those events with very high V_T values formed tunnels. This technique was used to locate the complete sample of actinide ($Z \geqslant 88$) events collected during the experiment's exposure period in the remaining 104 unprocessed stacks.

The ammonia-scanning technique revealed ≈18 ultra-heavy (i.e., $Z > \approx 60$) nuclei per detector plate. The following selection criteria were applied to the sample:

- While ammonia scanning can detect high-Z events, the technique's efficiency drops at lower charges. In order for an event to be detected in a given detector plate, the vertical components of the track etch rates of the two cones must be great enough to meet and form a tunnel. In practical terms, this means that events with a low value of $V_T \sin\theta$ are less likely to be detected by ammonia scanning.

- Every event with dip angle less than 30° was eliminated from the sample because the charge-assignment error on such events is large.

- The etching technique applies a charge-dependent angular cut-off to the sample. For an incident particle causing a particular V_T in the detector, there is a limiting dip angle, θ_{max}, beyond which measurable etch-cones will not form. This occurs when the vertical component of the track etch rate (i.e., $V_T \sin\theta$) is less than or equal to the bulk etch rate, V_G. When this is so, the track is dissolved by the etchant before it can form an etch cone. For a given element there is a limiting dip angle, θ_{cutoff} below which an etch cone will not form.

Figure 2.4 shows the angular cutoffs imposed on various elements by the above criteria. GCRs above the 30° line and to the right of the Z-dependent cutoff will be accepted. Some events will have dip angles falling between 30° and the Z-dependent cutoff. The method of compensating for these events is outlined in Section 4.2.

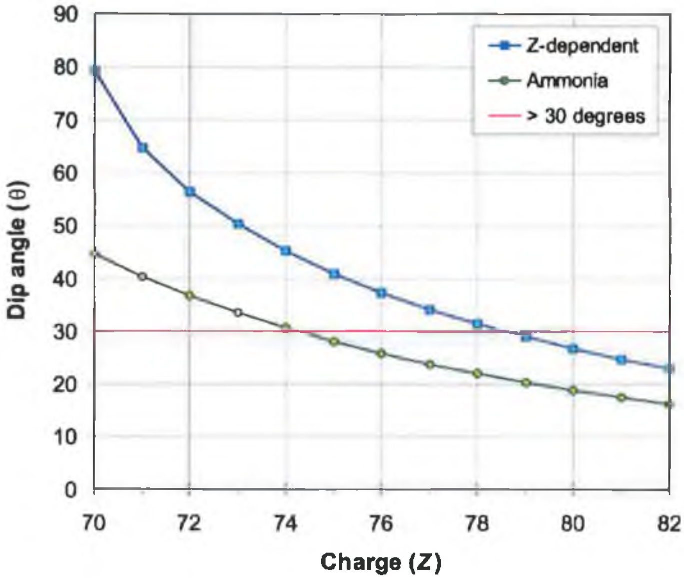

FIGURE 2.4 *Z*-dependent angular cutoffs for $Z > 70$ GCR events in the UHCRE (at -20°C and 5 GeV nucleon^{-1})

In addition, further quality control measures were implemented:

- Cosmic rays which fell below the registration threshold of, or demonstrated nuclear interaction in, the detector are eliminated. The latter usually manifested itself in the form of a rapid change in direction, dip angle (θ) or V_T between consecutive plates. The accuracy of the SSNTD technique depends on taking V_T measurements over as long a path length as possible through the stack. Using only those V_T measurements occurring before a nuclear interaction would thus result in a large charge-assignment error.

- Events failing to penetrate the stack were eliminated. Lexan polycarbonate has a registration threshold of $Z/\beta > 60$ and while this is sufficiently high that only ultra-heavy (i.e., $Z > \sim 70$) relativistic nuclei would leave a signal throughout the entire thickness of the stack, rapidly slowing Fe-group nuclei could register over some portion of the stack. Such events were detected by ammonia-scanning a selection of plates from throughout the stack. Events which fell below the detector's registration threshold at any point in the stack were assumed to be slowing Fe events and were eliminated.

- Events whose trajectory took them outside the 26.5 × 20.0 cm area of a stack were eliminated.

The remaining events, which constitute the UHCRE's ultra-heavy GCR sample, are further corrected for geometrical biases, earth-shadowing (Section 4.2) and fragmentation within the detector (Section 4.4).

2.4.3 *Data Measurement*

Etched cones were measured using Leitz-Ortholux optical microscopes with ×10 and ×25 eyepieces and a ×100 oil-immersion objective lens. Measurements in the plane horizontal to the microscope stage (and the detector plate) were conducted with a calibrated eyepiece graticule (of precision ± 0.05 μm). Measurements in the plane normal to the detector plate availed of a transducer connected to the microscope's movable eyepiece (which measured to a precision of ± 0.05 μm).

The measurements consisted of: Z_T (the vertical depth of the top etch cone), Z_B (the vertical depth of the bottom etch cone), Z (the plate thickness) and, x (the horizontal distance between the tips of the etch-cone pair). Z measurements were all relative to the *j*-point[*] of the top and bottom plate surfaces.

These measurements were performed for each cone pair, yielding two V_T measurements for each detector plate. Typically, twenty plates would be etched together to provide 40 measures of V_T through the stack[†] These data were entered into spreadsheets which flagged and eliminated Z_T, Z_B, θ or V_T measurements which deviated by more than 2σ from the mean. The results were then stored in text files and compared to calibration data to infer the charges of the original incident particles.

Summary

An important point to note here is that automatic scanning procedures were largely avoided in processing the UHCRE – every measurement used to identify the cosmic rays was obtained manually. These measurements were conducted under stringent quality-control procedures and the result is a huge dataset of carefully-gathered, unbiased measurements. Any remaining sources of error were closely monitored and are discussed in detail in Chapter 3.

---

[*] The *j*-point is the point at which the focal plane passes through the detector plate surface and is signaled by the apparent disappearance of etch-pit imperfections on the plate surface.

[†] An etch cone would commonly have Z_T and Z_B mmeasurements of a few tens of microns, while the typical plate thickness (Z) would be ~250 μm and the average dip angle (θ) was 54°. The mean difference in V_T between charge units is 0.050 microns hour^{-1} in the Pt-Pb region and 0.145 microns hour^{-1} for the actinides (see Section 3.2.1 for details).

3. Calibration and Sources of Error

In this chapter, the calibration of the UHCRE, using beams of relativistic nuclei and the restricted energy loss (REL) model, is discussed. Uncertainties due to variations in detector response, detector processing and registration temperature are examined. The total charge-assignment errors are derived and finally, a point-spread function for the detector response is obtained with a Monte-Carlo simulation. The results are all shown to concur with previous research carried out at the DIAS.

3.1 Calibration

Inferring the charge of a cosmic ray incident on a solid-state nuclear-track detector requires one to define a relationship between the particle's essentially immeasurable ionisation (J) and its readily measurable track etch rate (V_T). This relationship is assumed to be of the form $V_T = a\,J^n$, where a and n are determined by calibration. As shown in fig 3.1, three data sets are required: one relating ionisation to energy (cf. section 3.1.1), another range to energy (cf. section 3.1.2) and the last V_T to energy (cf. section 3.1.3). These data are used to generate theoretical V_{eff}-gradient curves (cf. section 3.1.4) for every possible charge of cosmic ray.

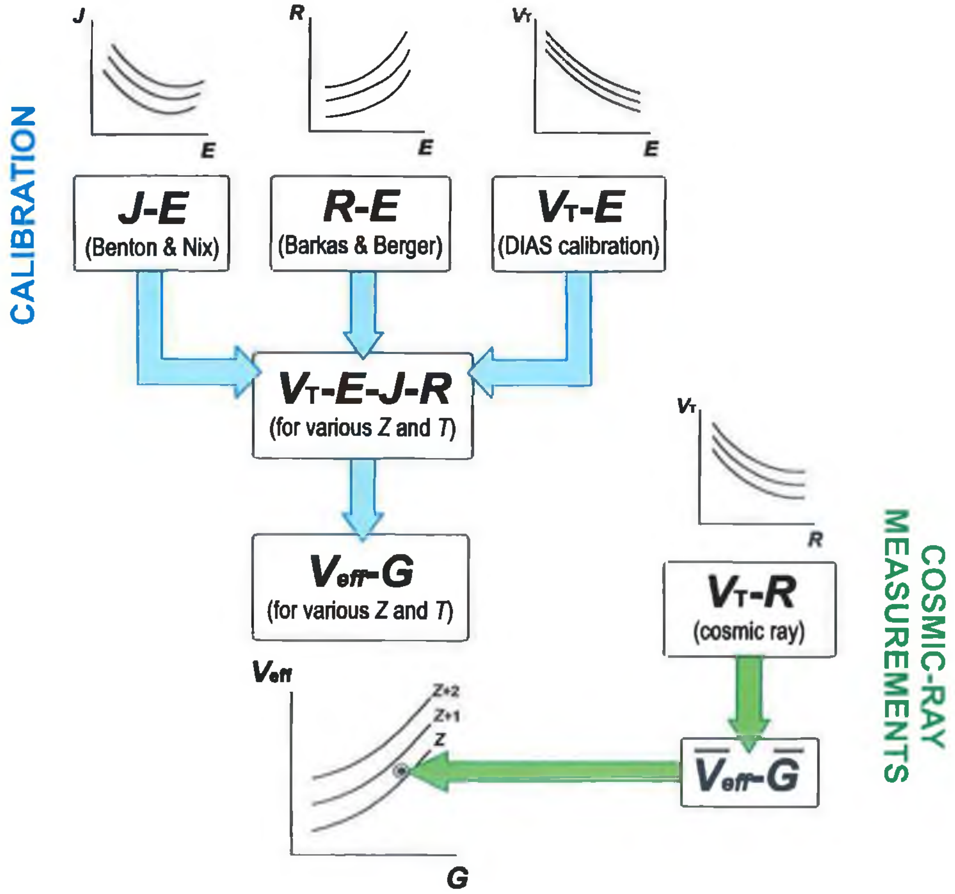

FIGURE 3.1 Overview of the cosmic-ray charge-assignment procedure for the UHCRE.

Measurements of actual events in the UHCRE's detectors are used to derive a single $\overline{V}_{eff}$ and $\overline{G}$ point for every cosmic ray. Interpolation between the theoretical calibration curves to this point provides an estimate of the cosmic-ray's charge.

3.1.1 *Energy-Ionisation*

We confine our discussion to very massive, heavily-ionising particles. For these, it is a very good approximation that the particles' trajectories are unaltered by multiple-Coulomb scattering. Because of the extremely small ($\sim 10^{-10}$) ratio of nuclear to atomic cross sections we can ignore the nuclear force. Inelastic nuclear collisions are also rare. We limit ourselves to velocities above those at which shell corrections become important for singly-charged particles ($\beta \sim 0.2$) and below those at which point radiative corrections become evident ($\gamma \sim 100$).

The scenario is that a particle (of mass M and electric charge Ze) penetrates a material composed of atoms (of atomic number Z_2 and mass M_2, where $M_2 = A_2$ amu). Using the elastic cross sections calculated by Bethe (1930) it can be shown that the ratio of energy lost in elastic collisions to that lost in inelastic collisions is, at most, of the order $m_e Z_2 / M_2$, where m_e is the mass of the electron. Hence, less than 0.1% of the projectile energy goes into atomic displacement. In calculating the stopping power we need merely sum over the various atomic excitation energies weighted by the cross section for such excitations.*

A cosmic ray's ionisation (i.e., its rate of loss of kinetic energy due to ionisation reactions in an absorber, dE/dx) may be related to its energy by a suitable energy-loss model. These models have traditionally been based on the Bethe-Bloch equation, a detailed derivation of which is provided by Longair (1992). The uncorrected Bethe-Bloch equation is:

$$-\frac{dE}{d\xi} = \frac{4\pi e^4 N_e}{m_e c^2} \frac{Z_2}{A_2} \frac{Z_{eff}^2}{\beta^2} \left[\ln\left(\frac{2m_e c^2 \beta^2 \gamma^2}{I_{adj}} \right) - \beta^2 - \psi(1) - \mathrm{Re}\,\psi(1+i\nu) \right]$$

where:

ξ is the distance traveled in g cm^{-2} ($\xi = \rho x$),
N_e is the electron density of the absorber,
Z_2 is the mean atomic number of the absorber,
A_2 is the mean atomic mass of the absorber,
$m_e c^2$ is the rest energy of the electron (0.511 MeV),

---

* These excitations are essentially ionisations of the stopping medium's atoms by the passing ion.

I_{adj} is the mean ionisation potential of the absorber (in eV). This value is semi-empirical and is determined by applying the Bragg rule of the additivity[*] to the stoichiometric components of the polycarbonate track detector,

Z_{eff} is the effective charge of the ionising particle, a semi-empirical value used by Pierce & Blann (1968): $Z_{\text{eff}} = Z\ \{1\text{-}\exp(-130\beta/Z^{2/3})\}$. Though strictly only valid for emulsions, this equation can be used for other solids, except for very heavy ions at low incident velocities (Benton & Nix, 1969; Pierce & Blann, 1968).

and $-\psi(1) - \mathrm{Re}\,\psi(1 + iv)$ is the Bloch correction for low-velocity particles.

This equation is valid only for massive ($m \gg m_e$) low-charge ($Z < 30$) ions traversing a gaseous absorber. Otherwise, integration of this equation allows us to determine the range of any particle in any stopping medium. Empirical measurements of such ranges in high-Z non-composite absorbers have differed greatly from calculated values. These discrepancies disappear if a corrected Bethe-Bloch formula, introduced by Ahlen (1982) and Waddington *et al.* (1986) is used (see below).

No full theory of latent track formation in a solid-state nuclear-track detector is available. Previously, two track registration models were used: the *primary ionisation (PI)* and *total energy loss (TEL)* models.

The TEL model (Fleishcher *et al.*, 1964) is based on the Bethe-Bloch equation and is known to differ from experimental data at high energies (Fleishcher *et al.*, 1967). The PI model assumes that the portion of ionisation damage that gives rise to a track is confined to a cylindrical region around the trajectory of the incident ion. This region has a net positive charge due to ionisation of the atoms of the stopping medium. The PI model neglects the secondary and higher-order ionisation produced by the electrons (i.e., δ-rays) ejected from the track-forming region.[†]

The opposite view is adopted by the restricted energy loss (REL) model. According to Benton & Nix (1969) the REL is the rate of energy loss of the bombarding particle due to the distant collisions with electrons of the stopping material. The emphasis here is not on the total energy lost by a fast-moving ion in an absorber, but rather only on those losses which

---

[*] National Academy of Sciences – National Research Council Publication – 1133 (1964).

[†] The PI model has the disadvantage that absolute values of the primary ionisation in plastics are not known – relative values must be used for calibration. Furthermore, experimental data on track registration in cellulose nitrate and Lexan requires that one of the model's parameters (I_0 – the ionisation potential of the outer shell electrons of the stopping atoms) to be set to 2 eV. This value appears to be much lower than the energy required to ionise an atom in practice.

contribute to the track formation process. Such losses are due to collisions with large impact parameters (i.e., involving distant electrons). These collisions impart energy lower than some threshold value (ω_0) to the absorber's electrons, which in turn deposit their energy around the incident particle's path – thus forming a track. Therefore ω_0 represents a boundary in energy between those electrons which contribute to track formation and those which do not. Note that ω_0 must fall in the range such that, for close collisions, the atomic electrons can be treated as free particles, while for distant collisions, the incident heavy particle is treated as a point charge.

The UHCRE has been calibrated using the REL model. Benton & Nix find that a value of $\omega_0 = (1.0 \pm 0.2) \times 10^3$ eV gave the best agreement with experimental data and this value has been adopted for the UHCRE analysis. The REL for fast, heavy ions in dense absorbers is a corrected Bethe-Bloch equation (Waddington *et al.*, 1986):

$$\left(-\frac{dE}{d\xi}\right)_{\omega < \omega_0} = \frac{4\pi e^4 N_e}{m_e c^2}\frac{Z_2}{A_2}\frac{Z_{eff}^2}{\beta^2}\left[\ln\left(\frac{2m_e c^2\beta^2\gamma^2}{I_{adj}}\right) - \beta^2 - S - \delta + M - B + R_B - \Delta_R\right]F$$

Note that the complete quantic Bloch term, $-\psi(1) - \mathrm{Re}\,\psi(1+i\nu)$, is due to close collisions and therefore should not appear in the REL equation. The new terms are correction factors: the inner-shell correction (S; Barkas & Berger, 1967), the density effect (δ; Sternheimer & Peierls, 1971), the Mott scattering correction (M; approximated by Ahlen, 1982), the Bloch and the relativistic Bloch corrections (B and R_B), the Leung correction (Δ_R) and the low-velocity correction (F). Of these, the Bloch, relativistic Bloch, Mott and Leung corrections are due to collisions close to the incident particle and are irrelevant to track formation under the REL model. The inner-shell and low-velocity corrections are due to both close and distant collisions. The former may be ignored since its effects are negligible for swift, heavy ions in a low-Z absorber such as a polycarbonate SSNTD. The latter is excluded since the use of the effective charge, Z_{eff}, accounts for the same physical process (charge pickup of the ionising particle).

However, the density effect *is* relevant to the UHCRE. An implicit assumption of the Bethe-Bloch result is that the absorber is a very dilute gas. However, in a solid-state track detector, the interatomic spacing is reduced by a factor of ~10 and the incident ion cannot be considered to act on one atom at a time (Ahlen, 1980), so the medium can be polarised. At low energies the distant-collision contribution increases as $\ln(\beta^2\gamma^2)$. However, as the particle's energy increases, its electric field flattens and extends, so that (dE/dx) then grows only as $\ln(\beta\gamma)$. The density correction therefore removes the assumption that the energy transfer to the electrons is incoherent and accounting for such absorber polarisation lessens the energy loss at high velocities (typically by ~10% for the cosmic rays encountered by UHCRE). The value of δ is computed from a parameterisation:[*]

Table 3.1 Density Effect Correction (δ)

$X_0 < X$	0
$X_0 < X < X_1$	$\log(gmm) + C + a(X_1 - X)^m$
$X > X_1$	$\log(gmm) + C$

Here, $X = 0.21715\ \log_{10}(gmm)$ and X_0 and X_1 are particular values of X, such that when $X < X_0$, $\delta = 0$ and when $X > X_1$, δ has reached its asymptotic form. For the UHCRE, $X_0 = 0.14$ and $X_1 = 2.0$.[†] $C = -3.21$, $a = 0.456$, $m = 2.78$ and $gmm = \{(E + m_0c^2)/m_0c^2\}^2 - 1$.

The $dE/d\xi$ of cosmic-ray ions in an UHCRE detector is calculated in arbitrary units using the following expression:

$$\left(-\frac{dE}{d\xi}\right)_{\omega < \omega_0} = \frac{Z_{eff}^2}{10{,}000\beta^2}\left[\ln\left(\frac{2m_ec^2\beta^2\gamma^2}{I_{adj}^2}\right) - \beta^2 - \delta\right]$$

Note that for the reasons outlined above only the density correction is included. Fig 3.2 demonstrates the influence of this density effect as projectile energy increases.

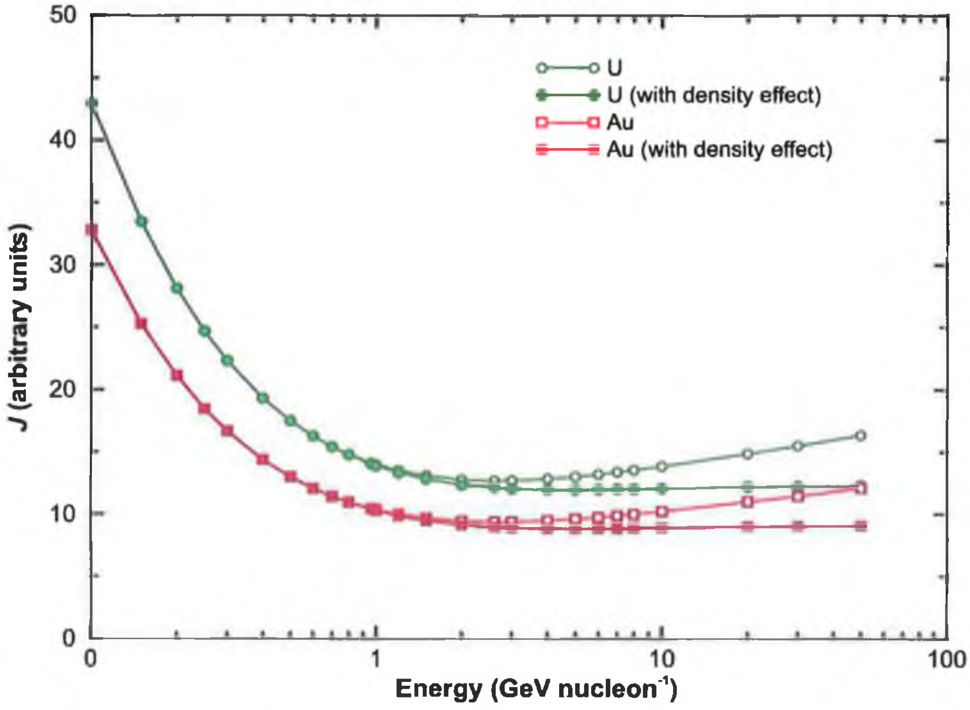

FIGURE 3.2 Ionisation losses for $_{92}$U and $_{79}$Au projectile ions in a Lexan polycarbonate detector, both with and without the density effect.

---

[*] e.g., Sternheimer & Peierls, 1971.

[†] Ahlen (1980) uses the following values for solids and liquids: $X = \log_{10}(\beta\gamma)$, $X_0 = 0.14$ and $X_1 = 2.0$ (for $I < 100$ eV) or 3.0 (for $I \geqslant 100$ eV), $C = -\{2\ln(I/\hbar\omega_p)\}-1$, $a = \{-(C + 4.606X_0)\ /\ (X_1 - X_0)^m\}$ and $m = 3.0$, where I is the mean excitation potential for the electrons of the medium and $\hbar\omega_p$ is the corresponding plasma energy ($\hbar\omega_p = 28.8(\rho_0 Z/A_0)^{1/2}$ eV, where ρ_0 is the density of the material and Z and A_0 are its atomic number and atomic weight respectively).

Projectiles in other media generate qualitatively similar curves. Note that the ionisation rate is a very sensitive function of particle energy ($\propto$-β^2). At low energies (γ~1) particles of different rest mass but of equal momentum can be distinguished by their different rates of energy loss.* At intermediate energies (> ~1 GeV nucleon^{-1}) the stopping power decreases to a minimum. This is due to the combined effects of: a) a decrease in energy loss caused by the -β^2 term (since at high energies, β saturates at unity) and b) a relativistic rise caused by the $\ln(\gamma^2)$ term. At high energies (> ~10 GeV nucleon^{-1}) there is a relativistic rise in ionisation that segues into an energy-independent region. At still higher energies (> ~1 TeV nucleon^{-1}) radiative effects become important and particles cannot be differentiated purely on the basis of ionisation losses.

3.1.2 *Range-Energy*

Barkas & Berger (1964) provide empirically derived range-energy tables for the ideal proton – a particle of protonic mass and charge that does not capture electrons or suffer close collisions with nuclei. When these are combined with a heavy ion extension (cf. Benton & Henke, 1969) a relationship between range and energy can be inferred for particles of various Z:

$$R(\beta) = M/Z^2\ [\lambda(\beta) + B_Z(\beta)],$$

where M and Z are the mass and charge of the incoming particle. λ is the ideal proton range, values of which have been published (Barkas & Berger, 1967) for various energies and stopping materials. Barkas & Berger expressed electronic stopping power as a universal function of two variables (the kinetic energy of the incident particle and the mean excitation energy of the stopping medium) using empirical data. They then systematised the calculation of proton ranges in all materials as follows:

$$\lambda \approx \left(11.1 + 1.34 I_{adj}^{5/8}\right)\frac{A}{Z}\beta^{10/3} \quad g\,cm^{-2}$$

I is the mean excitation potential for the electrons of the medium (≈ 69.5 eV for Lexan polycarbonate – calculations for which are provided in Appendix *A*).

B_Z is the heavy-ion range extension. This range extension is caused by charge pickup near the stopping end of the track and is dependent on the Z and β of the incoming ion and the A, Z and I_{adj} of the absorbing medium: $B_Z\left(I_{adj}, \beta\right) \approx \left(48.0 + 5.8 I_{adj}^{5/8}\right)\frac{A}{Z} \times 10^{-5} z^{5/3} \beta \quad g\,cm^{-2}$

---

[*] Also, at energies < 1 GeV nucleon^{-1} the details of the stopping medium are important as electron capture can alter the Z_{eff} of the incident ion.

The calculated values of range as a function of energy for $_{79}$Au and $_{92}$U projectiles in the UHCRE detectors is shown in fig 3.3.

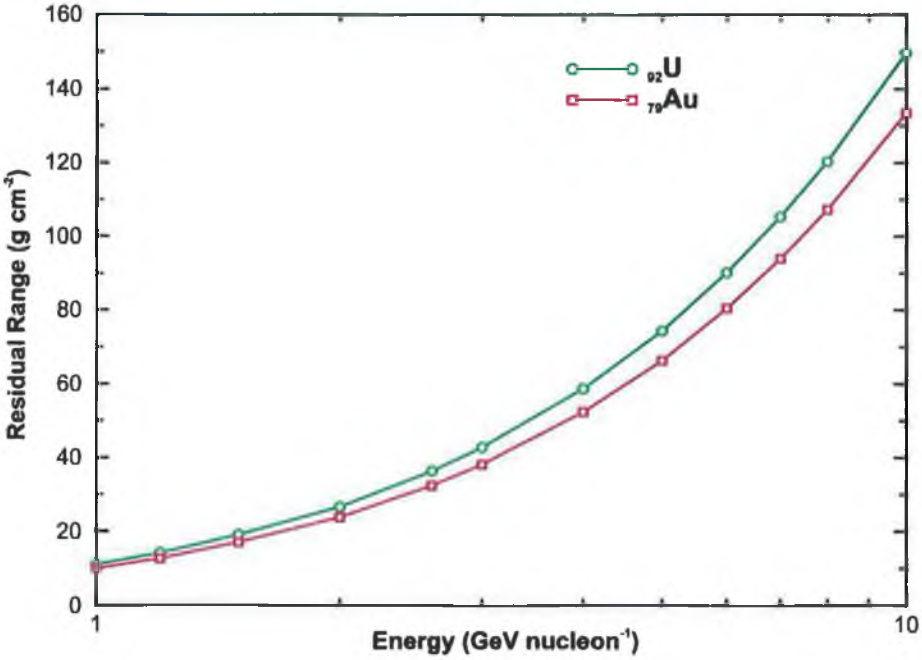

FIGURE 3.3 Calculated residual ranges for $_{92}$U and $_{79}$Au ions in Lexan polycarbonate at various energies.

3.1.3 *V_T-Energy*

The track-etch rate, V_T, is a measure of the bombarding cosmic ray's ionising power. To calibrate a detector stack, V_T measurements in the stack must be made at different energies and exposure temperatures (to allow adjustment for the registration temperature effect, cf. Section 3.2.2). Such measurements were completed for both the actinide and Pt-Pb charge regions.

For actinide calibration, a 0.96 GeV nucleon^{-1} $_{92}$U beam from the heavy-ion accelerator at the Gesellschaft für Schwerionenforschung mbH (GSI), Darmstadt, Germany was used. In November 1996, UHCRE detector stacks were exposed to this beam, yielding a V_T-energy relationship at various points through the detector. The beams were exposed at two registration temperatures (18 °C and –78 °C). The results from these exposures are summarised in Table 3.2.

Table 3.2 $_{92}$U calibration beam response

Energy (MeV nucleon^{-1})	Temperature (°C)	V_T (microns hour^{-1})
500	-78	6.67
	+18	3.78
800	-78	3.78
	+18	2.11

To enable calibration of the Pt-Pb region, DIAS Lexan polycarbonate SSNTDs were previously exposed to $_{79}$Au calibration beams at the Brookhaven National Laboratory (BNL) in January 1996. The beams were of various energies (2.0, 4.0 and 10.5 GeV nucleon^{-1}) and were exposed at several different temperatures. The results are summarised in Table 3.3.

Table 3.3 $_{79}$Au calibration beam response

Energy (GeV nucleon^{-1})	Temperature (°C)	V_T (microns hour^{-1})
2.0	-70	1.04
	-20	0.92
4.0	-70	0.92
	-20	0.84

Range-energy (*R-E*) and energy-ionisation (*E-J*) values were calculated for all $70 \leqslant Z \leqslant 100$ elements, providing a table of *R-J-E* relationships across a wide energy spectrum. These tables were combined with the calibration V_T-*E* measurements. In this way, *R-J-E*-V_T tables were compiled for all ultra-heavy elements at all relevant temperatures.*

3.1.4 *Particle Identification*

A cosmic ray's V_T can be measured at various points along its trajectory through the detector (i.e., at various residual ranges, *R*). In theory, a comparison between the V_T-*R* curve of the ion and those of the calibration particles should allow charge identification. However, if the cosmic ray penetrates the entire detector without coming to a halt, its residual range (i.e., the distance from its stopping point) cannot be determined. In this case, the *gradient* method is employed.

Two different datasets are required: *R-J-E*-V_T calibration tables for every *Z* and measured values of the cosmic ray's V_T and *R*. These are used to generate theoretical V_{eff}-gradient curves for every *Z* (fig 3.4) and a $\overline{V}_{eff}$ and $\overline{G}$ point for every cosmic ray. The curve closest to the point is the inferred charge of the incident ion.

---

* Calibration values were obtained at two different temperatures and linear interpolation was used to compensate for the registration temperature effect (see Section 3.2.2) in which V_T varies with the temperature of the SSNTD at the time of track registration.

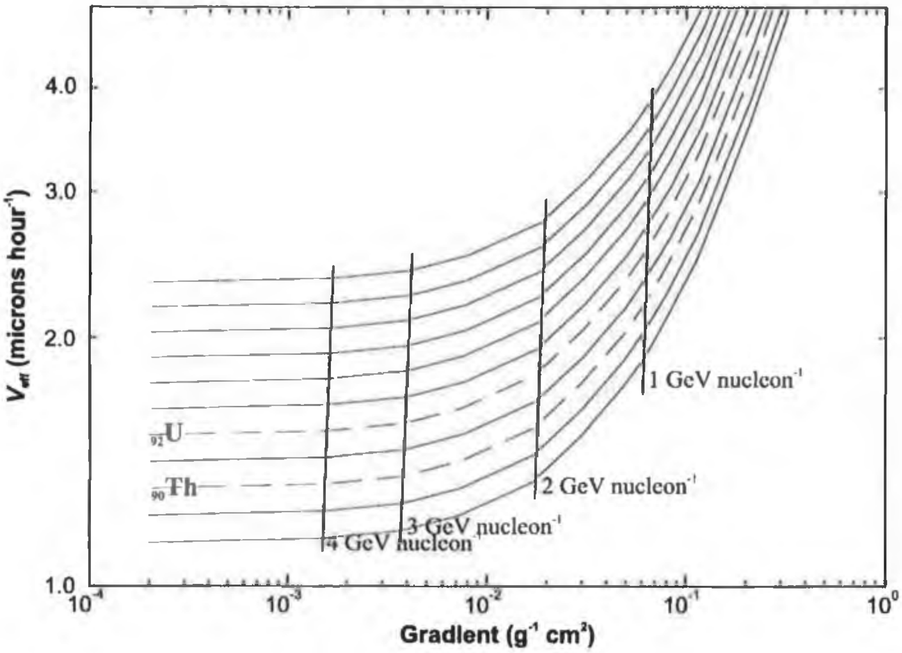

FIGURE 3.4 Actinide calibration curves for $88 \leqslant Z \leqslant 98$ ions in Lexan polycarbonate at a registration temperature of –20 °C. A cosmic ray can be plotted as a single point ($\overline{V}_{eff}$ and $\overline{G}$) on this graph.

The fractional etch-rate gradient, G, is defined as (Fowler *et al.*, 1977):

$$G = \left(\frac{1}{V_T}\right)\left(\frac{dV_T}{dx}\right)$$

It is thus a measure of the rate of change of V_T with respect to distance travelled by the ion. If two etch rates, V_{T1} and V_{T2}, are measured at two points separated by a distance Δx, then G is given by:

$$G = \left\{\frac{2(V_{T2} - V_{T1})}{(V_{T2} + V_{T1})\Delta x}\right\}$$

The second quantity to be defined is the effective track-etch rate, V_{eff}, given by:

$$V_{eff} = \frac{(2V_{T1}V_{T2})}{(V_{T1} + V_{T2})}$$

In a SSNTD stack of n plates, a cosmic-ray track will leave $2n$ etch cones and the overall mean value of G is given by:

$$\overline{G} = \frac{\sum_{i=1}^{n}\left[\left(2(V_{2n+1-i} - V_i)W_i\right)/\left((V_{2n+1-i} + V_i)\Delta x_i\right)\right]}{\sum_{i=1}^{n} W_i}$$

where $W_i \propto (\Delta x_i)^2$ and is a weighting factor and V_i is the track-etch rate of the i^{th} cone.[*] The overall value of V_{eff} in such a stack of detector plates is:

$$\overline{V}_{eff} = \frac{n}{\sum_{i=1}^{n}\left[(V_i + V_{2n+1-i})/(2V_iV_{2n+1-i})\right]}$$

---

[*] The error associated with this etch-rate gradient is: $\Delta G = (6/n)^{1/2}\,(\sigma/\Delta x_{max})$, where n is the number of cone pairs measured, σ is the fractional standard deviation in the measured etch rate of a cone and Δx_{max} is the maximum path length (Fowler *et al.*, 1977).

In practice, systematic errors in particle-accelerator beam measurements required the use of internal calibration. In the actinide region, a 12% increase in calibration V_T values provided optimum resolution of the $_{90}$Th and $_{92}$U peaks (as well as ensuring that a very high-charge transuranic event was binned as $_{96}$Cm). In the Pt-Pb region, a 20% decrease in calibration V_T values yielded the optimum $_{79}$Pt and $_{82}$Pb peaks. The causes of these systematic errors in the calibration are most likely due to inaccuracies in the calibration beam energy, errors in the recorded registration temperatures (cf. section 3.2.2), differing etching conditions between the calibration stacks and the UHCRE detector stacks (cf. section 3.2.3) and the difference in energy between the particle accelerator beams and those of the cosmic rays detected.

3.1.5 *Calibration Tests*

Previous work at DIAS has tested the calibration model* by using a beam of 1.125 GeV nucleon^{-1} $_{79}$Au ions exposed to a typical UHCRE stack. The inferred charge of these test events was $Z = 79.1 \pm 1.1$, demonstrating that the model could successfully extrapolate from $_{92}$U to $_{79}$Au.

To test energy extrapolation, UHCRE stacks were exposed to ions from a $_{79}$Au beam for analysis. These ions were of low ($100 \leqslant E \leqslant 400$ MeV nucleon^{-1}) and high ($10.3 \leqslant E \leqslant 10.6$ GeV nucleon^{-1}) energies and were identified as being $Z = 78.3 \pm 1.0$ and 78.9 ± 1.0 respectively (Bosch, 1994). This successful identification implies that the values of a and n in the calibration are essentially energy-independent in the range of energies encountered by UHCRE (modal value $\approx$ 2-3 GeV nucleon^{-1}).

Note that these beam exposures were conducted with the detector stacks in their original experimental configurations (i.e., still sealed inside Eccofoam and their pressure vessels). These tests demonstrated the sturdy nature of the calibration model and its ability to extrapolate from the actinide region to the Pt-Pb region (across at least 13 e) and from energies as low as 100 MeV nucleon^{-1} to as high as 10.6 GeV nucleon^{-1}.

---

* The model is based on a $_{92}$U calibration. In May 1992, 12 UHCRE detector stacks were exposed to a 0.96 GeV nucleon^{-1} $_{92}$U beam at the Lawrence Berkeley Laboratory, California.

3.2 *Z*-Assignment Error Estimates

A number of separate errors contribute to the overall error in GCR charge identification (ΔZ). These errors are due to: intrinsic detector imperfections (cf., Section 3.2.1), changing temperature at the time of track registration (cf., Section 3.2.2), varying etching conditions (cf., Section 3.2.3) and latent track effects (cf., Section 3.2.4).

3.2.1 *Intrinsic Error*

The intrinsic error in a single cone pair measurement was determined empirically by exposing detector material to a beam of ≈ 10.5 GeV nucleon^{-1} $_{79}$Au ions. Lead degraders in the detector stack reduced the energy of the beam to 2 GeV nucleon^{-1}. Samples of this exposed polycarbonate were processed during a series of etches spanning over a year. As many as twenty cone pairs were measured in each, resulting in 442 individual cone-pair measurements of Z_T (the vertical depth of the top etch cone), Z_B (the vertical depth of the bottom etch cone), Z (the plate thickness) and, x (the horizontal distance between the tips of the etch-cone pair). These measurements yielded a value for the mean standard deviation in a single etch (Table 3.4). Here, "Filtered" refers to the sample after the same quality control imposed on the UHCRE's cosmic-ray events is applied (i.e., measurements deviating by more than 2σ from the mean were removed). Filtering reduced the sample size to 345 cone pairs.

Table 3.4 Mean standard errors (σ) on a single cone measurements of a $_{79}$Au ion[*]

$_{79}$Au beam	V_T (microns hour^{-1})	ΔV_T (microns hour^{-1})	%
Unfiltered	0.616	0.027	4.4
Filtered	0.618	0.016	2.5

Though there were insufficient measurements for a definitive point-spread function (PSF), the overall V_T distribution appears quasi-Gaussian (fig 3.5), possibly possessing a low-V_T tail. However, our charge identification model is based upon V_{eff}, which depends on the *mean* of a set of V_T values. Since the distribution of a sample of means is closer to Gaussian than that of the dataset itself, our empirically-derived PSF represents an *upper-limit* on the asymmetry of V_T distribution.

---

[*] Note that these errors are upper limits as higher-charge events (with larger cones) are more easily measured.

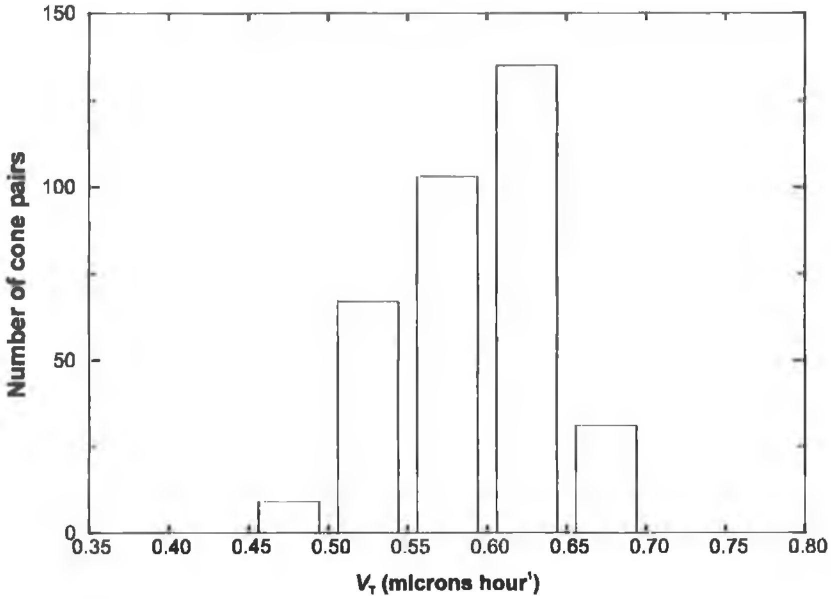

FIGURE 3.5 V_T distribution of 345 cone pairs from a $_{79}$Au ions in UHCRE detector material. The sample was filtered to remove measurements deviating by more than 2σ from the mean.

This spread of V_T values is due to imperfections intrinsic to the detector material and will in turn induce errors in measured values of both $\overline{V}_{eff}$ and $\overline{G}$, which are used for charge-identification of every cosmic ray detected by the UHCRE (fig 3.6). Note that the magnitude of these errors will depend on the energy of the cosmic ray – high-energy events (i.e., those with low gradients) will have relatively low errors. Thus, mean values for $\Delta\overline{V}_{eff}$ and $\Delta\overline{G}$ are used.

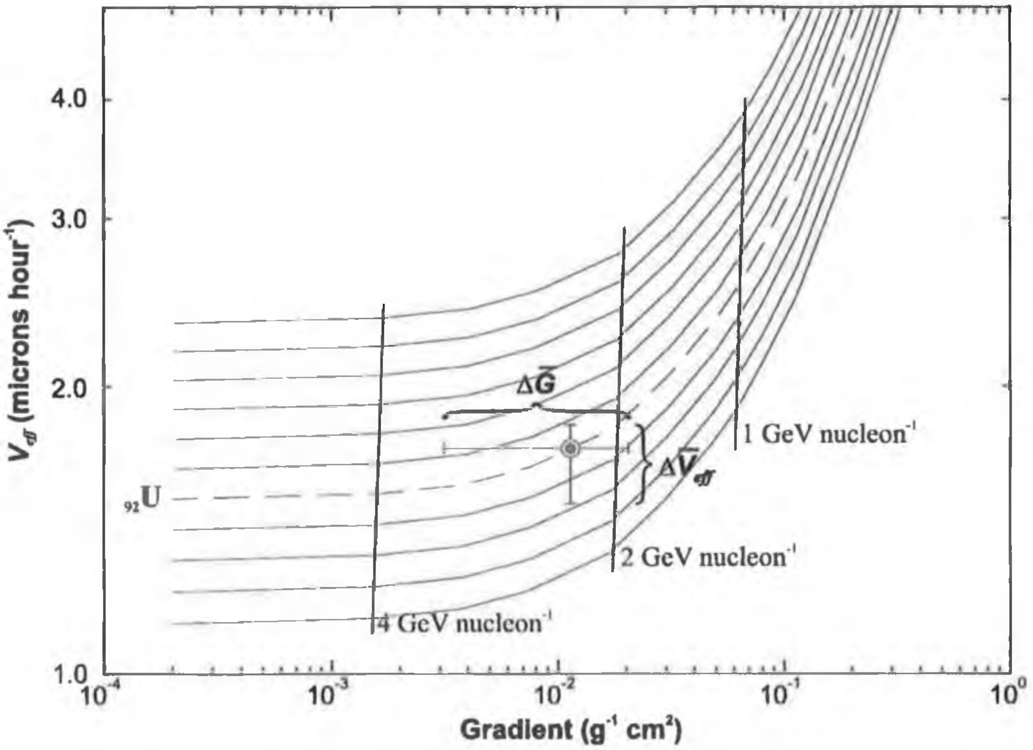

FIGURE 3.6 An intrinsic error in V_T measurements causing an error in charge assignment of a $_{92}$U ion.

$\overline{V}_{eff}$ is obtained from a number of individual V_T measurements and so $\Delta\overline{V}_{eff}$ is inversely proportional to $\sqrt{n}$, where n is the number of cone-pairs measured. Since n is typically between 10 and 20 (after filtering) the average error on $\overline{V}_{eff}$ is relatively small – typically ± 0.036 and ± 0.022 microns hour^{-1} in the Pt-Pb and actinide regions respectively. These uncertainties correspond to charge-assignment errors of ± 0.72 e (in the Pt-Pb region) and ± 0.15 e (in the actinide region).*

Errors were estimated by applying the mean intrinsic ΔV_T (± 4.4%) to each cone-pair measurement of every actinide event and every Pt-Pb event. These altered measurements were then propagated through the entire charge-identification procedure. The results provided an estimate of the upper and lower errors on charge assignment due to intrinsic detector error (table 3.5).

Table 3.5 Mean standard intrinsic detector errors (σ) for actinide and Pt-Pb ions (expressed in e)

Z region	Error Bar	mean ΔZ from $\Delta\overline{V}_{eff}$	mean ΔZ from $\Delta\overline{G}$	Total mean intrinsic ΔZ
Actinides† ($Z > 88$)	+	0.2	0.9	1.1
	-	0.2	1.1	1.2
Pt-Pb ($70 \leqslant Z \leqslant 88$)	+	0.4	0.5	0.6
	-	0.4	0.8	0.9

3.2.2 *The Registration Temperature Effect (RTE)*

The variation of signal strength with registration temperature in SSNTDs (the registration temperature effect or RTE) was first reported by DIAS (Thompson *et al.,* 1979 and O'Sullivan *et al.,* 1980). The strength of a latent ion-track in a SSNTD is a function of the temperature of the stack at the time of registration; higher registration temperatures reduce the latent track strength. Subsequently, Thompson and O'Sullivan (1984) discovered that the strength of the effect itself varies with ionisation and is more pronounced in incident ions of higher Z/β. Consequently, the UHCRE detectors were under careful temperature control and monitoring during the exposure period.

---

* Elements in the Pt-Pb region are separated by an etch rate difference of 0.050 microns hour^{-1} (at their mean gradient of 0.01 g^{-1} cm^{2}). For the actinide region, elements around $_{92}$U are separated by 0.145 microns hour^{-1} (at their mean gradient of 0.033 g^{-1} cm^{2}).

† Actinide errors are upper-limit estimates, since the fractional ΔV_T will be smaller for these events.

Thermal decoupling from the spacecraft frame biased the detector stack temperatures to over 20°C below that of the LDEF itself (Thompson, 1990). Tray temperature measurements were recorded at intervals of 112 minutes for the first 390 days of the LDEF's 2,105-day flight. NASA commissioned Lockheed to perform a thermal analysis of the spacecraft. The 16 individual detectors each had mean temperatures of between –15.5 °C and –23 °C, with an overall mean of –20 °C. Standard deviations in tray temperature varied from 2.2 °C to 6.8 °C, averaging at 4.3 °C (Sampair, 1991; Bosch, 1995).

Estimates of the RTE indicate a variation of ± 0.14e in Lexan for Uranium ions at 960 MeV nucleon^{-1} (Thompson and O'Sullivan, 1984). Since the average cosmic ray in the UHCRE sample is of both lower charge and higher energy, this figure safely over-estimates the magnitude of the RTE. Using this figure implies that temperature variations contribute a 1σ error on charge-assignment of ± 0.6e in the actinide region and considerably less in the (lower-ionisation) $_{79}$Pt-$_{82}$Pb region.

Calibration V_T measurements were made at two different temperatures and linear interpolation was used to adjust the calibration curves to the modal temperature of each UHCRE experimental tray.

3.2.3 *Detector Processing*

The UHCRE detectors were all etched in an aqueous NaOH 6.25N solution at 40°C. As suggested by Fleischer, Price and Walker (1975), this solution was saturated with etch products to a stable plateau where the bulk etch rate (V_G) became independent of the etch product concentration. V_G was monitored by measuring pre- and post-etched strips of Lexan in each of the approximately 40 separate chemical etches. Variations of the bulk etch rate are shown in figure 3.7. Since such variations are accounted for in charge-assignment calculations (and ΔV_G is $\approx$1%) they contribute negligibly to the charge-assignment error.

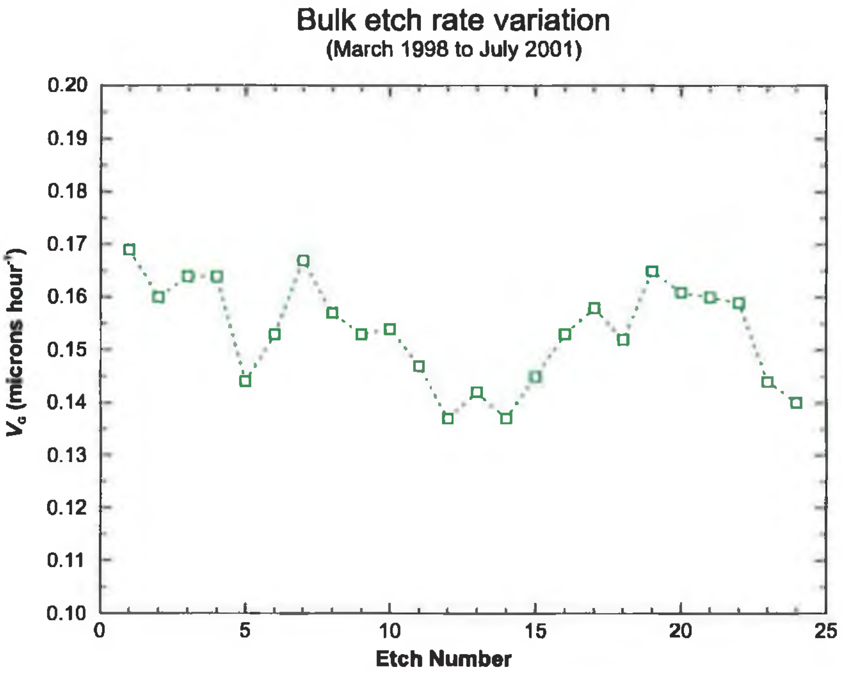

FIGURE 3.7 V_G variation during UHCRE detector processing. Since the error on these average V_G measurements is ≈ 1%, error bars are omitted.

Track etch-rate (V_T) monitoring was facilitated using spare detector material exposed to 10.1 GeV/nucleon^{-1} $_{79}$Au and 158 GeV/nucleon^{-1} $_{82}$Pb nuclei. These track etch rate monitors (or TERMs) provided 80 measurements of V_T for every detector etch. A three-year study discovered a maximum variation in V_T between etches of approximately 10% from the mean (fig.3.8).

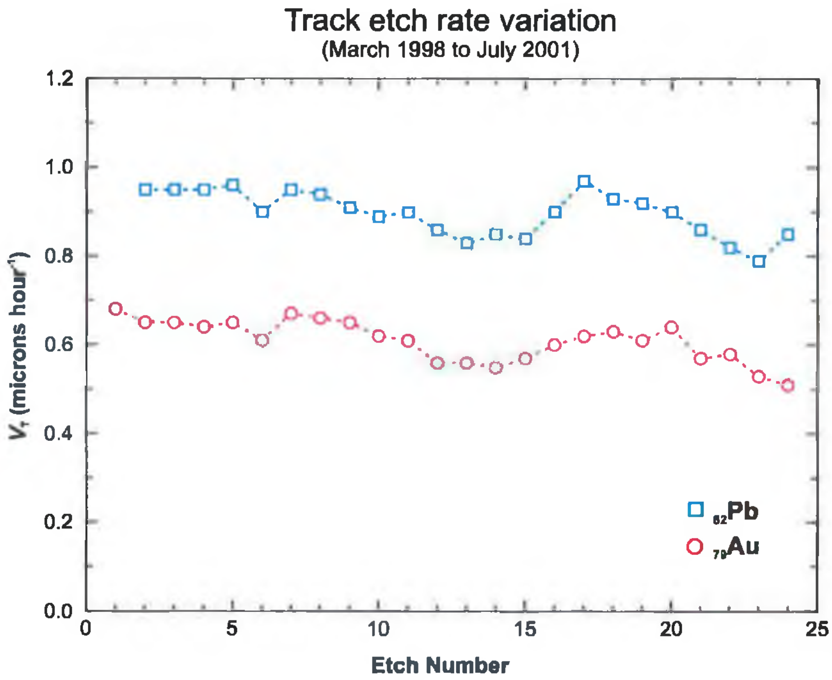

FIGURE 3.8 V_T variation during UHCRE detector processing. Since the error on these average V_T measurements is < 1%, error bars are omitted.

The average V_T of a particular etch was obtained by normalising to the mean of the V_T measurements from all etches. This value was then used to adjust the V_T measurements of all actinide events and remove the effect of etching variations. Compensating for these variations eliminated a mean systematic standard deviation of 7.5% in signal strength (for raw measurements) and 7.1% for filtered measurements. These translate to a charge-assignment error of ± 1.1e in the Pt-Pb region (for both raw and filtered events) and a maximum of ± 1.1e (for raw events) and ± 1.0e (for filtered events) in the actinide region.

3.2.4 *Latent Track Effects*

A latent (unprocessed) damage trail in a track detector is susceptible to thermal annealing, i.e., fading due to storage at a relatively high temperature. The studies of Adams and Beahm (1981) of the annealing of Fe tracks in Lexan reported a 10% reduction in signal strength after storage for one year at +27 °C. Salamon *et al.* (1986) have also shown annealing which is detectable at 0°C over a period of years and significant over several months at room temperature.

It has also been known for some time that the track response of a SSNTD is influenced by environmental conditions such as the atmospheric composition during and immediately after exposure. Samples stored in oxygen at a pressure of 1.7 atmospheres increased logarithmically for at least six months after exposure. This effect is thought to be due to the combination of oxygen with the free radicals of the detector's broken bonds. Those stored in inert gases showed no significant change, while those in a vacuum decreased in track etch rate.

Following 69 months in space at a mean temperature of –20 °C, the UHCRE detectors spent approximately eight months at NASA and ESTEC facilities at room temperature before entering long-term -31 °C storage at the DIAS. The detectors were examined for both annealing and ageing effects.

Previous research at DIAS has shown that latent track effects in the UHCRE are minimal. Twelve detector stacks were exposed to a 0.96 GeV nucleon^{-1} U beam from the heavy ion accelerator at the Lawrence Berkeley Laboratory, California before and after the LDEF mission (May 1983 and May 1990, respectively). Using the pre-flight $_{92}$U beam as calibration, the post-flight ions were successfully identified as $Z = 92.8 \pm 1.3$ e (Bosch 1995). The stability of track response of the UHCRE's detectors over the seven-year mission confirms earlier DIAS studies which saw no indication of long-term aging of latent tracks.

Domingo *et al.* (1990) monitored signal strength in the Lexan detectors from six to eight weeks after exposure for three years (from 1984 to 1987). They detected no significant change in detectors stored at temperatures varying from –70 to +25 °C.

In addition, track etch rate monitors which were exposed to beams of Au and Pb ions (cf. Section 3.2.3), demonstrated no systematic change in V_T after storage at –31 °C for six years. The TERM measurements further illustrate the lack of a detectable systematic effect on latent tracks over a three year period of continuous etching and cold storage.

Other research at the Dublin Institute for Advanced Studies (Bosch, 1995) has shown that as long as thermal annealing is avoided by storing the track detectors at below –25 °C (as was the case with the UHCRE stacks) storage temperature has little effect upon latent tracks. The influence of temperature on latent track response can therefore be restricted to the RTE.1

3.2.5 *Total Charge-Assignment Error*

An estimate of the overall charge-assignment error resulting from the above effects is shown in Table 3.6. Note that the last column displays the total error for the actinide events after the detector processing error has been removed using TERM measurements (cf. Section 3.2.3).

Table 3.6 Mean σ errors for actinide and Pt-Pb ions expressed in fundamental charge units (e)

Z region	Error Bar	Intrinsic[*]	RTE[†]	Detector Processing	Total ΔZ	Total ΔZ[‡]
Actinides ($Z > 88$)	+	1.1	0.6	1.0	1.6	1.3
	-	1.2	0.6	1.0	1.7	1.3
Pt-Pb ($70 \leqslant Z \leqslant 88$)	+	0.6	0.6	1.1	1.4	-
	-	0.9	0.6	1.1	1.5	-

---

[*] Actinide errors are upper-limit estimates, since intrinsic ΔV_T will be smaller for these events.

[†] Pt-Pb errors from the RTE are upper-limit estimates, as this effect is lessened for these lower-ionisation events.

[‡] After variations resulting from the detector processing of actinide events were removed.

The errors agree with, or are larger than, those obtained in previous work (±1.3e for uranium events and ±0.9e for gold events; Bosch, 1994), suggesting that any additional error in calibration measurements is negligible. Section 3.3 describes a Monte-Carlo method used to more accurately determine the intrinsic charge-assignment error by modeling the interaction of cosmic-ray ions of various energies and dip angles in the UHCRE apparatus.

3.3 Monte-Carlo Simulation of Errors

A Monte-Carlo simulation was used to obtain a stochastic estimate of the intrinsic charge spread in the UHCRE detectors. Weighted probabilities for various cosmic-ray energies, cosmic-ray dip angles and detector stack types were calculated. A correctly-weighted distribution of a large number of simulated cosmic rays could then be created. Events in this sample were classified by charge-assignment software identical to that used for genuine GCR events.

3.3.1 *Energy Distribution*

The simulated cosmic rays were distributed in energy according to a doubly-truncated inverse power law (wherein *n*, the number of cosmic rays at a given energy, $\propto E^{-2.6}$). This power law was combined with a geomagnetic transmission function as calculated from the CREME96 website (https://creme96.nrl.navy.mil/). The energy range considered was that for typical UHCRE cosmic rays, i.e., 0.9 to 4.1 GeV/nucleon^{-1}. See Fig. 3.9 (a).

3.3.2 *Dip Angle Distribution*

An ideal planar SSNTD surface under an isotropic flux of cosmic rays will encounter a flux proportional to $\frac{1}{2}\sin 2\theta$. This distribution reaches a maximum at $\theta = 45°$ and a minimum when $\theta = 0°$ or $90°$. Clearly, this will alter the distribution of dip-angles in an incoming isotropic flux of GCRs.*

In addition, the LDEF's low-earth orbit meant that a sizeable portion of the sky surrounding the spacecraft was screened by the disc of the earth. This earth "shadow" thus reduces the experiment's collecting power in a trajectory-dependent manner and further complicates the dip angle distribution of the cosmic-ray flux. The following expression defines the Earth's horizon (i.e., the edge of the shielded area) as a function of an incident GCR's dip angle (θ) and azimuthal angle (ϕ):

$$\sin^2\theta \leqslant 1 - \sin^2 \alpha_h / \sin^2 \phi,$$

where α_h is the angle between the earth's horizon and the azimuthal angle, ϕ.† This function is plotted in fig 3.9 (b) and will clearly influence GCR flux as a function of θ.

---

* The charge-dependent thresholds inherent in the UHCRE's detector efficiency which were described in Section 2.4.2 will also alter the the distribution of dip-angles of the incoming flux as a function of θ. Only ions both above and to the right of the red and blue lines respectively in fig 2.3 will register in the detector. However, these cutoffs will only affect ions of $Z \leqslant 79$.

† For the LDEF spacecraft's orbit, $\alpha_h = 20 \pm 2$ °.

The combined effect of both the earth “shadow” and θ-dependent detector efficiency is shown in figure 3.9 (c). This function is used to assign dip angles to Monte-Carlo-simulated cosmic rays.

3.3.3 *Stack Composition*

As described in Section 2.3, UHCRE SSNTD stacks were of several different compositions, any of which may interact with the trajectory of a simulated cosmic ray event. Weighted probabilities were used to determine the frequency of each stack composition.

3.3.4 *Results*

A simulation was performed with 100,000 Monte-Carlo-generated $_{92}$U cosmic rays. The distribution of dip-angles is shown in fig 3.10 (a). Note the similarity to that of the theoretical dip-angle distribution in fig 3.9 (c).

The point-spread function of 10,000 of these events is shown in fig 3.10 (b). As expected, it is gaussian (or pseudo-gaussian) with a mean Z of 92.0 e and a standard deviation of 0.8 e. This is fully consistent with the upper-limit empirically-derived estimates of intrinsic error on the actinides of + 1.1e and -1.2 e (see Section 3.2.1). This Monte-Carlo value is also consistent with earlier DIAS work which estimated the low-energy (i.e., maximum) intrinsic σ_Z for $_{92}$U to be 1.3 e (Bosch, 1995). The Monte-Carlo simulation thus corroborates the empirical error estimates collated in Table 3.6.

Summary

The energy-loss model used by the UHCRE has demonstrated its ability to successfully identify the charges of incident relativistic nuclei (Sections 3.1.5 and 3.2.4).

Errors arising from detector processing, intrinsic detector anomalies and temperature variations have been studied. The discovery of a V_T variation between detector etches is of great importance. The results of correcting for this large (~10%) effect on signal strength in the detector can be seen in Section 4.3.2.

These investigations of charge-assignment errors in the UHCRE (as well as a Monte-Carlo simulation) have yielded results in broad agreement with previous DIAS research. Assuming a gaussian distribution, the maximum total Z-assignment errors were +1.4e/-1.5e in the subactinide region and ±1.3e for the actinides. The effects of these errors on the more important charge abundance ratios are presented in Section 4.6.

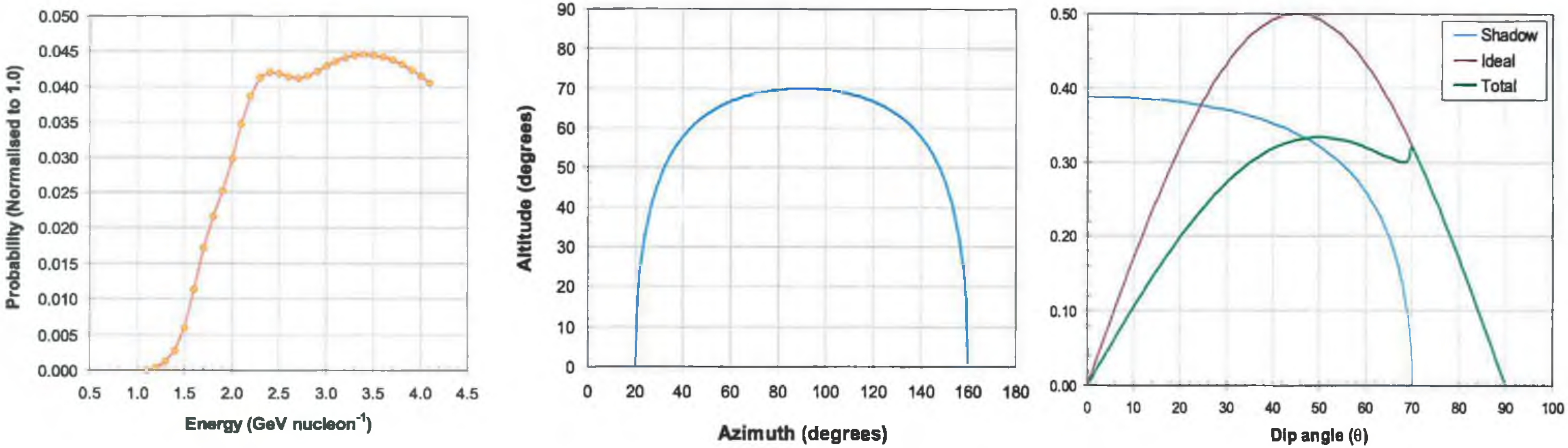

(a) (b) (c)

FIGURE 3.9 (a) Distribution of the kinetic energies of simulated $_{92}$U GCRs. (b) The Earth's horizon as seen from an UHCRE experimental tray as a function of dip angle (θ) and azimuthal angle (ϕ). (c) Distribution of GCRs as a function of dip angle due to: the earth's shadow, an isotropic flux on an ideal detector and the resulting total effect. This last is used to determine the dip angles of simulated cosmic-ray events.

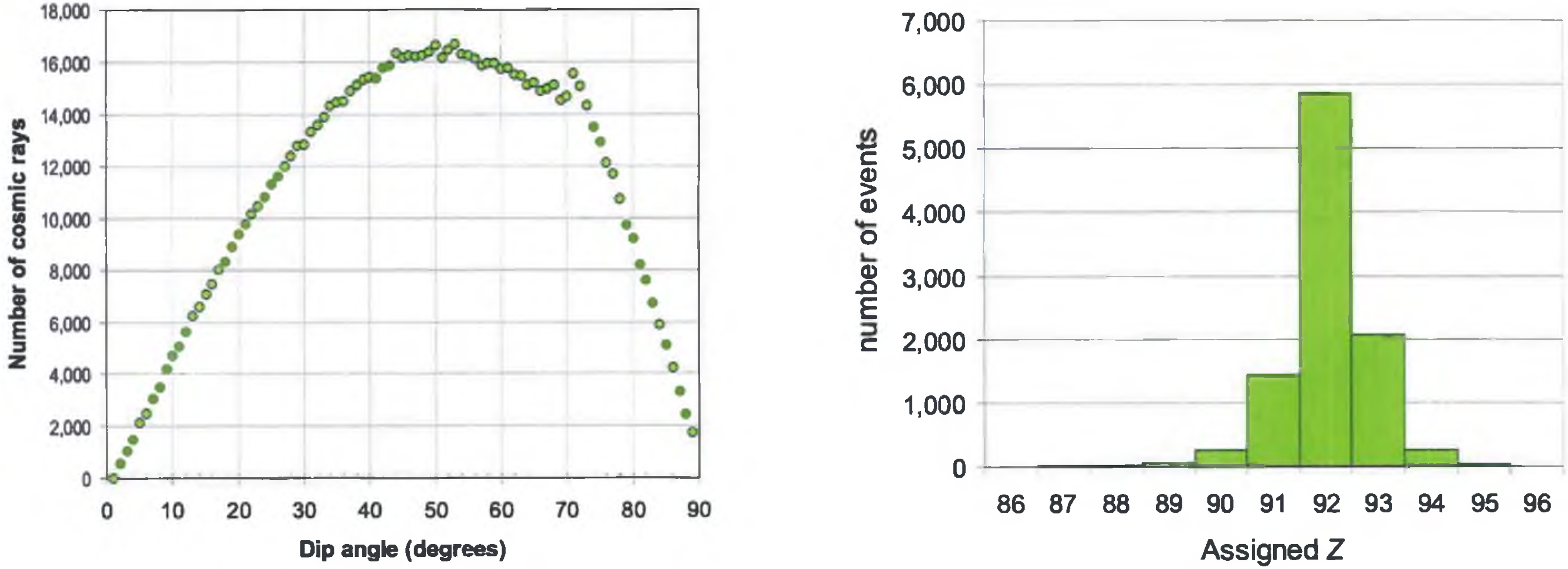

(a)

(b)

FIGURE 3.10 (a) The dip-angle distribution of 100,000 Monte-Carlo simulated cosmic-ray events. (b) Charge distribution of 10,000 Monte-Carlo-simulated $_{92}$U cosmic rays. ($\overline{Z} = 92.0$ and $\sigma = 0.8$ e)

4. Results

The hundreds of manually-measured events from the UHCRE comprise the largest currently existing database on ultra-heavy cosmic rays. Stringent controls were applied to reduce systematic and statistical errors on these data (c.f. Chapters 2 and 3).

This chapter describes the methods used to compensate for these errors and presents the resulting final charge abundance spectrum. Section 4.1 describes the unprocessed data while Sections 4.2 and 4.3 discuss data-filtering and the corrections imposed for various detector and etching biases. The discovery of an important detector-processing error for actinide events is explained. Section 4.4 describes the procedure used to compensate for cosmic-ray fragmentation in the UHCRE apparatus and the LDEF. Finally, Section 4.5 presents the final inferred spectrum of cosmic rays outside the spacecraft.

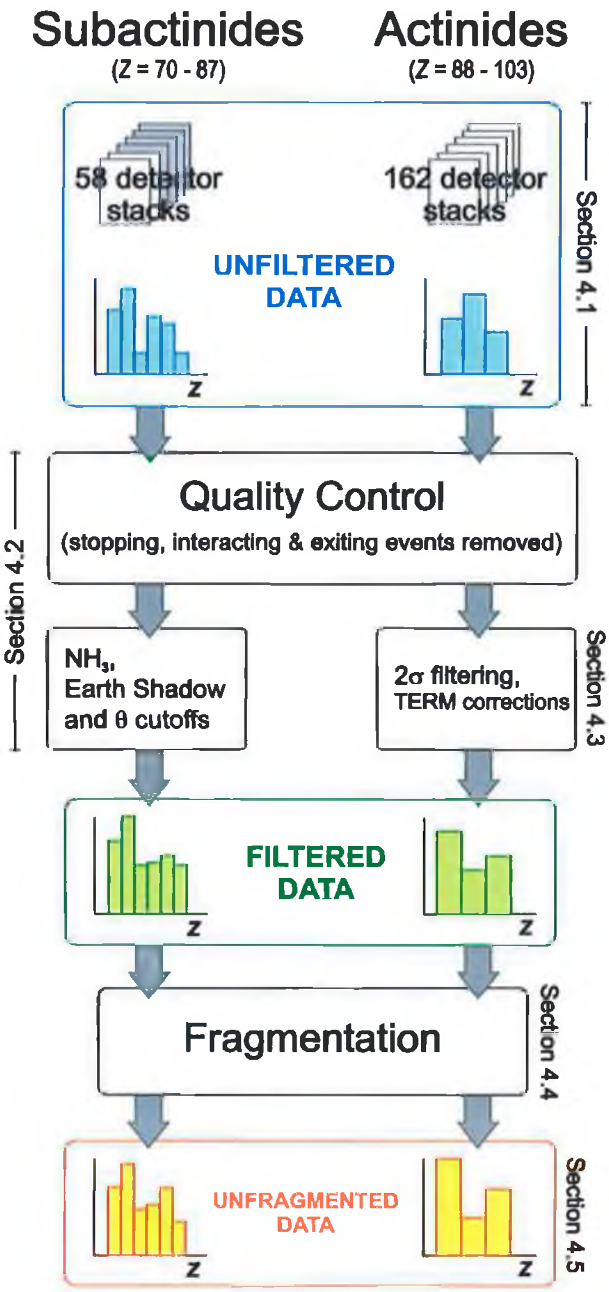

FIGURE 4.1 Processing the UHCRE data.

Firstly, the data extracted from the detectors are presented in an unfiltered form (Section 4.1). These data were corrected only for bulk etch-rate variations in the etch tank. Secondly, the abundances of elements around $_{78}$Pt and $_{82}$Pb were processed for quality control and to correct detector biases (Section 4.2). Thirdly, the actinide abundances were corrected for quality control and track etch rate (V_T) variations during the etching procedure (Section 4.3). Finally, all elemental abundances were corrected for fragmentation within the detector (Section 4.4). The charge spectra resulting from all of these adjustments are presented in Section 4.5.

Actinide ($88 \leqslant Z \leqslant 103$) and subactinide[§] ($70 \leqslant Z \leqslant 87$) cosmic rays were collated using different methods. The former were extracted from all 162 accessible detector stacks. The latter derived from a subset of 58 stacks in which all ultra-heavy nuclei events were measured.

4.1 Uncorrected Data

4.1.1 *Subactinide Charge Spectrum*

Table 4.1 Total numbers of Detected Events in 162 accessible stacks (unprocessed data)[*]

Charge region	58 stacks	104 stacks	UHCRE
Pt-Pb ($Z \geqslant 70$)	643	-	-
"Actinides"[†] ($Z \geqslant 88$)	15	18	33
All charges[‡]	919	1842	2761

Of the UHCRE's 192 detector stacks, only 162 were accessible (i.e., possessed a standard atmosphere during the mission *and* were uncompromised by calibration beam exposures). Of these, 58 were pseudo-randomly selected to provide an unbiased sample from the LDEF spacecraft. The ammonia-scanning technique (c.f. Section 2.4.2) was used to locate every $Z \geqslant 70$ event in these stacks. These events were subsequently measured and their dip angles and estimated charges were compiled into spectra (figs. 4.2 and 4.3).

The remaining 104 accessible stacks were ammonia-scanned and the numbers of events in each recorded. Estimates of the total number of ultra-heavy (i.e., $Z > \approx 60$) events collected in the UHCRE's 162 accessible stacks are collated in Table 4.1. Note that these data are unprocessed and that more accurate abundance estimates can be found in Section 4.5.

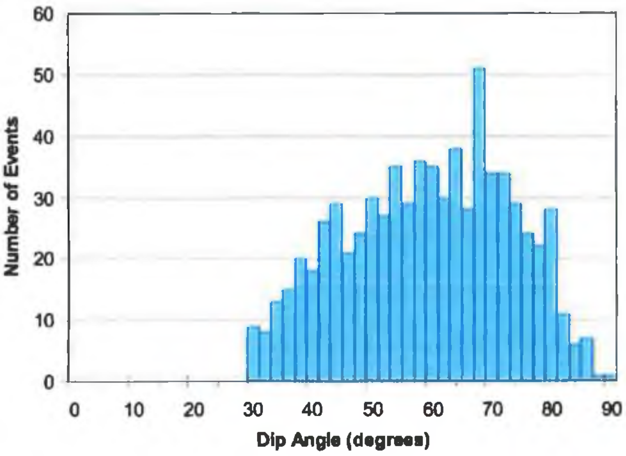

FIGURE 4.2 The distribution of dip angles (θ) in the subactinide sample. Note the similarity to the overall theoretical spectrum in fig. 3.9 (c).

---

[*] These 162 stacks represent the entire accessible detector surface area of the UHCRE. This result is geometrically weighted as described in Section 4.1.2. The number of $Z \geqslant 70$ events detected was 2596.

[†] Here, the term "actinide" denotes particles of $Z \geqslant 88$, although more formally the term refers to $89 \leqslant Z \leqslant 103$.

[‡] Note that this is *not* the sum of the rows above as these data do not include events of $Z < 70$.

[§] i.e., those elements in the ${}_{78}$Pt and ${}_{82}$Pb-region.

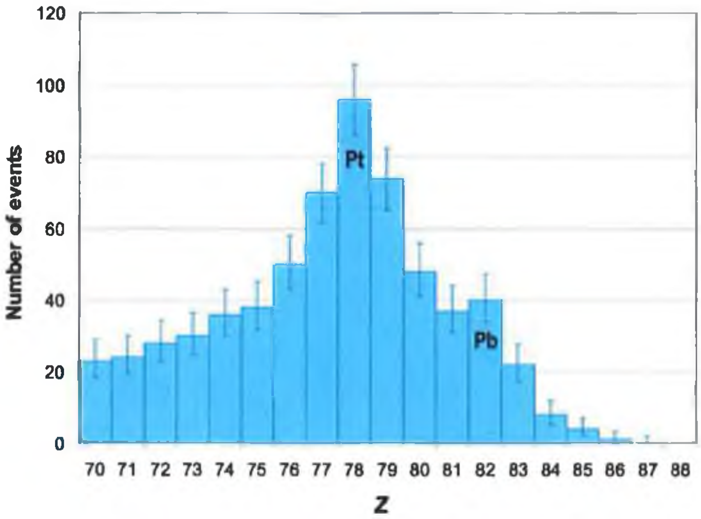

FIGURE 4.3 Subactinide abundance spectrum for 629 events (1σ statistical error bars are shown).

4.1.2 *Actinide Charge Spectrum*

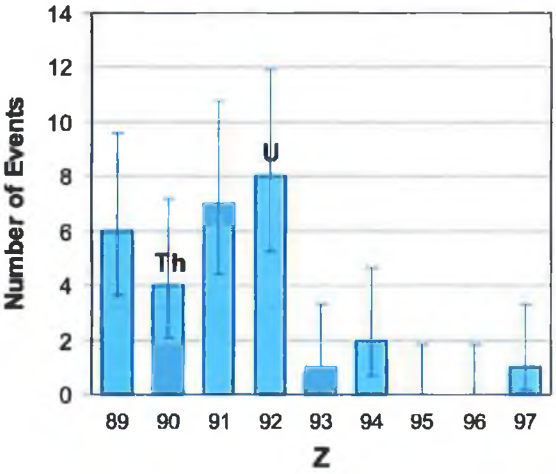

FIGURE 4.4 Abundance spectrum for 33 actinides (derived from all 162 UHCRE detector stacks). 1σ statistical error bars are shown.

To compile a charge-spectrum of $89 \leqslant Z \leqslant 103$ events *actinide skimming* was employed. This variant on the actinide scanning technique (c.f. Section 2.4.2) involved reducing the ammonia-etch time so that only events with very high values of V_T could form 'tunnels' through the polycarbonate plate. This technique was used to locate the complete sample of actinide events in the remaining 104 unprocessed stacks (fig. 4.4).

Note that the numbers of events in figs. 4.3 and 4.4 *cannot* be directly compared as they derived from different sample sizes. However, the *frequency* histograms in Sections 4.2, 4.3, 4.4 and 4.5 allow for such comparisons.

Even given the unfiltered nature of the above spectra, some features are already apparent. $_{78}$Pt and $_{82}$Pb peaks are visible in the subactinides. The former is clearly larger than the latter, in stark contrast to the relative abundances found in solar-system material. As expected, the abundances fall off from the $_{82}$Pb peak, as the elements immediately heavier than $_{83}$Bi are quite unstable. Thus a gap in abundance is expected between the subactinides and the actinides. This natural division is useful as it allows us to treat subactinide events separately from the actinides. The presence of actinides is confirmed, though in the raw sample no ${}_{90}$Th or ${}_{92}$U peaks are visible. One very high charge event ($Z = 97$) is also present.

4.2 Corrected Charge Spectrum (subactinides)

As described in Section 2.4.2, the following quality-control measures were applied to the sample:

1) Events stopping in stack were eliminated[*]
2) Events interacting in stack were eliminated
3) Events exiting the stack area (i.e., moving off the edge of the stack) were eliminated and
4) Events with dip angles < 30° were eliminated.

The effect of detector and earth-shadow geometry were to apply the following additional selection criteria to the events:

4) An ammonia-scanning threshold[†] and
5) A limiting dip angle threshold[‡].

Fig. 4.5 (a) shows the angular cutoffs imposed on elements of various Z by the last three of the above criteria. GCRs above the 30° line and to the right of the Z-dependent cutoff will be accepted. Clearly, a method of compensating for the lack of events with dip angles falling between 30° and the Z-dependent cutoff is required.

Firstly, any anomalous events falling within this dip-angle range were removed from the sample. Secondly, the range in question (e.g., for Z=70, the dip angle range is θ = 30-79°) was considered. The fractional area under the 'total' dip-angle bias curve in fig. 4.5 (b) that corresponds to this dip-angle range is assumed to equal the fraction of events that go undetected due to Z-dependent cutoff, adjusted for detector and earth-shadow effects. The original abundance of each element is adjusted upwards using this fraction. This procedure is only necessary for events of $Z \leqslant 78$ as, at these energies higher-ionisation events are all above the Z-dependent threshold.

---

[*] i.e., those falling below the registration threshold of the detector.

[†] i.e., ($V_T \sin\theta \times$ etch time) must be > ½ the detector plate thickness to be detected.

[‡] To form a track, $V_T \sin\theta$ must be > V_G. Therefore, for a cosmic ray of given Z subjected to etching conditions with a given V_G, an etch cone will not form below some limiting dip angle (θ_{cutoff}).

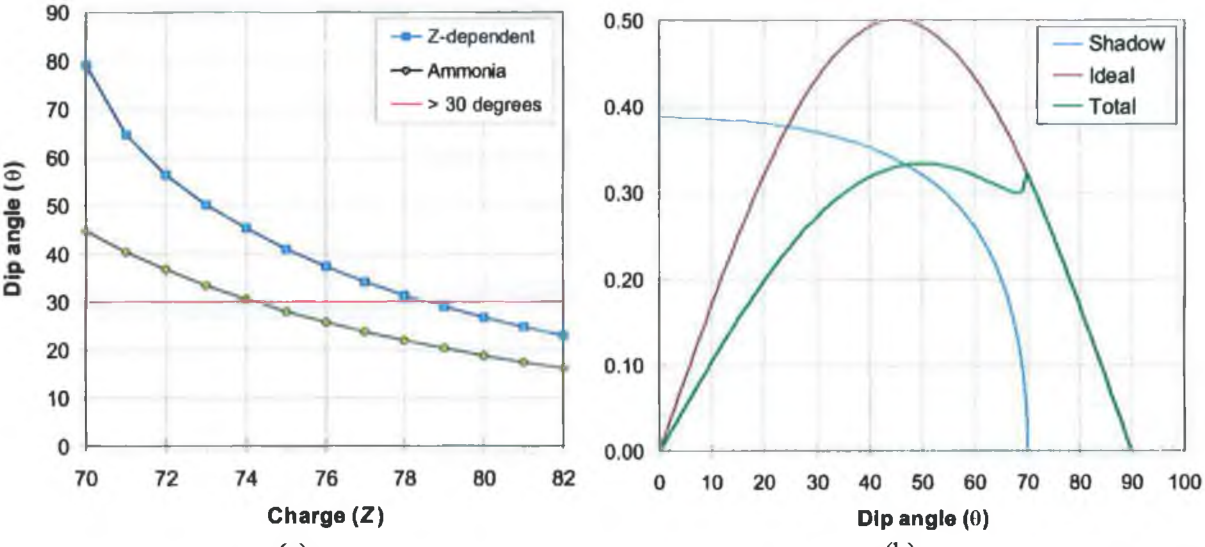

(a) (b)

FIGURE 4.5 (a) Z-dependent angular cutoffs for $Z > 70$ GCR events in the UHCRE (at -20°C and 5 GeV nucleon^{-1}). (b) Distribution of GCRs as a function of dip angle due to: the earth's shadow, an isotropic flux on an ideal detector and the resulting total effect.

The results are presented in Table 4.2 and the adjusted histogram is plotted in fig 4.6 (note that here, *frequency* abundances are quoted).

Table 4.2 Measured and weighted elemental abundances

Charge	No. of events	Dip angle range	Fractional area	Removed events	Adjusted no. of "events"	**Frequency**[*]
70	23	30-79	0.74	19	15.6	**0.023**
71	24	30-65	0.56	12	27.2	**0.040**
72	28	30-56	0.42	7	36.1	**0.054**
73	30	30-50	0.32	1	42.7	**0.063**
74	36	30-45	0.24	5	40.8	**0.060**
75	38	30-41	0.18	1	44.9	**0.067**
76	50	30-37	0.11	2	54.2	**0.080**
77	70	30-34	0.07	3	72.0	**0.107**
78	96	30-31	0.03	0	98.7	**0.146**
79	74	-	-	-	74.0	**0.110**

---

[*] Frequencies are relative to the estimated total number of ($Z \geqslant \sim70$) events in the UHCRE's 162 accessible detector stacks, in this case adjusted for the geometrical effects described in this section.

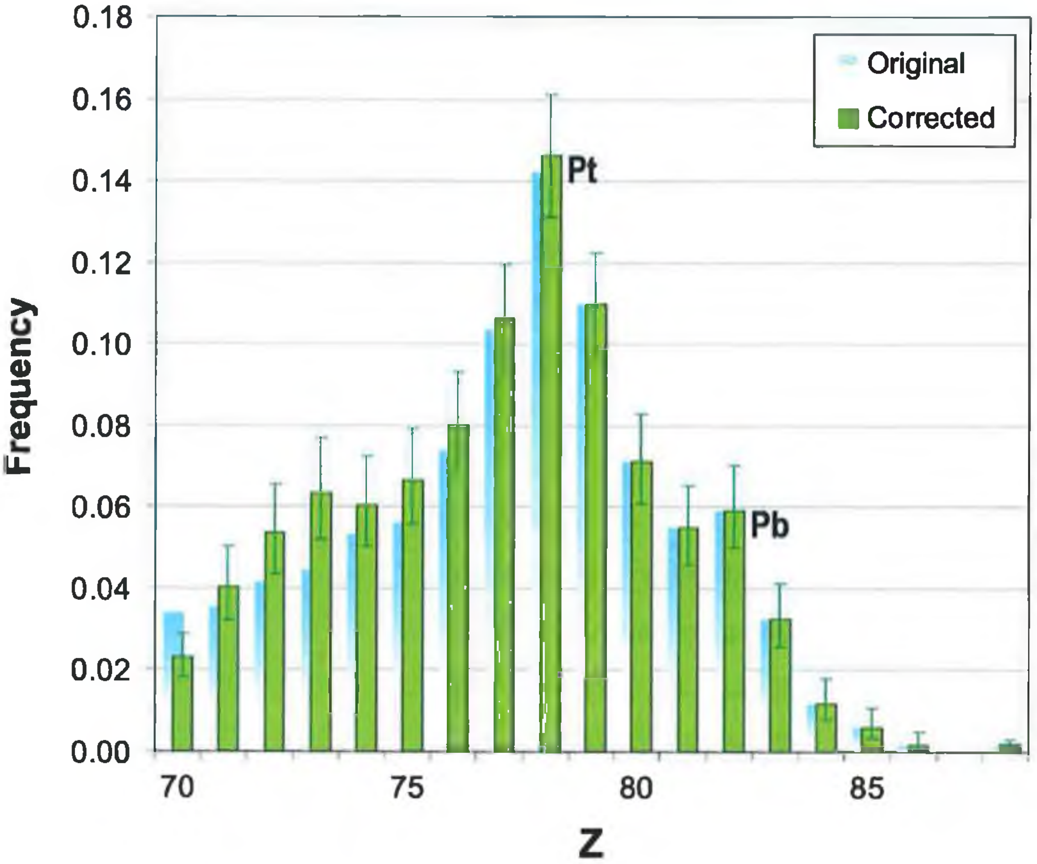

FIGURE 4.6 Charge histogram of 629 measured Pt-Pb ($70 \leqslant Z \leqslant 87$) events adjusted for the effects of cutoffs, thresholds, detector bias and the screening influence of the Earth. Frequencies are relative to the estimated total number of events in the UHCRE's 162 accessible detector stacks. Error bars correspond to 1σ (c.f. Gehrels, 1986).

4.3 Corrected Charge Spectrum (actinides)

4.3.1 *Quality Control*

The quality control measures which were applied to Pt-Pb events (as described in Section 4.2) were also applied to all actinide events. Namely, events which stopped in the stack, interacted in the stack, exited the stack area or had dip angles < 30° were eliminated. In addition, non-linear curve fitting was applied to each actinide candidate's V_T-gradient data. Any measurements deviating by more than 2σ from this curve were removed (e.g., fig. 4.7). 2σ filtering led to the removal of ~8% of actinide detector plates. See Appendix *B* for quality control plots and other details of all detected actinides.

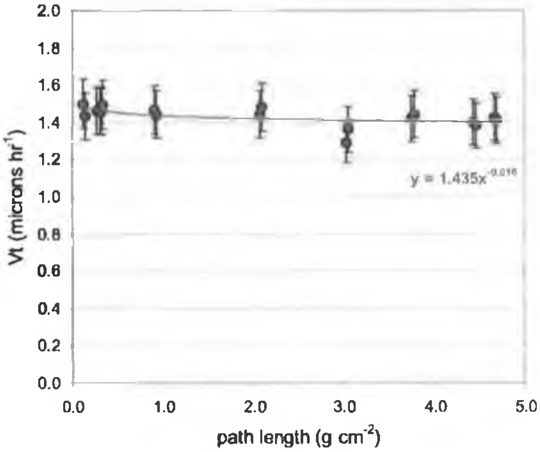

FIGURE 4.7 An actinide (in this case, a $_{90}$Th event) with non-linear curve fitting and 2σ error bars.

4.3.2 *Track etch-rate adjustments*

A further improvement of actinide charge resolution became possible with the discovery of a variation in V_T due to changing etching conditions in the chemical etch tank (see figs. 3.8 and 4.8). This variation contributed a mean error to V_T measurements between etches of ~10%. As explained in Section 3.2.3, the average V_T of a particular etch was obtained by normalising to the mean of the V_T measurements from all etches. This value was then used to adjust the V_T measurements of actinide events and remove the effect of etching variations. Compensating for these variations eliminated a mean maximum standard charge-assignment error of ± 1.0e (for processed actinide events).

Actinide abundances before and after etching variations have been removed are shown in Table 4.3. The frequencies shown are relative to the entire UHCRE sample of $Z > 70$ events.

Table 4.3 Actinide abundances before and after V_T adjustment

	Original		**Etching Variation Removed**	
Charge	No. of events	Frequency*	No. of events	Frequency*
88	4	0.0014	5	0.0018
89	6	0.0022	2	0.0007
90	**4**	**0.0014**	**11**	**0.0040**
91	7	0.0025	4	0.0014
92	**8**	**0.0029**	**8**	**0.0029**
93	1	0.0004	3	0.0011
94	2	0.0007	1	0.0004
95	0	0.0000	0	0.0000
96	0	0.0000	1	0.0004
97	1	0.0004	0	0.0000
Total	**33**	**0.0120**	**35**	**0.0127**

Figure 4.9 shows the improvements gained by applying quality control, by filtering data >2σ from a fitted curve and by eliminating etching variations. Prominent $_{90}$Th and $_{92}$U peaks are now visible. In addition, the event which was previously assigned a charge of 97 ($_{97}$Bk) is now $_{96}$Cm – a more plausible candidate because $_{97}$Bk has a very short half-life, while the longest-lived isotope of $_{96}$Cm has a half-life of 15.6 Myr.

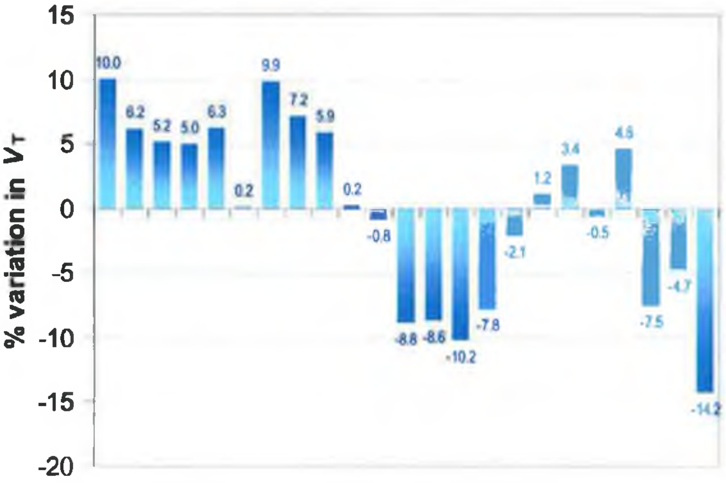

FIGURE 4.8 Percentage variation in V_T over a number of different etches.

Note that this track etch-rate adjustment has a larger effect on the relative abundances of the actinides than those outlined in Section 4.3.2. V_T-gradient curves and further details of every actinide event are presented in Appendix *B*.

---

[*] Frequencies are relative to the estimated total number of $Z \geqslant 70$ events in the UHCRE's 162 accessible detector stacks, in this case adjusted for the geometrical effects described in section 4.3.2.

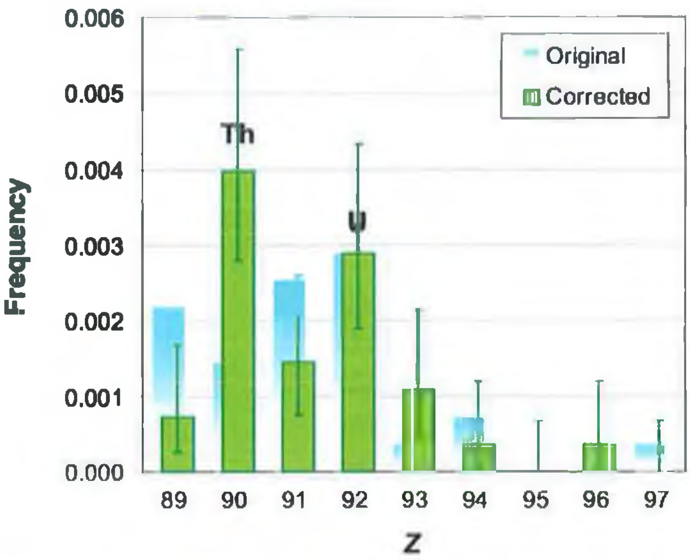

FIGURE 4.9 Corrected histogram of 35 actinide (i.e., $Z \geqslant 88$) events. Note the prominent $_{90}$Th and $_{92}$U peaks in the new spectrum. Statistical Error bars correspond to 1σ (c.f. Gehrels, 1986).

4.4 Fragmentation Corrections (actinides & subactinides)

A cosmic-ray nucleus will interact with atoms of both the interstellar medium and the detector apparatus itself. The cross-sections of these charge-changing nuclear interactions depend on the projectile type. Since heavier elements are particularly susceptible, the charge-frequency histogram of the GCR flux will therefore show a paucity of these elements in comparison to that at the top the detector. In addition to these central collisions in which the nuclei are totally disrupted, peripheral collisions resulting in so-called "spectator nuclei" must be considered. When measuring the GCR charge spectrum, fission interactions lead to an underestimation of the flux in each particular bin, while peripheral interactions can be seen as "polluting" the lower bins with their lower-charge reaction products. This effect is seen on a much grander scale in the abundances of Li, Be and B, whose presence in the Galaxy is largely due to spallation of heavier nuclei in the interstellar medium.

Obtaining the cosmic-ray abundances at the top of the detector is thus critically dependent on using accurate partial ($\sigma_{partial}$) and total (σ_{total}) cross-sections for the appropriate projectile, projectile energy and target. Before the advent of relativistic heavy-ion accelerators, such cross-sections could be determined only for certain radioactive isotopes produced by proton bombardment of target nuclei. Cross sections of heavier targets were subsequently inferred by semi-empirical extrapolations. Data from the Lawrence Berkeley Laboratory Bevelac accelerator (limited to energies of ~1 A GeV for ultra-heavy nuclei) indicated that many of the important charge-changing fragmentation cross sections were still varying at this maximum energy. Energy independence (i.e., limiting fragmentation) for the heavy nuclei could only be reached later by the Brookhaven National Laboratory Alternating Gradient Synchrotron (or AGS). This facility accelerated ^{197}Au nuclei to 10.6 A GeV. The AGS detector array measured cross sections for the charge-change in each target and $\sigma_{partial}$ for the fragmentation of $_{79}$Au nuclei to elements with charges from ~ 50 to 80. However, the impracticality of measuring every permutation of target and projectile at various energies necessitates parameterisation of the cross-sections based on relevant variables.

A useful assumption in formulating these models is that of *factorisation*. Olson *et al.* (1983) have shown that for iron and lighter nuclei, projectile and target dependences can be separated and it seems reasonable to apply this principle to heavier nuclei.

Factorisation is based on the concept that the cross section for a given projectile and target can be separated into two factors: one that is independent of the target and one that is independent of the fragment. The cross section for the production of a fragment F from a projectile nucleus P interacting with a target nucleus T can be written:

$$\sigma\,(F,P,T) = \gamma(F,P)\;\eta(P,T)$$

where $\gamma(F,P)$ depends only on the species of projectile and fragment but not on the target and $\eta(P,T)$ depends only on the projectile and target but not on the fragment. This is "weak factorisation". "Strong factorisation" restricts the second dependence to the target only. The above equation is taken from Olson *et al.* (1983).*

4.4.1 *Total Nuclear Interaction Cross-Sections (σ_{total})*

The UHCRE sample contains only events which completely penetrate the detector stack. Fragmentation in the detector will reduce the measured abundance of all elements in the sample in a charge-dependent manner, and so distort the charge abundance spectrum. Thus, σ_{total} must be calculated for each element and used to adjust the elemental abundances upwards to their pre-fragmentation levels outside the LDEF spacecraft.

A number of theoretical models have been suggested to formally calculate total cross-sections. A (by no means exhaustive) sample of the reported data and models is shown in Table 4.4. The semiempirical parameterisation of measured data by Silberberg and Tsao (Silberberg & Tsao, 1990; Sihver *et al.*, 1993; Tsao *et al.*, 1993) is based on proton bombardment of heavy targets. Though accurate to within 35%, this parameterisation introduces a number of non-physical discontinuities in the partial cross sections and uses a large number of parameters and special cases, leading to a complicated algorithm. Though

---

* Olson *et al.* examine three theoretical models: an *opaque disk geometrical* model of colliding nuclei, *abrasion-ablation* theory and an *excitation* model.

In the *opaque disk geometrical model*, $\eta(P,T)$ is proportional to an impact term of the form $(A_P^{1/3} + A_T^{1/3})$ – the combined radii of the projectile and target nuclei, and $\gamma(F,P)$ is the width of an annular band on a disk of this radius and contains details of the physics of the interaction.

In the *abrasion-ablation* model, when two high-energy nuclei collide, the overlapping portion of their volumes is sheared away (abrasion). The remaining spectator portion of the projectile maintains essentially the same velocity but is highly excited by the abrasion. It subsequently decays, emitting γ-radiation or nuclear particles – the ablation stage. The predictive accuracy of abrasion-ablation models has been hampered by the need to estimate the (unknown) pre-fragment excitation energy. The cross-section equation for abrasion-ablation violates the factorisation principle because the fragmentation channel depends on the impact parameter (and thus on the target). If measured data on much heavier projectile nuclei were consistent with factorisation, this would be an argument against the abrasion-ablation model.

The *excitation* model follows factorisation with $\eta(P,T)$ proportional to the sum of the target and projectile nuclear radii plus a constant and $\gamma(F,P)$ proportional to an integral over excitation energies of the probability for producing a given energy in a collision involving one nucleon in the projectile nucleus, times the probability for that level of excitation to produce the given fragment.

abrasion-ablation models (see footnote on previous page) have provided acceptable fits to previously published measurements, those of Townsend *et al.* (1993) and Badavi *et al.* (1987) were unable to predict the data of Nilsen *et al.* (1995) for ^{84}Kr and ^{109}Ag projectiles in targets ranging from H to Pb. Traditional hard-sphere models have proven more effective.

Table 4.4 Reported total cross section (σ_{total}) data gathered from beam exposures

Author(s)	Projectile(s)	Target(s)*	Energies (GeV)
Silberberg & Tsao (1973)	H	Li → Ni	> 0.1
Westfall *et al.* (1979)	Fe	H, Li, Be, C, S, Cu, Ag, Ta, Pb	1.88
Greiner (1985)	U	H → Pb	0.9
Binns *et al.* (1987)	Kr, Xe, Ho, Au	H, Al, C, CH_2	≈1 (for Au)
Cummings *et al.* (1990)	Kr, Xe, La, Ho, Au	H, C, Cu, Al,	< 1 (for Au)
Nilsen *et al.* (1994)	Ag, Kr	H → Pb	10.6 0.5 - 1.4
Geer *et al.* (1995)	Au	CH_2 → Pb	10.6
Hirzebruch *et al.* (1995)	Au	H → Pb	10
Nilsen *et al.* (1995)	Ag Kr	H → Pb	0.67 - 1.5 0.47 - 1.4
Waddington *et al.* (1995)	Au	H → Pb	10
Bhattacharyya (1997)	U	Al	0.9
Waddington (1999[a, b])	Au	H → Pb	0.9 - 4

In the simple hard sphere model, first introduced by Bradt and Peters (1950), the total cross section is that of a pair of hard spheres colliding with a small overlap:

$$\sigma(R_P, R_T) = \pi(R_P + R_T - \Delta R)^2$$

where R_P and R_T are the projectile and target nuclear radii and are usually taken as $R = r_0 A^{1/3}$, with A being the mass number of the nucleus and ΔR, the overlap parameter, is written as $\Delta R = r_0\delta$, with r_0 and δ to be determined.

Using ^{56}Fe nuclei accelerated at the Bevelac to 1.88 A GeV targets ranging from hydrogen to uranium, Westfall *et al.* (1979) derived values of $r_0 = 1.35 \pm 0.02$ fm and $\delta = 0.83 \pm 0.12$ for the Bradt-Peters form, but found it necessary to assign $A_H = 0.089$ for a hydrogen target. This relation assumes that the overlap required before a charge-changing

---

[*] '→' indicates a range of elements; e.g., H → Li denotes hydrogen through lithium inclusive.

interaction occurs is mass-independent and that a nucleus has a radius given by $r_0A^{1/3}$. They suggest that there is no significant energy dependence in σ_{total} from a few hundred MeV nucleon^{-1} to about 2 GeV nucleon^{-1}, limits which fortunately correspond to those of the UHCRE data. This energy-independence greatly simplifies the treatment of fragmentation within the detectors.

An earlier expression proposed by Hagen (see Nilsen *et al.*, 1995 and references therein) fits most of the same data by the relation:

$$\sigma(A_P, A_T)_{Ha} = 10\pi(1.29)^2\{A_T^{1/3} + A_P^{1/3} - 1.189\exp[-0.05446\min(A_T, A_P)]\}^2\, mb$$

This equation assumes a mass-dependent overlap, where min(A_T, A_P) is the lesser of and A_T and A_P. In this case, A_T for hydrogen is set to 1, though the model does not provide a good fit to the hydrogen data. Results from this model also show poor agreement with those of Nilsen *et al.*(1995) and Westphal *et al.* (1979) and we do not consider it further.

Binns *et al.* (1987), used heavier projectiles (Kr, Xe, Ho and Au) in targets varying from hydrogen to aluminium and a modified overlap term: $\Delta R = r_0\delta(A_P + A_T)^{\varepsilon}$, with $\delta = 0.209 \pm 0.003$ and $\varepsilon = 1/3$, while maintaining Westfall *et al.*'s values for r_0 and A_H. Physically, this expression corresponds to an overlap model with the overlap dependent on the masses of both nuclei involved. These modifications were consistent with Westfall *et al.*'s cross section measurements for the lighter projectiles and yielded an improved representation of the behaviour of the heavier projectiles.

Hizebruch *et al.* (1995) also measured total cross sections using BP-1 glass track detectors with similar Au projectiles from the AGS. These results are in excellent agreement with those of Geer *et al.* (1995) who report charge-changing cross sections of 10.6 GeV nucleon^{-1} Au ions in targets of polyethylene (CH_2), C, Al, Cu, Sn and Pb.

Webber *et al.* (1990) fitted measurements of Bevalac projectiles of carbon to nickel on targets of hydrogen, helium and carbon, using an overlap term of the form: $\Delta R = r_0[\delta - \varepsilon A_T - b' A_P^{1/3} A_T^{1/3}]$, with r_0=1.35 fm, δ=1.0074, ε=0.013 and b'=0.048. However, the lack of symmetry between the projectile and target nuclei in this form leads us to not consider it further.

Nilsen *et al.* (1995) report total cross-sections for $_{36}$Kr and $_{47}$Ag nuclei in targets of from $_1$H to $_{82}$Pb. They fit the cross sections from these measurements with new parameters in the hard sphere models, without regard to energy.* These fits are performed both with

---

* None of these new fits to the $_{36}$Kr and $_{47}$Ag data, however, have χ^2 values lower than approximately 6.59.

and without the inclusion of ten additional Bevelac cross sections (reported by Binns *et al.*, 1987) and six additional higher energy AGS 10.6 A GeV Au projectile cross sections from Geer *et al.* (1995)[*]. Inclusion of these additional cross sections resulted in lower χ^2 values, most likely because of the inclusion of more values at the higher energies (where the energy dependence of the cross sections appear to be reduced).

Furthermore, Nilsen *et al.* modified the assumption that $R \propto A^{1/3}$ to obtain a somewhat better fit to the measured total charge-changing cross sections. Electron scattering experiments (Collard *et al.*, 1967; de Vries *et al.*, 1987) have determined nuclear charge radii, R_e. These are a function of atomic mass of the form $R \propto A^{0.281 \pm 0.003}$, which differs significantly from the commonly used $A^{1/3}$. They demonstrate that using these nuclear charge radii reduces the fluctuations in cross section calculations and brings the cross sections of higher-charge nuclei into concord with those of lower charges. Another advantage of this approach is that it is no longer necessary to treat hydrogen as an exception. The results show some improvement in χ_v^2 from previous calculations.

They have replaced the reliance on mass numbers in the hard sphere models with a dependence on R_e and introduced a scaling factor (S) to generate nuclear (R_n) rather than electronic measured charge radii. Thus, they replaced $r_0\delta$ with a new variable (α) and $r_0A^{1/3}$ with SR_e.

Nilsen *et al.* used the following equation to determine the total cross sections:

$$\sigma\,(R_P, R_T, E) = \pi\, F(E)[\, R_P + R_T - (8.9 \pm 1.4)G(E)]^2$$

where $$F(E_T) = 1 - (1.61 \pm 0.16)\ln(E) + (1.18 \pm 0.14)\,[\ln(E)]^2$$

and $$G(E_T) = 1 - (1.51 \pm 0.20)\ln(E) + (1.04 \pm 0.18)\,[\ln(E)]^2$$

Table 4.5 Best-fit hard-sphere parameters for elements relevant to UHCRE fragmentation (Nilsen *et al.*, 1995)

Element	R_e (fm)	R_n (fm)[†]
Al	3.75	6.75
Au	6.81	12.26
Pb	7.04	12.67

---

[*] These latter were corrected for electromagnetic dissociation, which is insignificant at the lower energies of the Berkeley Bevelac accelerator.

[†] $S = (1.80 \pm 0.09)$ provided the best fit to experimental data and so $R_n = 1.80R_e$.

The best-fit parameters for this model are those which incorporate the ten additional values of σ (*P*,*T*,*K*) from Binns *et al.* (1987) but *not* the six additional values from Geer *et al.* (1995). These are quoted in table 4.5.

The model of Nilsen *et al.* was used to determine total charge-changing cross sections for the UHCRE analysis. The calculated σ (*P*,*T*,*K*) for $_{79}$Au ions in two of the elements comprising the UHCRE apparatus is presented in fig. 4.10.

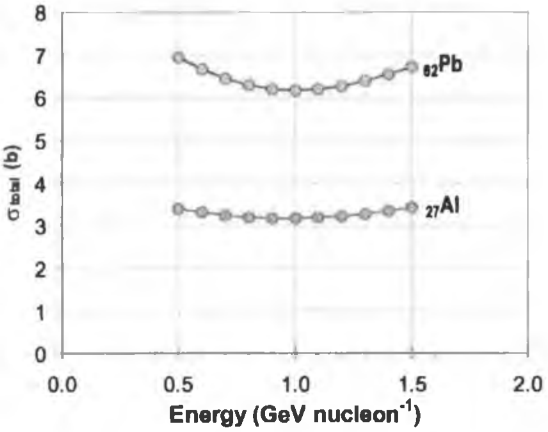

FIGURE 4.10 Calculated total charge-changing cross sections for $_{79}$Au projectiles at various energies in two of the fragmenting substances in the UHCRE (using the model of Nilsen *et al.*, 1995)

4.4.2 *Partial Nuclear Interaction Cross-sections* ($\sigma_{partial}$)

Fragmentation of cosmic rays in the detector can produce spallation products which increase the measured flux of lower charges and so distort the charge abundance spectrum. Thus, σ_{partial} is calculated for every Z and every ΔZ (where $Z + \Delta Z$ is the charge of the spallation product under consideration). These data are used to adjust the elemental abundances downwards to their pre-fragmentation levels outside the LDEF spacecraft.

The simplest model of the behaviour of the partial cross sections is that of a power law in ΔZ.* Measured nonhydrogen values of σ_{partial} (P, T, ΔZ) for $-20 \leqslant \Delta Z \leqslant -2$ fragments have been used to fit power laws of the form:

$$\sigma_{\text{partial}} = \sigma\,|\,\Delta Z\,|^{-\varepsilon}$$

While the above power law illustrates the relationship between $\sigma_{partial}$ and ΔZ, there appear to be significant deviations for targets lighter than carbon and at lower energies (< ≈ 1 A GeV).

Unlike total nuclear interaction cross sections, partial cross sections are heavily energy-dependent, $\sigma_{partial}$ generally decreasing with increasing projectile energy. For

---

* It appears that the behaviour of cross-sections in hydrogen targets is different from that in any other target yet studied. We confine our discussion to fragmentation in the non-hydrogen targets of the UHCRE apparatus. Note that the partial charge-changing cross sections from $\Delta Z = -2$ to -20 constitute 86.2% of σ_{total} in a hydrogen target (and just 28.6% in lead); Nilsen *et al.* (1995). The majority of the other reactions that contribute to σ_{total} are fission and can be ignored here as their daughter products do not alter the $Z > 70$ charge spectrum.

example, Geer *et al.* (1995) have shown that the sums of small charge-changing cross sections for heavy nuclei such as $_{79}$Au changed by nearly a factor of 2 between 1.0 and 10.0 GeV nucleon^{-1}.

However, $\sigma_{partial}$ does show a transition to energy-independence at high energies. As projectile energy increases, the extra energy creates more particles or disintegrates more of the subfragments instead of opening up new channels for the production of a given fragment or new particles. Such *limiting fragmentation* occurs at intermediate energies (i.e., a few GeV nucleon^{-1}) and more measurements are required to improve the models at these energies. Several attempts have been made to gather more fragmentation data to infer a general model for $\sigma_{partial}$ $(P, T, \Delta Z, E)$.

Cummings *et al.* (1990, 1990b) demonstrated that small negative charge changes from the incident nuclei have cross sections which are excellently described by power laws in $|\Delta Z|$ of the form: $\sigma_{\text{partial}} = \sigma_\beta\,|\,\Delta Z\,|^{-\beta}$. Heavy projectiles on hydrogen targets have cross sections which show a somewhat less regular exponential dependence on $|\Delta Z|$ of the form: $\sigma_{\text{partial}} = \sigma_\delta \exp(-|\,\Delta Z\,|/\delta)$. The fitting parameters σ_β, β, σ_δ and δ are functions of the energy and masses of the projectile and target nuclei.*

In attempting to avoid the complicated multiparametric semiempirical approach of Silberberg *et al.* (e.g., Silberberg & Tsao, 1973a; 1973b), which yields predictions in error by as much as a factor of two, Cummings *et al.* used a new approach based on factorisation. They derived a parametric fit with seven independent parameters, applicable over a wide range of projectiles, targets and energies:

$$\sigma(A_P, A_T, E, \Delta Z) = p_1\left(A_P^{1/3} + A_T^{1/3} - p_2\right)\left[1 + \frac{E}{p_4}\right]\Delta Z^{\{p_6[1+(A_P/p_7)][1+(A_T/p_8)][1+(E/p_9)]\}}$$

where $p_1 = 45.24 \pm 2.15$, $p_2 = 0.81 \pm 0.36$, $p_4 = -3.48 \pm 0.16$, $p_6 = -0.614 \pm 0.013$, $p_7 = 788.7 \pm 59.5$, $p_8 = 1173 \pm 204$ and $p_9 = -11.13 \pm 1.72$. This equation provides a fit to the measured data of $\chi^2 = 1.81$.

Waddington *et al.* (1999$^{a,\,b}$) have measured partial cross sections for $_{79}$Au projectiles on targets of hydrogen, polyethylene (CH_2), carbon, aluminium, copper, tin and lead. The projectile energies correspond to those of the UHCRE's cosmic rays (namely, between 0.92

---

* Cummings *et al.* (1990) also reported that the cross sections from fragments with $\Delta Z = -1$ were systematically larger than expected and surmised that electromagnetic dissociation (EMD) could be a contributing cause. In EMD, a relativistic nucleus passing a target nucleus at a small impact arameter (but large enough to avoid interaction) experiences an electromagnetic pulse from the Lorentz contracted field of the target nucleus, resulting in the emission of one or more neutrons.

and 4.0 GeV nucleon^{-1}). They report significant energy dependence in $\sigma_{partial}$, and fit a modified power law to their data, valid for $|\Delta Z| \leqslant 12$ and $E \leqslant 5.0$ GeV nucleon^{-1}. From their data, they further conclude that it is reasonable to assume that limiting fragmentation occurs by 4.0 GeV nucleon^{-1}.

Nilsen *et al.* (1995) use newer fragmentation data to update the successful parametric power-law model of Cummings *et al.* with one which yields slightly improved values of χ_ν^2 and leads to limiting fragmentation at high energies.

$$\sigma_{partial}(A_P, A_T, K, \Delta Z) = p_1\left(A_P^{1/3} + A_T^{1/3} - p_2\right)\left(1 + \frac{p_3}{K}\right)\Delta Z^{-p_4\left[1+\left(A_P^{1/3}/p_5\right)+\left(A_T^{1/3}/p_6\right)+\left(p_7/K\right)\right]}$$

where $p_1 = 21.2 \pm 0.5$ mb, $p_2 = 1.08 \pm 0.15$, $p_3 = (0.485 \pm 0.014)$ GeV nucleon^{-1}, $p_4 = 0.094 \pm 0.013$, $p_5 = 1.11 \pm 0.02$, $p_6 = 10.6 \pm 1.6$ and $p_7 = (0.85 \pm 0.03)$ GeV nucleon^{-1}.

It is this equation that is used to calculate partial nuclear interaction cross sections for the UHCRE analysis. It was decided to confine the examination of daughter products to the range $2 \leqslant |\Delta Z| \leqslant 20$ because: a) these are better known experimentally, b) Au signals from fragments of $|\Delta Z| \leqslant 20$ cannot be confused with fission fragments from higher-Z ions and c) the $\Delta Z = -1$ fragments are systematically larger than the trend from smaller charge changes would imply and appear to include an additional component, probably attributable to electromagnetic dissociation. The calculated $\sigma_{partial}$ (P,T,K) for $_{79}$Au ions in two of the elements comprising the UHCRE apparatus is presented in fig. 4.11.

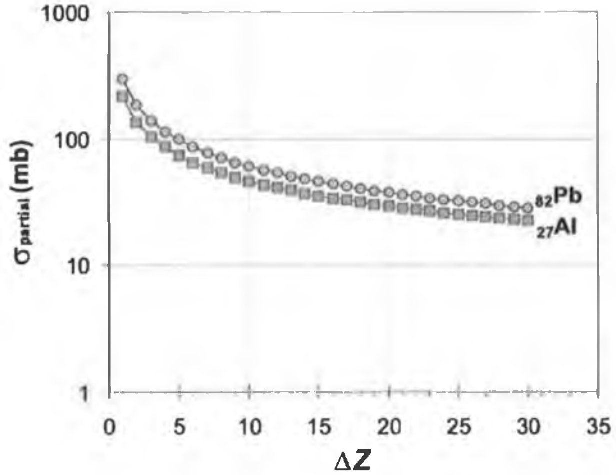

FIGURE 4.11 Calculated partial charge-changing cross sections for 1.5 GeV nucleon^{-1} $_{79}$Au projectiles undergoing various ΔZ interactions in two of the fragmenting substances in the UHCRE (using the model of Nilsen *et al.*, 1995).

4.4.3 *Correcting the UHCRE sample for fragmentation*

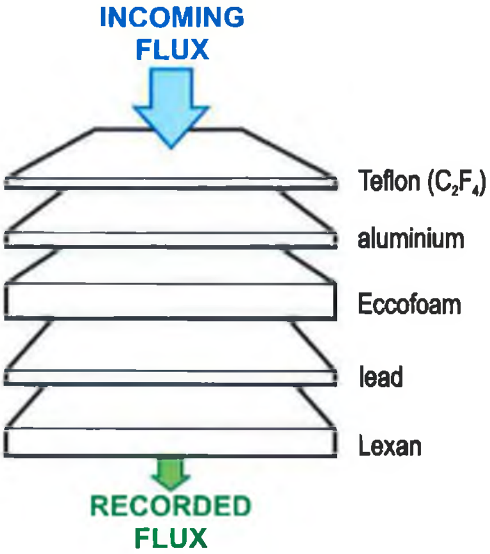

FIGURE 4.12 Potential sites for fragmentation in the UHCRE apparatus.

There are five layers of the UHCRE apparatus which can cause fragmentation of incoming cosmic rays (fig. 4.12; see also fig. 2.2). The first is a layer of silver-coated *Teflon* (C_2F_4) that covers each experiment tray.* In addition, an *aluminium* cylinder surrounds the *eccofoam* mount for the detector stacks. The stacks themselves consist of *Lexan* polycarbonate plates interleaved with a varying number of *lead* plates.

Table 4.6 details the effective atomic weights, vertical thicknesses and pathlengths of a GCR through each of these layers. The total nuclear-interaction cross sections for a $_{79}$Au ion projectile are calculated. The projectile's kinetic energy was assumed to be 1.5 GeV nucleon^{-1}, close to the modal energies of cosmic rays in the UHCRE sample (a few GeV nucleon^{-1}). The nuclear radii parameters from table 4.5 were used for the $_{79}$Au projectile and the $_{27}$Al and $_{82}$Pb targets.

The survival fraction of ions in a given incoming flux was then inferred using the equation:

$$survival\ fraction = 1 - \left(\frac{N_A x \sigma_{total}}{A_T \times 10^{-3}\,kg} \right)$$

where N_A is Avogadro's number, x is the path length traversed in (kg m^{-2}) and A_T is the atomic mass of the target.

Note that the most probable site for fragmentation is within the polycarbonate of the detectors themselves. This confirms the relative effectiveness of lead as a low-fragmentation velocity degrader.

---

* As the silver coating was just 1000 Å thick, its effect is ignored here.

Table 4.6 Calculated total cross section (σ_{total}) for $_{79}$Au ions in the constituent layers of the UHCRE detector apparatus.*

Target	A_T	thickness (cm)	thickness (g cm^{-2})	pathlength (g cm^{-2})†	pathlength (kg m^{-2})	σ_{total} ‡ (b)	survival fraction
Teflon	60	0.0127	0.0272	0.034	0.34	13.3	**1.00**
Aluminium	27	0.24	0.65	0.8	8.0	3.4	**0.94**
Eccofoam	258	11.7	0.374	0.463	4.63	72.7	**0.92**
Lead	207	0.28	3.18§	3.92	39.2	6.7	**0.92**
Lexan	254	1.75	2.10	2.60	26.0	62.1	**0.62**

Further calculations demonstrated that the differences between cross section values using the parameterisations of Nilsen *et al.* (1995) and Westphal *et al.* (1979) were negligible. The calculated survival fractions in Lexan (using cross sections from Nilsen *et al.*) also concur with a previously-written simulation based on the cross-section values of Silberberg & Tsao.

In every layer of the UHCRE apparatus, and for each Z in the range $70 \leqslant Z \leqslant 98$, the following procedure was executed:

1) The total charge-changing cross section (σ_{total}) was calculated and used to determine the survival fraction of Z in the cosmic ray flux. The measured abundance of Z was then increased to the inferred original value before fragmentation
2) Partial charge-changing cross sections ($\sigma_{partial}$) for $\Delta Z = -1$ to -20 were calculated. The contributions of spallation products from Z to lower-charge abundances were then removed.

---

* The total cross sections in Table 4.6 were calculated for the relatively well-examined ^{197}Au ion and then scaled to other values of A by $(A/A_{Au})^{2/3}$. Scaling by Z was avoided as Z and A are related linearly only at charges below $Z = 82$ or so. Though this approach is a legitimate one for total cross sections (Waddington *et al.*, 1999^b), further measurements are needed to ascertain if such scaling is entirely applicable to the partial cross sections.

† These calculations use the calculated average dip angle (54°) for incident cosmic rays.

‡ The cross-sections for aluminium and lead are calculated from the equation above while those for non-elemental materials (i.e., teflon, eccofoam and lexan, for which values of R_n are unavailable) per molecule are obtained from Bosch (1995).

§ This figure is based on the average number of lead plates traversed. Including unmeasured events, 636 were recorded in stacks with 6 lead plates, 15 in stacks with 4 lead plates and 37 in stacks with zero lead plates. Thus GCRs in the Pt-Pb sample passed through an average of 5.6 lead plates.

The results using the Nilsen *et al.* (1995) models for σ_{total} and $\sigma_{partial}$ are shown in figs. 4.13 and 4.14. Note that the overall increase in abundances at the top of the atmosphere demonstrates the importance of σ_{total} cross sections relative to $\sigma_{partial}$. Fragmentation effects vary the relative abundances of $_{79}$Au and $_{92}$U (for example) by ~14%. Most of this is due to the effects of the total cross section, as the partial cross section generally contributes less than a 2% effect.

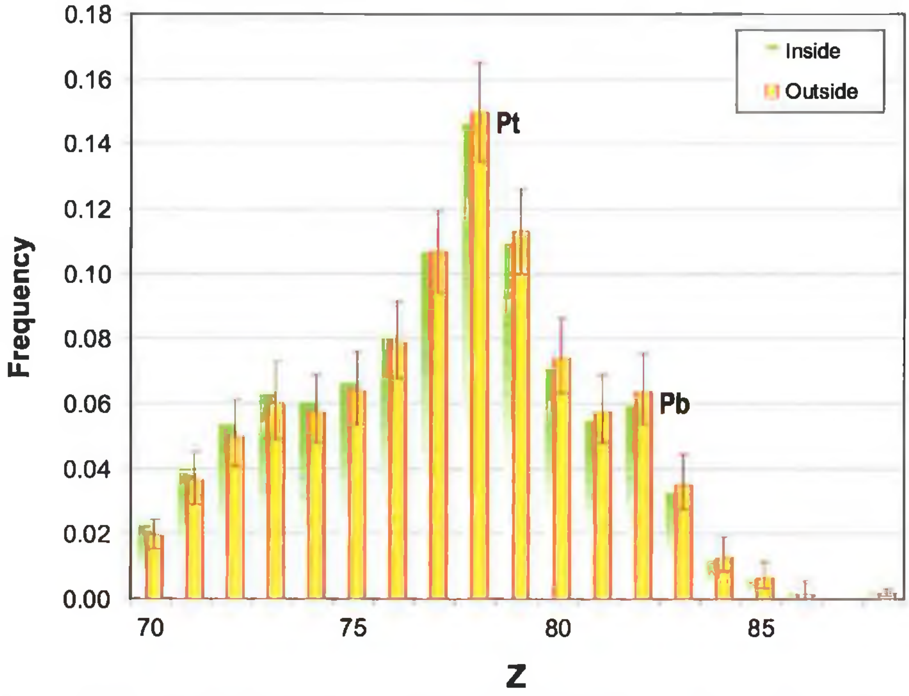

FIGURE 4.13 Charge distribution of Pt-Pb events inside and outside the LDEF spacecraft. Error bars correspond to 1σ (Gehrels, 1986).

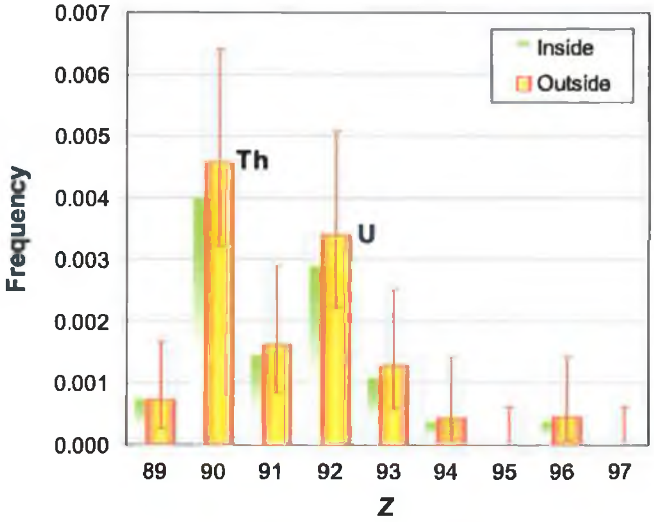

FIGURE 4.14 Charge distribution of actinide "events" inside and outside the LDEF spacecraft. Error bars correspond to 1σ (Gehrels, 1986).

4.5 Corrected Charge Spectrum

A summary of elemental charge abundances from this chapter are presented in tables 4.7 and 4.8.

Table 4.7 Subactinide ($70 \leqslant Z \leqslant 87$) abundances after improvements[*]

	Original		**After Quality Control**		**Fragmentation Corrected**
Charge	No. of events	Frequency	No. of events	Frequency	Frequency
70	23	0.034	15.6	0.023	0.019
71	24	0.036	27.2	0.040	0.036
72	28	0.041	36.1	0.054	0.050
73	30	0.044	42.7	0.063	0.060
74	36	0.053	40.8	0.060	0.057
75	38	0.056	44.9	0.067	0.064
76	50	0.074	54.2	0.080	0.079
77	70	0.104	72.0	0.107	0.107
78	**96**	**0.142**	**98.7**	**0.146**	**0.150**
79	74	0.110	74.0	0.110	0.113
80	48	0.071	48.0	0.071	0.074
81	37	0.055	37.0	0.055	0.058
82	**40**	**0.059**	**40.0**	**0.059**	**0.063**
83	22	0.033	22.0	0.033	0.035
84	8	0.012	8.0	0.012	0.013
85	4	0.006	4.0	0.006	0.006
86	1	0.001	1.0	0.001	0.002
87	0	0.000	0.0	0.000	0.000
Total	**629**	**0.932**	**666**	**0.987**	**0.986**

---

[*] Frequencies in the *Original* and the *After Quality Control* columns are relative to the estimated total number of $Z \geqslant 70$ events in the UHCRE's 162 accessible detector stacks (adjusted for the geometrical effects described in section 4.3.2); i.e., 2760 events. In the *Fragmentation Corrected* column, the figure has been adjusted for fragmenation (yielding a figure of 3022 events).

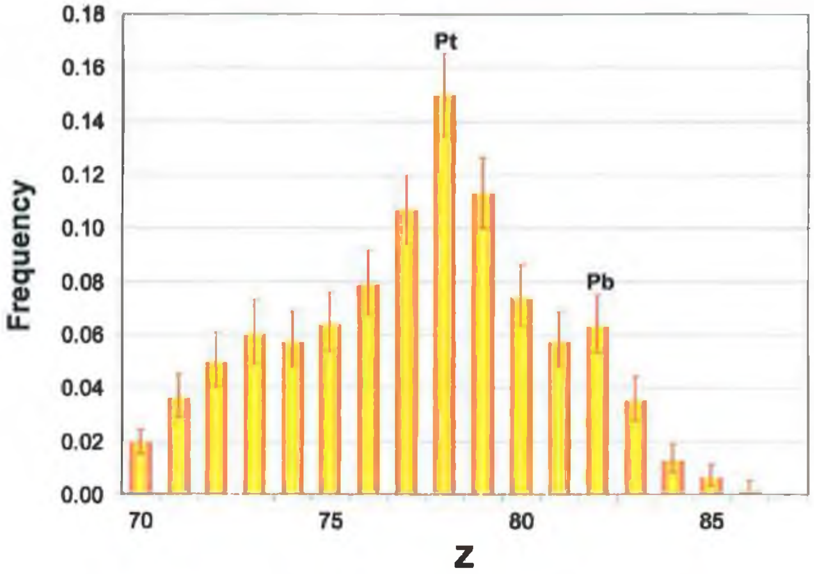

FIGURE 4.15 Frequency charge distribution of subactinide cosmic rays at the top of the atmosphere. Statistical error bars correspond to 1σ (Gehrels, 1986).

Table 4.8 Actinide ($88 \leqslant Z \leqslant 103$) abundances after improvements[*]

	Original		**Etching Variation Removed**		**Fragmentation Corrected**
Charge	No. of events	Frequency	No. of events	Frequency[*]	Frequency[*]
88	4	0.0014	5	0.0018	0.0020
89	6	0.0022	2	0.0007	0.0007
90	**4**	**0.0014**	**11**	**0.0040**	**0.0046**
91	7	0.0025	4	0.0014	0.0016
92	**8**	**0.0029**	**8**	**0.0029**	**0.0034**
93	1	0.0004	3	0.0011	0.0013
94	2	0.0007	1	0.0004	0.0004
95	0	0.0000	0	0.0000	0.0000
96	0	0.0000	1	0.0004	0.0004
97	1	0.0004	0	0.0000	0.0000
Total	33	0.0120	35	0.0127	0.0144

---

[*] Frequencies in the *Original* and *Etching Variation Removed* columns are relative to the estimated total number of $Z \geqslant 70$ events in the UHCRE's 162 accessible detector stacks (i.e., 2760 events). In the *Fragmentation Corrected* column, the figure has been adjusted for fragmenation (yielding 3022 events).

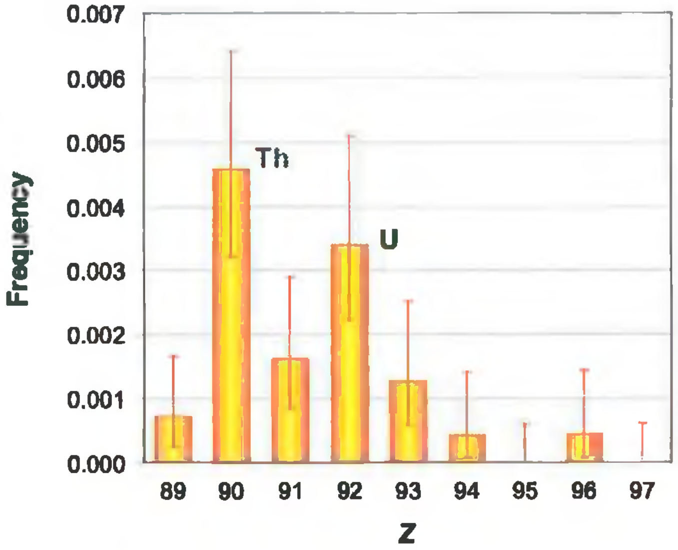

FIGURE 4.16 Frequency charge distribution of actinide cosmic rays at the top of the atmosphere. Error bars correspond to 1σ (Gehrels, 1986).

Note that when comparing abundance ratios of actinide and subactinide elements, their *frequencies* must be used, as the numbers of events derive from different sample sizes. These data are plotted in figs. 4.15 and 4.16, wherein elements important to theories of galactic cosmic-ray origin are indicated. Chapter 5 addresses the impact of these data on such theories.

4.6 Systematic Errors

In the results of previous sections, only statistical errors have been included on elemental abundances. Including systematic errors involved the use of a Monte-Carlo simulation which operated in the following way:

1. Each measured event was assigned a random error in the form of a Gaussian distribution of standard deviation equal to the systematic charge-assignment error of the UHCRE. This error (i.e., +1.4e / -1.5e in the subactinide region and ±1.3e for the actinides) was derived in Section 3.2.5.

2. Step 1 resulted in a synthetic charge-abundance histogram, with systematic errors included. 1,000 such synthetic spectra were generated.

3. For each Z bin of $70 \leqslant Z \leqslant 87$ the mean abundance of the 1,000 synthetic spectra was derived. The standard deviation of this mean abundance was also inferred and used as the systematic error on the abundance of that charge.

4. These systematic errors were combined with statistical errors (derived from Gehrels, 1986) to determine the total charge-abundance error in each Z bin.

On applying this technique to Z bins with a range of 1e, the Pt peak remained, but the Pb peak was eliminated. This smothering of structure inherent in the data indicates that our charge-assignment error estimate is pessimistic, meaning that it was not possible to calculate accurate systematic errors on the abundances of individual elements. However, systematic errors on the abundance ratios of charge *groups* were calculated and are presented in table 4.9.

Table 4.9 Statistical and Monte-Carlo calculated systematic errors for various abundance ratios in the UHCRE data[*]

Ratio	Systematic Error (%)	Statistical Error (%)	Total (%)
"Pt"/"Pb"	± 9.1[†]	± 11.2	± 14.4
Actinides / "Pt"	± 4.5	+ 20.5 - 17.5	+ 21.0 - 18.1
Actinides / subacitinides	± 4.2	+ 20.4 - 17.4	+ 20.8 - 17.9

Summary

We have already seen in Chapter 3 that the derived errors on UHCRE charge-assignment are compatible both with the results from Monte-Carlo simulations and with those from previous DIAS research. The addition of systematic errors (Section 4.6) reveals that the total charge-assignment error (especially on actinide abudances) is dominated by statistical error (cf. Table 4.9 and footnotes in Table 5.2). Thus, detector resolution (i.e., "systematic" error) is *not yet* the primary limiting factor in measurements of the actinide abundances. This is an important consideration for any future ultra-heavy cosmic-ray studies.

The calculated survival fractions in Lexan shown in Table 4.6 (using cross sections from Nilsen *et al.*, 1995) agreed with those from a previously-written simulation that used the cross-sections of Silberberg & Tsao. Other studies showed that cross-section calculations from the parameterisations of Nilsen *et al.* differed negligibly from those of Westfall *et al.* (1979).

The errors derived in this chapter determine the limits of our knowledge of important abundance ratios in the cosmic rays. The UHCRE's estimates of these key ratios are presented in Chapter 5, where their implications are also discussed.

---

[*] "Pt" ≡ ($74 \leqslant Z \leqslant 80$), "Pb" ≡ ($81 \leqslant Z \leqslant 83$), "Subactinides" ≡ ($74 \leqslant Z \leqslant 87$) and "Actinides" ≡ ($Z \geqslant 88$).

[†] Note that the systematic error on this abundance ratio is *not* merely a combination of the separate errors on "Pt" and "Pb". Since these charge ranges abut one another, the "Pt"/"Pb" ratio is highly senstiive to Z-assignment errors.

5. Conclusions

In this final chapter, the UHCRE data (Section 5.1) are compared with other measurements (Section 5.2). Further results are obtained with Monte-Carlo simulations (Section 5.3), the possibility of a transuranic component in the GCR flux is investigated (Section 5.4) and the UHCRE's impact on determining the origin of the cosmic rays is discussed (Section 5.5).

5.1 Initial Observations

The elemental abundances in the galactic cosmic rays as measured at the top of the earth's atmosphere by the UHCRE are presented in table 5.1 and are plotted in figure 5.1. These frequencies are normalized to the UHCRE's $Z \geqslant 70$ sample so that $\sum_{Z\geq 70} f_Z = 1$.

Table 5.1 Elemental abundances from the UHCRE, relative to the entire $Z \geqslant 70$ sample

		Before Fragmentation Adjustment			**After Fragmentation Adjustment**		
Element	**Charge**	**Frequency**	**1 σ statistical errors**[*]		**Frequency**	**1 σ statistical errors**[*]	
			+	-		+	-
Yb	70	0.023	0.0059	0.0048	0.019	0.0049	0.0040
Lu	71	0.040	0.0100	0.0082	0.036	0.0090	0.0073
Hf	72	0.054	0.0121	0.0101	0.050	0.0113	0.0093
Ta	73	0.063	0.0138	0.0115	0.060	0.0131	0.0109
W	74	0.060	0.0119	0.0100	0.057	0.0113	0.0095
Re	75	0.067	0.0126	0.0108	0.064	0.0121	0.0103
Os	76	0.080	0.0130	0.0113	0.079	0.0128	0.0111
Ir	77	0.107	0.0128	0.0128	0.107	0.0128	0.0128
Pt	78	0.146	0.0149	0.0149	0.150	0.0153	0.0153
Au	79	0.110	0.0127	0.0127	0.113	0.0132	0.0132
Hg	80	0.071	0.0118	0.0102	0.074	0.0123	0.0106
Tl	81	0.055	0.0106	0.0090	0.058	0.0111	0.0094
Pb	82	0.059	0.0109	0.0093	0.063	0.0117	0.0100
Bi	83	0.033	0.0085	0.0069	0.035	0.0092	0.0074
Po	84	0.012	0.0059	0.0041	0.013	0.0063	0.0044
At	85	0.006	0.0047	0.0028	0.006	0.0050	0.0030
Rn	86	0.001	0.0034	0.0012	0.002	0.0037	0.0013
Fr	87	0.0000	0.00067	-	0.0000	0.00067	-
Ra	88	0.0018	0.00123	0.00078	0.0020	0.00134	0.00086
Ac	89	0.0007	0.00096	0.00047	0.0007	0.00095	0.00046
Th	90	0.0040	0.00160	0.00118	0.0046	0.00184	0.00136
Pa	91	0.0014	0.00115	0.00069	0.0016	0.00128	0.00077
U	92	0.0029	0.00143	0.00100	0.0034	0.00168	0.00118
Np	93	0.0011	0.00106	0.00059	0.0013	0.00124	0.00069
Pu	94	0.0004	0.00083	0.00030	0.0004	0.00099	0.00035
Am	95	0.0000	0.00067	-	0.0000	0.00067	-
Cm	96	0.0004	0.00083	0.00030	0.0004	0.00100	0.00036
Bk	97	0.0000	0.00067	-	0.0000	0.00067	-
Total		1.0			1.0		

---

[*] All error estimates from Gehrels (1986), except $77 \leqslant Z \leqslant 79$ abundances, which use $\sqrt{n}$ errors bars.

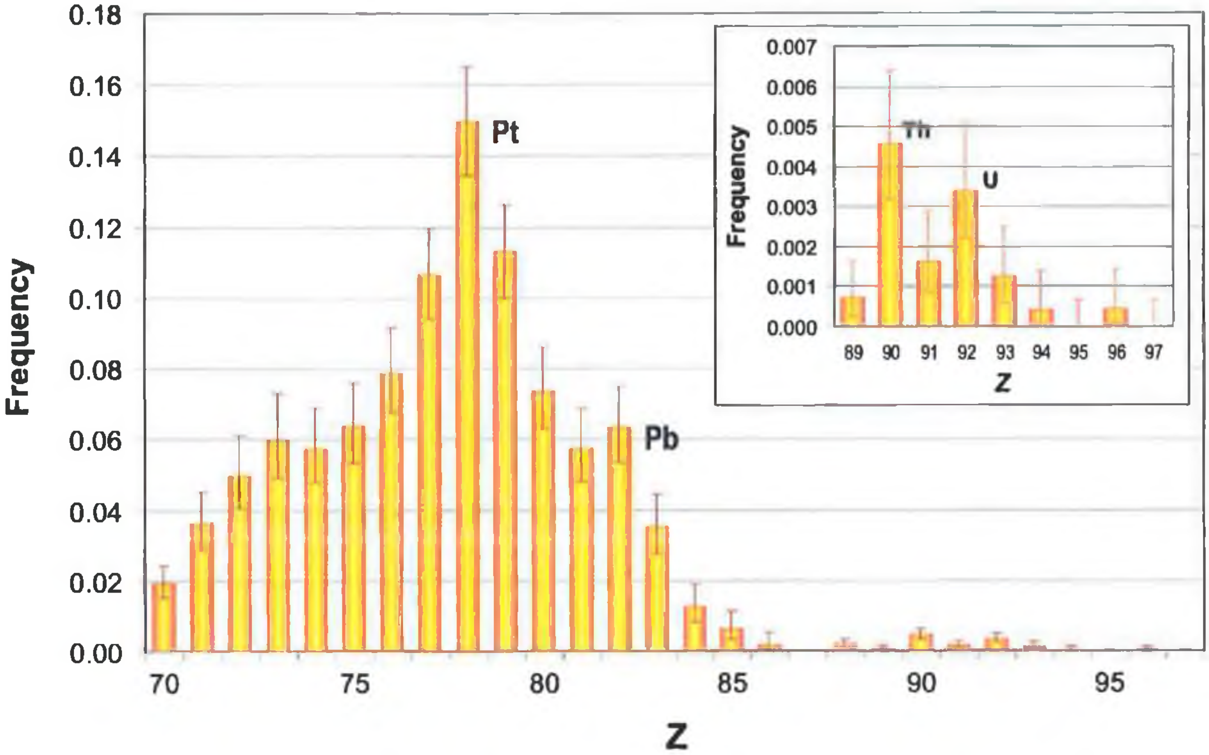

FIGURE 5.1 The UHCRE charge spectrum, normalized to the total $Z \geqslant 70$ sample. 1σ statistical error bars are included (Gehrels, 1986).

The abundances and charge-assignment error of both the actinides and subactinides were used to obtain semi-empirical Gaussian curves for the $_{82}$Pb and $_{90}$Th peaks. Figure 5.2 demonstrates that the actinide and subactinide abundances overlap (at a low value) between $86 \leqslant Z \leqslant 87$. This result both justifies our assumption of an actinide gap and provides increased confidence in our error estimates.

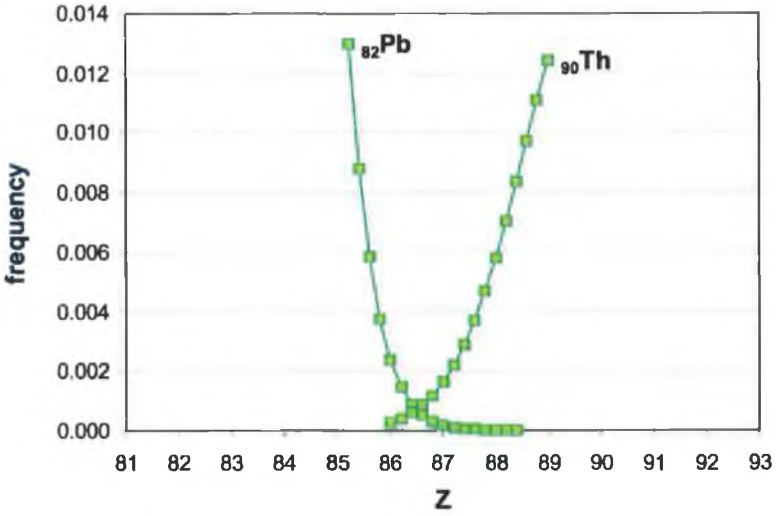

FIGURE 5.2 Extrapolated Charge Spread of $_{82}$Pb and $_{90}$Th peaks using the Gaussian errors for actinides and subactinides presented in Table 3.6.

Furthermore, assuming the measured Pb peak is a Gaussian distribution, a charge-assignment error of 1.2 e was inferred from the data. This is entirely consistent with the (conservative) estimate from Chapter 3 (ΔZ = +1.4 e / -1.5 e) *and* with that obtained by

Bosch (1995) from UHCRE data ($\Delta Z = \pm 1.4$ e). These concurrences lend further support to our error estimates.

Abundance ratios from a variety of sources, including this work, are compiled in table 5.2. Note that absolute values from the different sources in this table are not normalized and so cannot be directly compared to one other. However, the *ratios* of the charge groups can be compared and the most significant of these ratios are presented in the last three rows of the table.[*]

---

[*] Note that the values in this table do not include the effects of the Earth's magnetic field. Geomagnetic transmission effects as calculated from the CREME96 website (https://creme96.nrl.navy.mil/) on the quoted ratios were examined. High rigidity (i.e., higher A/Z) nuclei have a greater chance of being detected than lower-rigidity species. Most of the UHCRs detected by the UHCRE are expected to have energies between 2 and 4 GeV/nucleon – see figure 3.9(a) – and for this energy range, the increase in the $_{92}$U/$_{90}$Th and "Pb"/"Pt" ratios due to geomagnetic cutoff where estimated to be very small (~1% and ~5% respectively). The increase in the actinide/"Pt" ratio, however, was found to be ~11%, which may explain the anomalously high value obtained by both the UHCRE and other space-based observations. Interpretation of this last ratio, however, is further complicated by large uncertainties in its propagation factor and so at the moment the insight it provides is limited.

Table 5.2 Charge-group abundances from various meteoritic and cosmic-ray sources

Group[*]	**Charge**	**Anders & Ebihara**[†] **(1982)**		**Anders & Grevesse**[†] **(1989)**		**Lodders**[†] **(2003)**		**This work**[‡]		**Binns *et al.* (1989)**	**Westphal *et al.* (1998)**
HS	70	0.243	0.48	0.2479	0.46	0.2484	0.48	0.019	0.17 ± 0.02	1.9	-
	71	0.0369		0.0367		0.03572		0.036			
	72	0.176		0.151		0.1699		0.050			
	73	0.0226		0.0207		0.02099		0.060			
“Pt”	74	0.137	3.64	0.133	3.39	0.1277	3.46	0.057	0.64 ± 0.03	5.4	135
	75	0.0507		0.0517		0.05254		0.064			
	76	0.717		0.675		0.6738		0.079			
	77	0.6600		0.661		0.6448		0.107			
	78	1.37		1.34		1.357		0.150			
	79	0.186		0.187		0.1955		0.113			
	80	0.52		0.34		0.4128		0.074			
“Pb”	81	0.184	3.48	0.184	3.48	0.1845	3.58	0.058	0.16 ± 0.02	1.6	36
	82	3.15		3.15		3.258		0.063			
	83	0.144		0.144		0.1388		0.035			
actinides	90	0.0335	0.04	0.0335	0.04	0.03512	0.04	0.014	$^{+0.003}_{-0.002}$	0.13	6
	92	0.0090		0.0090		0.009306					
“Pb” / “Pt"		0.9553		1.0267		1.0338 ± 0.1166		0.24 ± 0.03		0.30	0.27
actinides / “Pt"		0.0117		0.0125		0.0128 ± 0.0014		0.022 $^{+0.005}_{-0.004}$		0.0241	0.0444
actinides / subactinides		0.0060		0.0062		0.0063 ± 0.0006		0.018 $^{+0.004}_{-0.003}$		0.0186	0.035

---

[*] Here, *HS* (heavy secondaries) ≡ (70 ⩽ Z ⩽ 73), *“Pt”* ≡ (74 ⩽ Z ⩽ 80), *“Pb”* ≡ (81 ⩽ Z ⩽ 83), *subactinides* ≡ (74 ⩽ Z ⩽ 87) and *actinides* are Z ⩾ 88.

[†] Normalized to the abundance of Si (= 10^6).

[‡] These data are corrected for fragmentation and normalized to the UHCRE's Z ⩾ 70 sample. 1σ errors are presented: HS ± 11.4% [± 5.9% (systematic), ± 9.8% (statistical)]; “Pt” ± 5.3% [± 2.0% (systematic), ± 4.9% (statistical)]; “Pb” ± 12.3% [± 7.1% (systematic), ± 10.1% (statistical)]; actinides $^{+20.3\%}_{-17.3\%}$ [± 4.0% (systematic), $^{+19.9\%}_{-16.8\%}$ (statistical)].

5.2 Abundance Ratios

5.2.1 ${}_{82}Pb/{}_{78}Pt$

As discussed in Chapter 1, the ${}_{82}$Pb / ${}_{78}$Pt abundance ratio is a key indicator of whether nuclei are fractionated by FIP or volatility during cosmic-ray acceleration. Here, the UHCRE's results are compared with those reported from other experiments and those derived from meteoritic and photospheric analyses. It is convenient to compare the ratios of charge groups, the definition commonly used in the literature being "Pt" ≡ $(74 \leqslant Z \leqslant 80)$ and "Pb" ≡ $(81 \leqslant Z \leqslant 83)$. This definition is used in figure 5.3 which compares the UHCRE results with data from meteoritic studies and from other experiments.

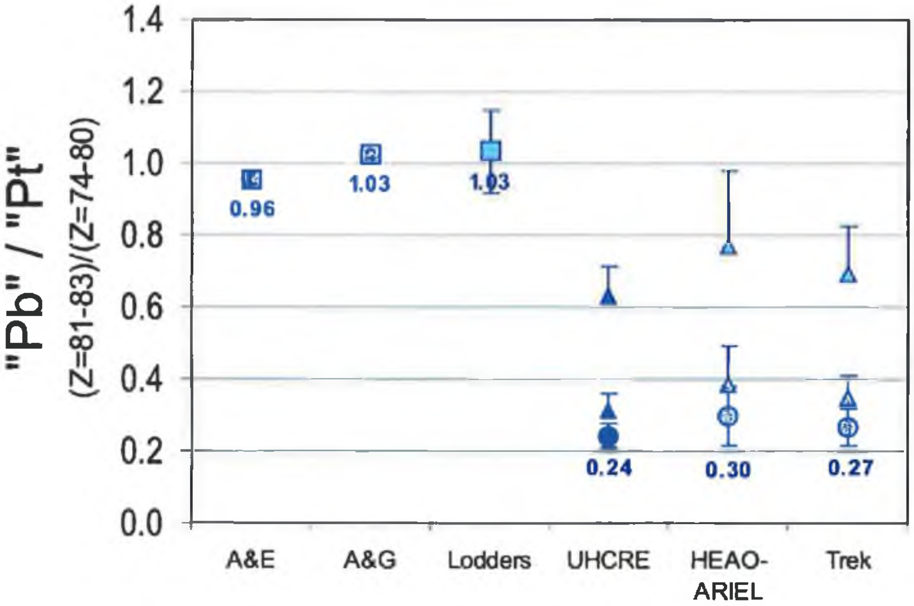

FIGURE 5.3 "Pb" / "Pt" abundance ratios for various souces. 1σ systematic and statistical error bars are shown on all GCR measurements and the meteoritic value recommended by Lodders (2003). An exception is the *Trek* datum, which includes only statistical errors (systematic errors are small in this case). The triangular points are upper limits at the source, assuming maximum and minimum propagation changes to the "Pb" / "Pt" ratio (i.e., factors of ×1.3 and ×2.6, respectively).[*]

CI-chondrite meteoritic data were obtained from the following sources: A&E (Anders & Ebihara, 1982); A&G (Anders & Grevesse, 1989) and Lodders (Lodders, 2003). Cosmic-ray data were obtained from combined HEAO-3 and ARIEL-6 spacecraft results (Binns *et al.*, 1989) and the *Trek* experiment (Westphal *et al.*, 1998).

The maximum likely values at the source (taking propagation factors from Meyer, Drury & Ellison, 1997) are shown. The UHCRE results indicate that at the 1σ level, the "Pb"/"Pt" ratio in the cosmic rays at Earth is at most just 30% of that found in CI-chondrite source material.

---

[*] Clinton & Waddington, 1993; Waddington, 1996, 1997; Meyer, Drury & Ellison, 1997.

By assuming a commonly accepted propagation value (i.e., ×1.65 from Binns *et al.*, 1989) a comparision between the "Pb"/"Pt" ratio in the GCRs and that found in CI-chondrite material can be made. With this assumption, the UHCRE results show that at the 1σ level, the "Pb"/"Pt" ratio in the cosmic rays at the Earth is *at most* just 50% of that found in CI-chondrite source material. Even using the most extreme propagation factor (×2.6) the "Pb"/"Pt" ratio in the cosmic-ray source material is still *at most* just 79% of the minimum level found in CI-chondrite material.

Clearly, lead is depleted in the GCR source material beyond what might be expected due to propagation. Interpreting this value as a low s-process abundance is problematic, given the lack of any such effect in the first and second s-nuclei and r-nuclei peaks. Depending on propagation conditions the FIP model predicts a GCR source enhancement of between ~1.3 and ~2.6 of solar. Since FIP-biased source material would have a "Pb"/"Pt" ratio slightly higher than solar (~1.6), the UHCRE value is actually $\sim 4.0^{+1.1}_{-1.5}$ times *lower* than that predicted by the FIP model.

5.2.2 *Actinides/"Pt"*

In Figure 5.4, the ratio of actinide (Z ⩾ 88) to Pt-group (74 ⩽ *Z* ⩽ 80) abundances in the UHCRE findings are compared to those from the same sources referenced in Section 5.2.1.

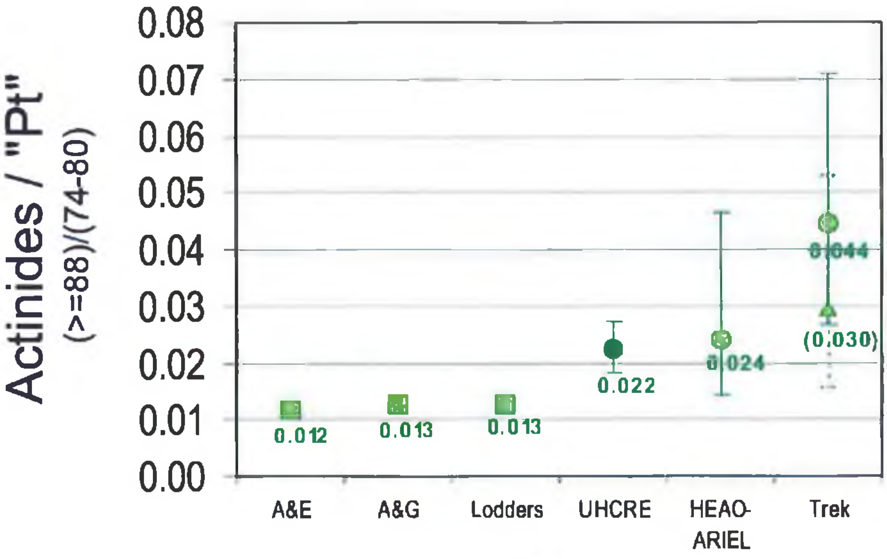

FIGURE 5.4 Actinide / "Pt" [i.e., (Z ⩾ 88) / (74 ⩽ *Z* ⩽ 80)] abundance ratios for various souces. 1σ systematic and statistical error bars are shown on experimental data (errors on the value recommended by Lodders are negligible), except for the *Trek* datum, which includes only statistical errors (systematic errors are small in this case). The triangular point and dotted error bars denote the TREK value, assuming its two unassigned actinides are spurious. Note that the UHCRE datum is "unpropagated" and represents the value at the Earth.

5.2.3 *Actinides / Subactinides*

In Figure 5.5, the UHCRE results are compared to those from the same sources described in Section 5.2.1.

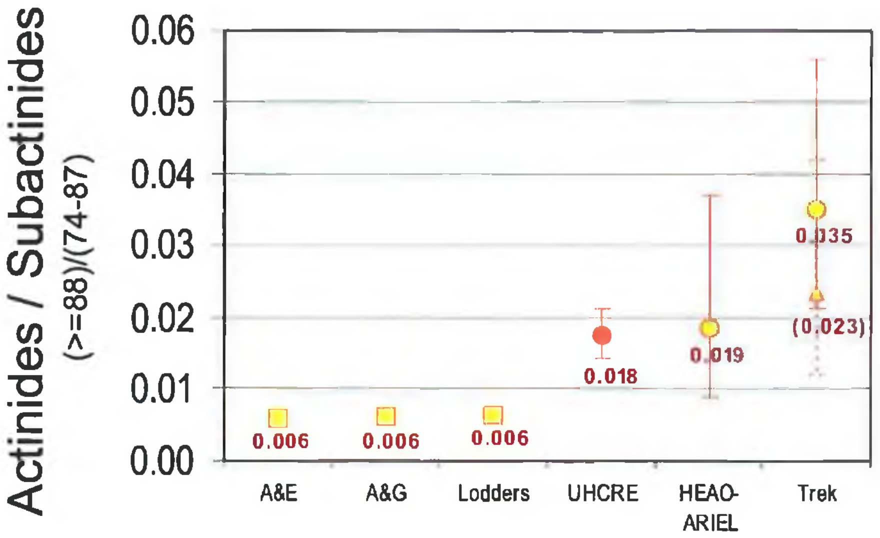

FIGURE 5.5 Actinide / subacitinide [i.e., $(Z \geqslant 88) / (74 \leqslant Z \leqslant 87)$] abundance ratios for various souces. 1σ systematic and statistical error bars are shown on experimental data (errors on the value recommended by Lodders are negligible), except for the *Trek* datum, which includes only statistical errors (systematic errors are small in this case). The triangular point and dotted error bars denote the TREK value, assuming its two unassigned actinides are spurious. Note that the UHCRE datum is "unpropagated" and represents the value at the Earth.

5.2.4 *Other Comparisons*

Lingenfelter *et al.* (2003) have used calculated r-process yields from core-collapse supernovae[*] to determine actinide abundances averaged over various time intervals. They then predicted actinide abundances in the present interstellar medium using a standard Galactic chemical evolution model (e.g., Fowler, 1972; Thielemann, Metzinger & Klapdor, 1983). They assert that since the bulk of core-collapse supernovae occur in the supernova-active cores of superbubbles, the material within these cores should comprise the bulk of the GCR source material. They then calculate U/Th and other actinide abundances expected inside a superbubble core (the actinide/"Pt" ratio does not appear to vary significantly with superbubble age). Finally, they derive expected cosmic-ray actinide ratios for a mix of acceleration sites and SN types.

---

[*] Developed by Kratz *et al.* (1993) and Pfeiffer *et al.* (1997).

Figure 5.6 compares the actinide ($Z \geqslant 88$) / "Pt" ($75 \leqslant Z \leqslant 79$) abundance ratios of Lingenfelter *et al.* to those from HEAO/ARIEL[*], (Binns *et al.*, 1989) Trek (Westphal *et al.*, 1998) and the UHCRE. Here, "Ejecta (50 Myr)" denotes the composition of SN-ejecta after 50 Myr of radioactive decay, "Superbubble" is the abundance ratio in a 50 Myr accumulation of SNe ejecta (such as that inside a SB) and "Cosmic Rays" is the expected galactic cosmic-ray composition.

Note that the UHCRE value is fully consistent with the composition inside the core of a superbubble and that estimated for GCRs. A major caveat here (and in Figures 5.4 and 5.5) is that the UHCRE value is "unpropagated". Little is known about the effect of propagation on the actinide abundances as their fragmentation cross sections are poorly-constrained. Qualitatively, however, the UHCRE value can reasonably be expected to represent a lower limit on the actinide/"Pt" ratio.

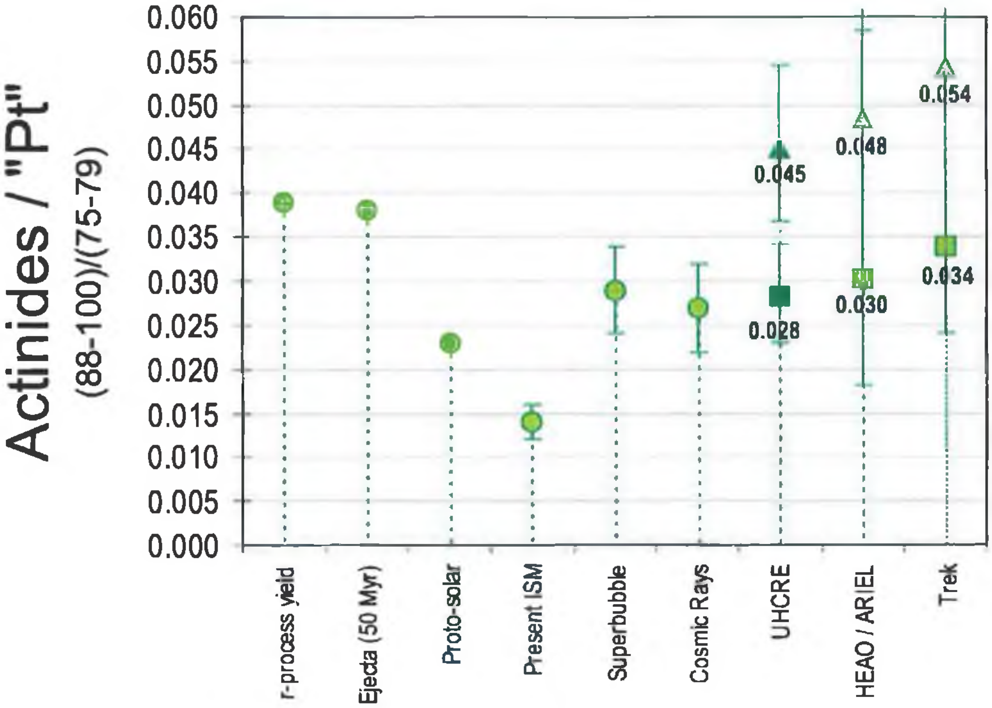

FIGURE 5.6 Actinide / "Pt" [i.e., ($Z \geqslant 88$) / ($75 \leqslant Z \leqslant 79$)] abundance ratios for various souces. Where available, 1σ systematic and statistical error bars are shown. The triangular points are UHCRE, HEAO/ARIEL and *Trek* data at the source, assuming propagation changes the actinide / "Pt" ratio by a factor of ×1.6[†]).

Note that the GCR value from the UHCRE is similar to earlier results, though more tightly constrained. The value is at least as rich in actinides as that predicted in the interior of superbubbles.

---

[*] Note that due to the slightly different definition of the Pt-group, "Pt" ≡ ($75 \leqslant Z \leqslant 79$), the HEAO and ARIEL results of Binns *et al.* (1989) are estimated by assuming the same relative distribution of charges as in the UHCRE measurements and scaling the published HEAO and ARIEL $74 \leqslant Z \leqslant 80$ abdundance and error bars appropriately.

[†] Lingenfelter *et al.*, 2003 (also, c.f. Westphal *et al.*, 1998).

5.3 A Monte-Carlo estimate of the cosmic-ray $_{90}$Th / $_{92}$U ratio

5.3.1 *The Algorithm*

As discussed in Section 1.4, changes in the relative abundances of $_{90}$Th, $_{92}$U and the transuranics some time after the r-process event that produced them are well-modelled. Thus, their relative abundances can be used as efficient cosmic ray clocks to infer the time elapsed between the r-process event and acceleration of the nuclei. The statistical error on the UHCRE abundances of these elements is too large to directly calculate the $_{90}$Th / $_{92}$U ratio. However, a Monte-Carlo Simulation was created to obtain a best estimate of their relative abundances. Fig. 5.7 illustrates the procedure.

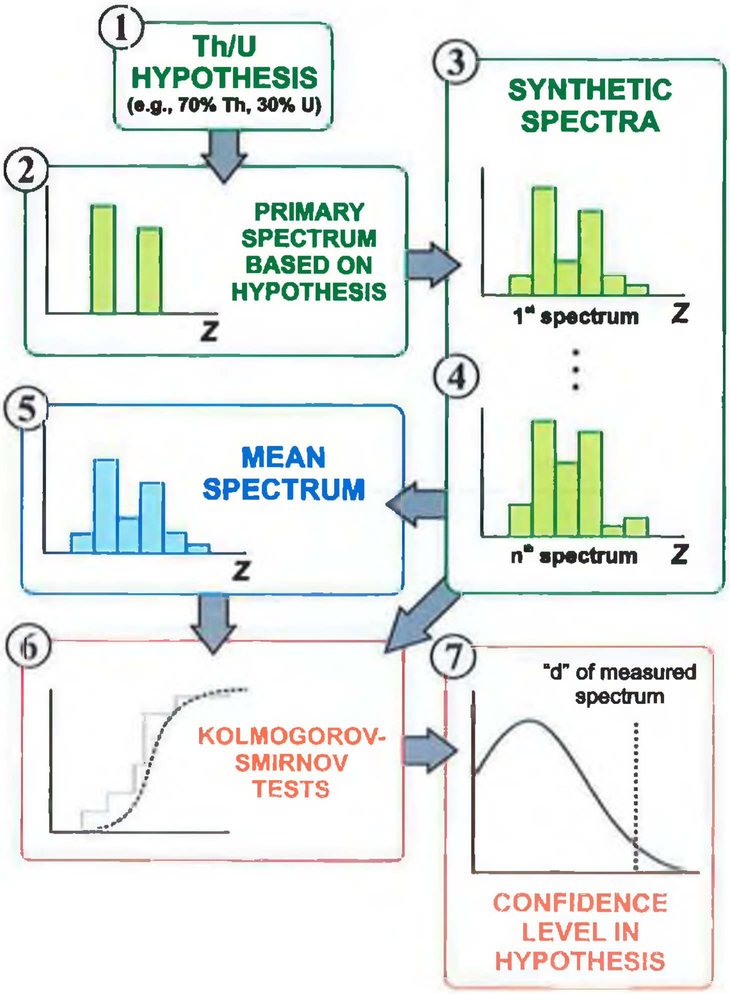

FIGURE 5.7 A Monte-Carlo procedure to estimate the Th/U ratio in the GCRs.

1. Assuming the actinide ($Z \geqslant 88$) spectrum consists only of $_{90}$Th, $_{92}$U and $_{94}$Pu primary nuclei, a hypothetical composition is chosen (e.g., 70% Th, 28% U and 2% Pu).

2. Using this hypothesis, a Monte-Carlo derived primary spectrum is created, with a sample size equal to that of the measured UHCRE sample (i.e., 35 events).

3. Each event in this sample is fed through a Gaussian error generator to simulate a set of 35 "measured" Z values – a synthetic spectrum. (Note: the results of the previous Monte-Carlo simulation demonstrated a point-spread function very close to Gaussian – see Section 3.3.)

4. This process is repeated and 1,000 such synthetic spectra were assembled.

5. The Z values for all synthetic spectra are totalled to create a "mean sample".

6. A Kolmogorov-Smirnov test is applied between each of the synthetic spectra and this mean sample. The same test is applied between the empirically-measured spectrum and the mean sample.

7. The fraction of the simulated dataset (i.e., synthetic spectra) that lie further from the mean than the real (i.e., empirically-measured) dataset is calculated. For example, if it is 5% of the total sample then to a 95% confidence level, the real data are incompatible with the original hypothetical composition. An example of the distribution of synthetic spectra acording to their difference, "*d*" from the mean synthetic spectrum is shown in Figure 5.8.

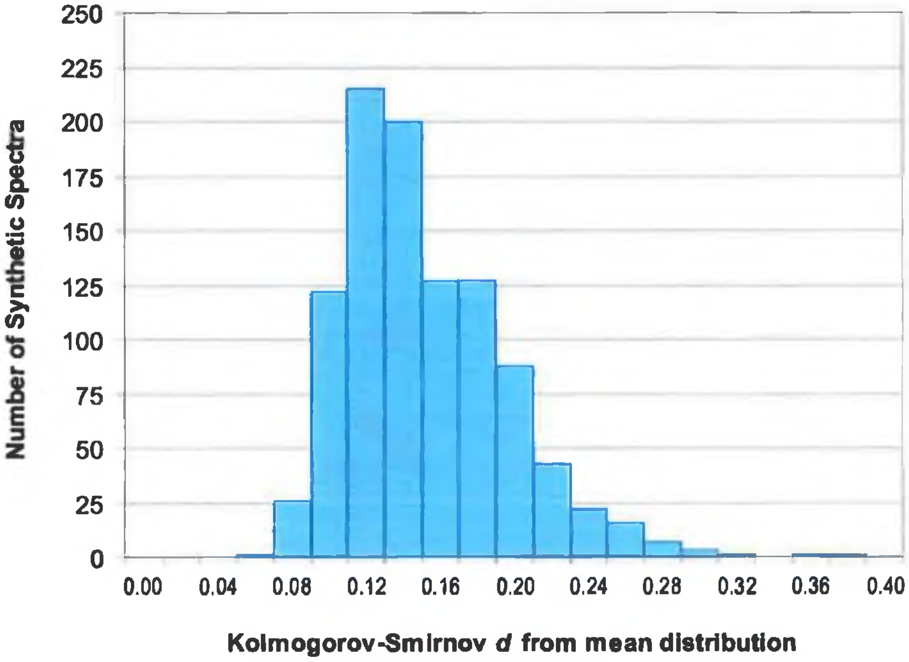

FIGURE 5.8 Example distribution of a set of synthetic spectra according to their Kolmogorov-Smirnov derived difference, *d*, from the mean of the set.

5.3.2 *Tests of the Algorithm*

To test the simulation, test spectra (each starting with a 70% $_{90}$Th content) were generated and used as "measured" data. The results (Fig. 5.9) demonstrate that the system can determine the most probable composition of the measured GCR spectrum and provide a suitable confidence interval. The scatter and differing amplitudes of the curves is due to the fact that some of the randomly-generated test spectra lie further from the original 70% $_{90}$Th content than others. In practice, this is probably the maximum scatter on such curves, as the error applied to the synthetic spectra is probably an overestimate. This test demonstrates that the method is both robust and unbiased.

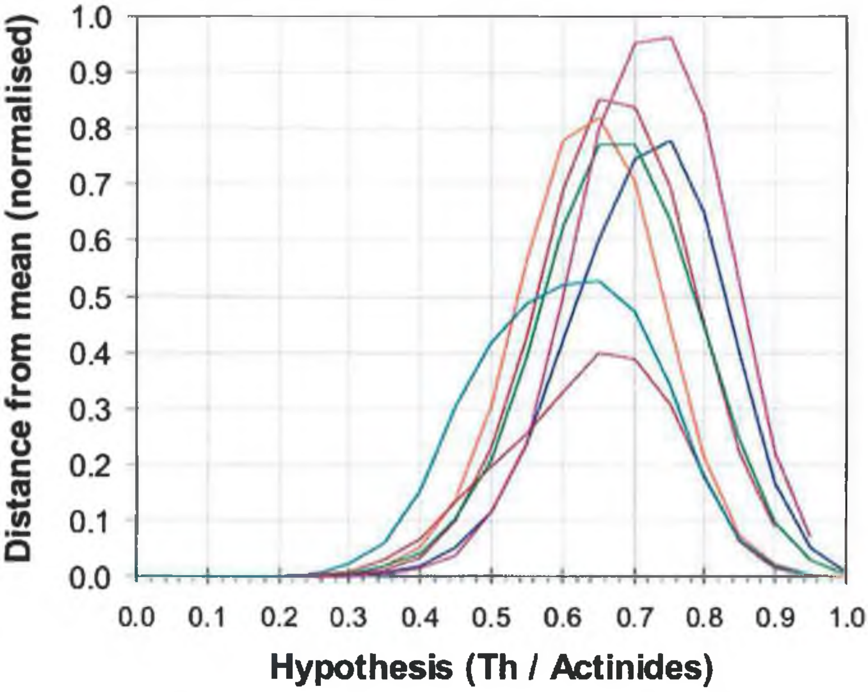

FIGURE 5.9 Seven test runs of the Monte-Carlo simulation. The ordinate on this plot denotes the fraction of a set of synthetic spectra that are further from the mean of the set than the "measured" UHCRE actinide spectrum (at various hypotheses of $_{90}$Th content in the primary spectrum). In this case, each "measured" spectrum is a different test spectrum originally containing 70% $_{90}$Th and 30% $_{92}$U.

The simulation was implemented under two different regimes. Firstly, it was assumed that there was no transuranic component in the cosmic ray flux and various hypotheses of $_{90}$Th and $_{92}$U content were tested (Section 5.3.3). In the second test, the actinide content was assumed to consist of $_{92}$U, $_{90}$Th and $_{94}$Pu only (Section 5.3.4).

5.3.3 *Results (without transuranic component)*

Assuming that the GCRs have no transuranic component, the simulation results are presented in Figs. 5.10 and 5.11 (and Table 5.3) for the actinide flux detected in the UHCRE. The UHCRE $_{92}U/_{90}Th$ ratio is estimated to be ~0.56, with confidence intervals shown in table 5.3.

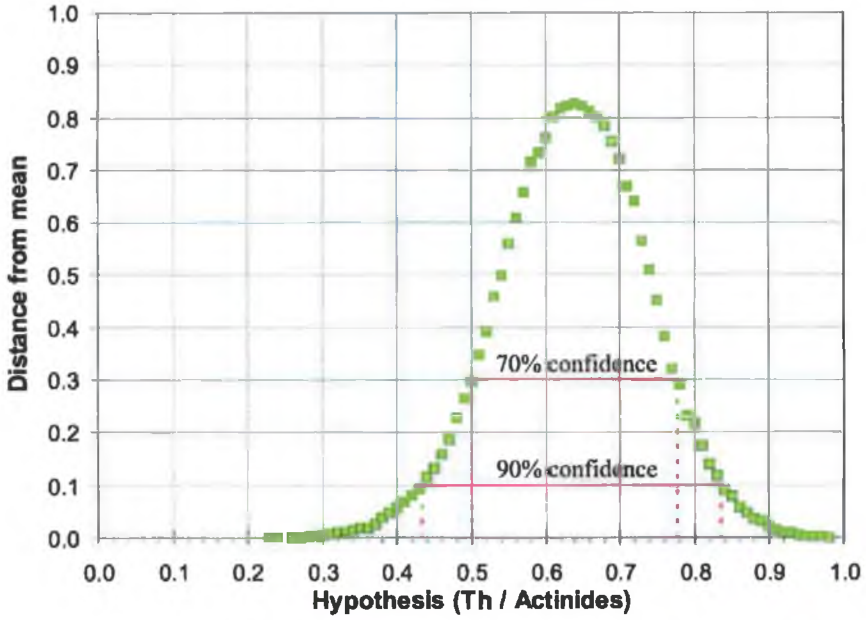

FIGURE 5.10 Fraction of a set of synthetic spectra that are further from the mean of the set than the measured UHCRE actinide spectrum at various hypotheses of $_{90}Th$ content in the GCRs.

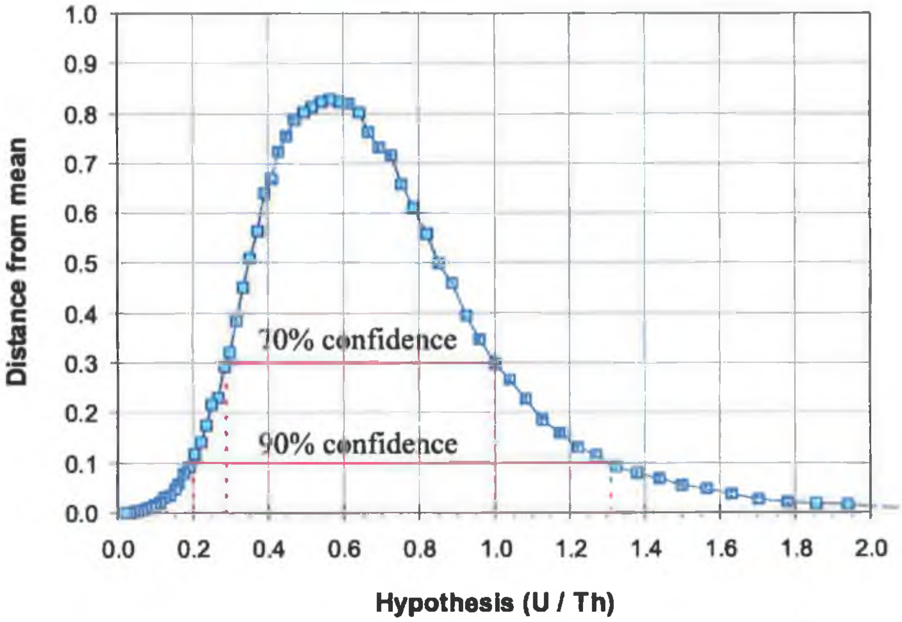

FIGURE 5.11 Fraction of a set of synthetic spectra that are further from the mean of the set than the measured UHCRE actinide spectrum at various hypotheses of $_{92}U$ / $_{90}Th$ content in the GCRs.

Table 5.3 Monte-Carlo estimates of $_{90}$Th and $_{92}$U content in the GCRs (assuming the presence of $_{90}$Th and $_{92}$U components only)

Ratio	Most likely Composition	90% confidence *lower* limit	90% confidence *upper* limit	70% confidence *lower* limit	70% confidence *upper* limit
Th / Actinides	**0.64**	0.43	0.84	0.50	0.78
$_{92}$U / $_{90}$Th	**0.56**	0.20	1.31	0.29	1.00

5.3.4 *Results (with transuranic component)*

The Monte-Carlo simulation results, assuming the presence only of $_{90}$Th, $_{92}$U and $_{94}$Pu in the cosmic rays, are summarised in Fig. 5.12 and Table 5.4. The most likely GCR composition is: 69% $_{90}$Th, 26% $_{92}$U and 5% $_{94}$Pu. Within the 70% (~1σ) confidence contours, the U/Th ratio is 0.38 with a maximum value of 0.96 and a minimum of zero. Note that though the evidence is not yet compelling, there does appear to be less uranium than thorium in the cosmic rays. If the cosmic-ray source matter originates from a single r-process source, would indicate that the time between their nucleosynthesis and acceleration is long enough to allow significant uranium decay.

Table 5.4 Monte-Carlo estimates of $_{90}$Th and $_{92}$U content in the GCRs (assuming the presence of $_{90}$Th, $_{92}$U and $_{94}$Pu components only)

Ratio	Most likely Composition	70% confidence *lower* limit	70% confidence *upper* limit
Th / Actinides	**0.69**	0.50	0.88
$_{92}$U / $_{90}$Th	**0.38**	0.00	0.96

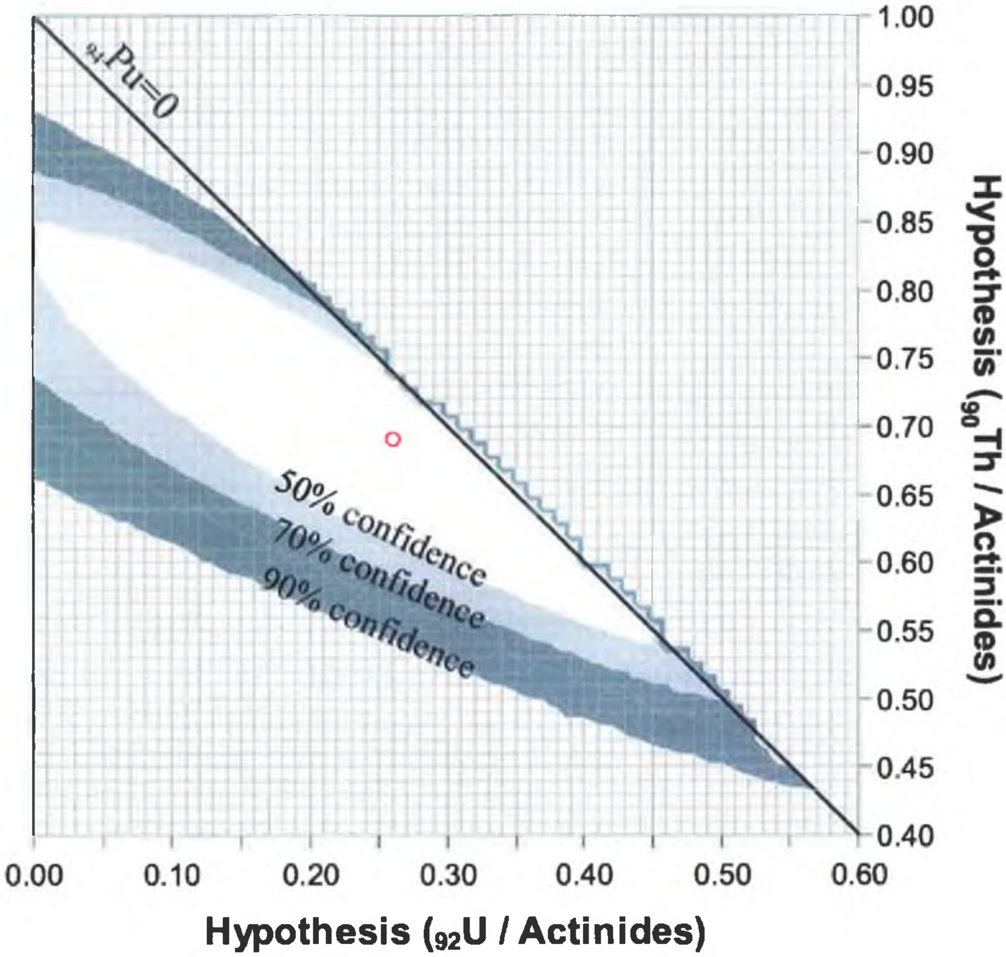

FIGURE 5.12 Fraction of a set of synthetic spectra that are further from the mean of the set than the measured UHCRE actinide spectrum at various hypotheses of $_{90}$Th and $_{92}$U content in the GCRs. Here, components of the cosmic ray flux that are not $_{90}$Th or $_{92}$U are assumed to be $_{94}$Pu. The most likely value (fractional distance from mean = 0.89) occurs at Th = 0.69 and U = 0.26.

Note that the maximum-likelihood Th-U cosmic-ray composition (0.83) is inferior to that for the maximum-likelihood Th-U-Pu composition (0.90) due to the extra degree of freedom in the simulation in the latter case.

5.4 Transuranics

The Monte-Carlo simulation indicates that, given the UHCRE actinide spectrum, the GCRs are more likely to contain a transuranic component (i.e., $_{94}$Pu) than not. The peak fractional distance from the mean in the former case was 0.90, while in the latter it was 0.83.

The detected $_{96}$Cm event was processed and measured twice, independently, with a large number of detector plates (to reduce errors). Both attempts yielded exemplary V_{eff}-gradient curves and concurring Z-assignment results.

Monte-Carlo simulations using the most likely distribution of 35 Th, U and Pu nuclei (69% Th, 26% U, 5% Pu, derived in Section 5.3.4) show that there is a ~ 18% chance of at least one of these events being binned as Cm. Using the most likely Th and U-only composition (64% Th, 36% U, derived in 5.3.3) the chance of one of the events being mistaken for Cm is only ~4%. This is a further strong indication of the existence of transuranic cosmic rays. These data are summarised in Table 5.5.

Table 5.5 Monte-Carlo estimates of spurious Cm content in the UHCRE spectrum.

GCR Composition	Chance of faux "Cm" in UHCRE sample
64% Th, 36% U	~ 4%
69% Th, 26% U, 5% Pu	~ 18%

5.5 Final Words

The UHCRE data is now the largest ever sample of ultra-heavy cosmic rays and includes the largest single sample of cosmic-ray actinides (35). The actinides are well-separated from the subactinides due to unstable nature of the elements immediately heavier than $_{83}$Bi. There are some striking features in the data.

The experiment has demonstrated that the "Pb" / "Pt"[*] abundance ratio is decidedly low in the GCRs (0.24 ± 0.03) compared to the best estimates from solar and meteoritic material (1.03 ± 0.12). Even assuming a very severe propagation effect on this ratio (×2.6), the GCR value is a mere 0.63 ± 0.09. This could be indicative of a volatility-based acceleration bias.

At $0.38^{+0.58}_{-0.38}$, the GCR U/Th ratio can be favourably compared with that of the present day ISM (0.27 ± 0.04)[†], the protosolar medium (~0.57) and the cosmic rays expected to arise from superbubble interiors (1.2 ± 0.4)[‡], though not with SB interiors themselves (1.4 ± 0.4). It does not match most predictions of r-process yields or with those of ejecta accumulated from multiple-SNe inside superbubbles over a 50 Myr period (both > ~2.3) [§].

The actinide / "Pt" ratio[||] ($0.028^{+0.006}_{-0.005}$), in broad agreement with other observations, is higher than in the present interstellar medium (0.014±0.002) and similar to that of the protosolar medium (~0.023) and the interior of superbubbles (0.029±0.005). Once propagated to the source, however, it is considerably higher. This unusually high value could be indicative of a recent r-process event. A major caveat here is that the exact effect of propagation on this ratio is unknown. The observational values are therefore best considered as lower-limits.

The presence of transuranic events in the UHCRE spectrum is intriguing as the maximum half-lives of these elements are small (81 and 15.6 Myr for $_{94}$Pu and $_{96}$Cm, respectively). Cm is the first long-lived actinide to undergo significant decay so its presence in GCRs would mean that the measured GCR actinide abundances reflect the r-process yield abundances. These are important (and poorly-constrained) parameters in predicting the age of the Galaxy. U and Th measurements in halo stars However, this approach assumes that the cosmic-ray source material originates from a single, purely r-process event – an unlikely scenario, especially given the low $_{92}$U/$_{90}$Th ratio measured by the UHCRE.

---

[*] $(81 \leqslant Z \leqslant 83) / (74 \leqslant Z \leqslant 80)$.

[†] Lodders, 2003.

[‡] Superbubble interior and superbubble cosmic-ray predictions from Lingenfelter *et al.* (2003).

[§] Lingenfelter, *et al.* (2003) and, among others, Goriely & Arnould (2001).

[||] $(Z \geqslant 88) / (75 \leqslant Z \leqslant 79)$

Taken alone, the measured $_{92}$U/$_{90}$Th ratio implies (with large errors) that the cosmic-ray source material is relatively old (> ~10^8 yr have elapsed between nucleosynthesis and acceleration). However, the probability that the UHCRE data contain at least one transuranic event is ~96% (see Table 5.5) and these have relatively short half-lives and *should not be present* if the CR-seed nuclei are old. The implication is that the cosmic-ray source material is an admixture of freshly nucleosynthesised matter (transuranics) with ordinary old ISM (material with a low U/Th ratio).

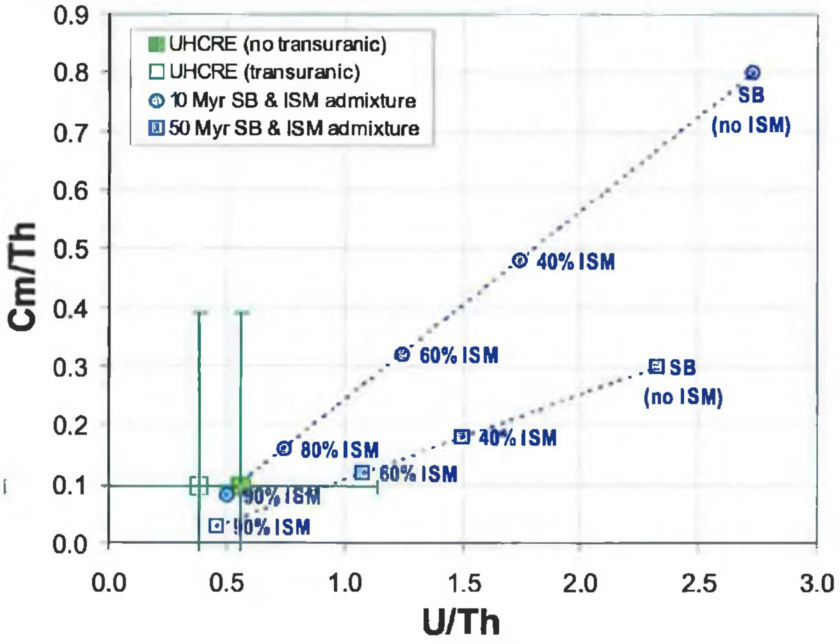

FIGURE 5.13 Actinide abundances in accumulated SN ejecta inside superbubbles over 10 and 50 Myr periods (Lingenfelter *et al.*, 2003) with admixtures of various quantities of ISM material. UHCRE data from Monte-Carlo simulations with and without a transuranic component are also plotted.

The effect of ISM dilution on SB actinide abundances can be seen in fig. 5.13. Though the calculation is crude (no error bars are published for the SB data), it appears that when sufficiently mixed with the ISM (⩾~50% ISM or so) the SB values converge with UHCRE observations.

There are many avenues for future work:

- Obviously, more primary GCR Z-abundance measurements (especially of the actinides) are required. An important point here is that currently *the statistical errors on measurements of actinide abundances are larger than detector errors*. The resolution of the detector is therefore less important than the magnitude of its exposure to the cosmic ray flux.

- Propagation models (especially for the actinides) would benefit from improved cross-section measurements. In some cases, cross-section uncertainties are still the major source of error. Simpson (1998) estimates that current propagation calculations are in error by as much as ±20-30%.

- The effects of charge pickup by ultra-heavy nuclei at moderately relativistic energies cannot be ignored. The possibility of K-capture decay after acceleration could lead to an overestimate of the age of cosmic-ray matter from actinide measurements.

- Geometrical effects (such as those from the local bubble) should also be considered. Th and U at 1 GeV/nucleon have destruction path lengths of ~0.6 g cm^{-2} in H (Wenger *et al.*, 1999) and therefore maximum ranges of ~300-500 pc. However, the low-density local bubble is a few hundred parsecs in scale and so could have a significant effect on the survival fractions of actinides arriving at earth. This is one possible explanation for the apparently high propagated GCR actinide/"Pt" ratios observed by TREK, HEAO-ARIEL and the UHCRE.

The UHCRE has demonstrated the following features in the cosmic rays:

- A statistically-significant low "Pb"/"Pt" ratio. Even assuming a very severe propagation effect on this ratio (×2.6), the GCR value is a mere 0.63 ± 0.09 compared to solar system material value of 1.03 ± 0.12. This is possibly indicative of a volatility-biased acceleration mechanism.

- The galactic cosmic rays definitely contain an actinide component. Moreover, our current knowledge of the actinide abundances is limited by statistical error and *not* by detector error.

- Within the 70% (~1σ) confidence contours, the U/Th ratio is 0.38 with a maximum value of 0.96 and a minimum of zero. This low value relative to fresh r-process material suggests that the CR matter has had sufficient time between nucleosynthesis and acceleration for radioactive decay to occur (> ~10^8 yr).

- There is evidence that suggests a $_{94}$Pu component in the cosmic rays and one $_{96}$Cm candidate event. The probability of the existence of a transuranic component is ~82% (see Table 5.4), which is indicative of freshly-synthesised matter (certainly $<\sim 10^8$ yr old).

Combined, these data suggest that the cosmic rays are a mixture of fresh (r-process enriched) and old ISM seed matter and preliminary calculations show that an admixture of accumulated SN-ejecta (such as that inside superbubbles) with the surrounding ISM agrees well with the UHCRE observations. Though the cosmic-ray mysteries remain numerous, the UHCRE has at least raised a candle to them. We await the next generation of cosmic-ray detectors to provide further illumination.

References

Adams, J.H. and Beahm, L.P., *Proc. 11th Conf. SSNTD*, Bristol, 163 (1981).

Ahlen, S.P., *Rev. Mod. Phys.* 52, 121 (1980).

Ahlen, S.P., Phys. *Rev. A*, 25, 1856 (1982).

Anders, E., Ebihara, M., *Geochimica et Cosmochimica Acta*, 46, 2363-2380 (1982).

Anders, E., Grevesse, N., *Geochimica et Cosmochimica Acta* (ISSN 0016-7037), 53, 197-214 (1989).

Arnaud, M., Casse, M., *Astron. Astrophys.*, 144, 1, 64-71 (1985).

Badavi, F.F., Townsend, L.W., Wilson, J.W. and J.W. Norbury, *Comput. Phys. Commun.* 47, 281 (1987).

Barkas, W.H., Berger, M.J., *NASA SP-3013*, Scientific and Technical Information Division, National Aeronautics and Space Administration, Washington, D.C. (1964).

Benton, E.V., Henke, R.P., *Nucl. Instrum. Meth.*, 67, 87-92 (1969).

Benton, E.V., Nix, W.D., *Nucl. Instrum. Meth.* 67, 343-347 (1969).

Bethe, H. A., *Ann. Phys.*, 5, 325 (1930).

Binns, W. R., Israel, M. H., Brewster, N. R., Fixsen, D. J., Garrard, T. L., *ApJ*, 1, 297, 111-118 (1985).

Binns, W.R., Garrard, T.L., Gibner, P.S., Israel, M.H., Kertzman, M.P., *ApJ*, 346, 997-1009 (1989).

Binns, W.R., Adams, J.H., Barbier, L.M., Christian, E.R., Cummings, A.C., Cummings, J.R., Doke, T., Hasebe, N., Hayashi, T., Israel, M.H., Leske, R.A., Mewaldt, R.A., Mitchell, J.W., Ogura, K., Schindler, S.M., Stone, E.C., Tarle, G., Tawara, H., Waddington, C.J., Westphal, A.J., Wiedenbeck, M.E., Yasuda, N., *Proc. 27th ICRC (Hamburg)* (2001).

Blake, J.B., Schramm, D.N., *Astrophysics and Space Science*, 30, 275-290 (1974).

Bosch, J., *Nucl. Insts and Methods in Physics Research Section B*, 84, 3, 357-360 (1994).

Bosch, J., Department of Physics, PhD. Thesis, Trinity College Dublin (1995).

Brewster N.R., Freier P.S. and Waddington C.J., *ApJ*, 264, 324 (1983).

Brunetti, M. T., Codino, A., *ApJ*, 528, 2, 789-798 (2000).

Cameron, A. G. W., *Space Science Reviews*, 15, 121 (1973).

Cameron, A.G.W., *Essays in Nuclear Astrophysics*, ed. C.A. Barnes, D.D. Clayton, D.N. Schramm, Cambridge University Press, 23 (1982).

Casse, M., Goret, P., *ApJ*, 1, 221, 703-712 (1978).

Cayrel, R., Hill, V., Beers, T. C., Barbuy, B., Spite, M., Spite, F., Plez, B., Andersen, J., Bonifacio, P., François, P., Molaro, P., Nordström, B., Primas, F., *Nature*, 409, 6821, 691-692 (2001).

Cherry, M.L., *Z. Phys C*, 62, 25 (1994).

Christensen-Dalsgaard, Jørgen, *Space Science Reviews*, 85, 1/2, 19-36 (1998).

Christensen-Dalsgaard, Jørgen, *Reviews of Modern Physics*, 74, 4, 1073-1129 (2002).

Clinton, Robert R., Waddington, C. J., *ApJ*, 1, 403, 2, 644-657 (1993).

Collard, H.R., L.R.B. Elton and R. Hofstadter, in *Nuclear Physics and Technology*, ed. H Schopper, Landolt-Bornstein, New Series, Group 1, 2 (Springer-Verlag, Berlin) p.30 (1967).

Connell, J. J., Simpson, J. A., *ApJ*, 475, L61 (1997).

Connell, J. J., *ApJ*, 501, L59 (1998).

Cowan, John J., Pfeiffer, B., Kratz, K.-L., Thielemann, F.-K., Sneden, Christopher, Burles, Scott, Tytler, David, Beers, Timothy C., *ApJ*, 521, 1, 194-205 (1999).

Cowan, John J., Sneden, Christopher, Burles, Scott, Ivans, Inese I., Beers, Timothy C., Truran, James W., Lawler, James E., Primas, Francesca, Fuller, George M., Pfeiffer, Bernd, Kratz, Karl-Ludwig, *ApJ*, 572, 2, 861-879 (2002).

Cummings, J. R., Binns, W. R., Garrard, T. L., Israel, M. H., Klarmann, J., Stone, E. C., Waddington, C. J., *Phys. Rev. C (Nuclear Physics)*, 42, 6, 2508-2529 (1990).

Cummings, J. R., Binns, W. R., Garrard, T. L., Israel, M. H., Klarmann, J., Stone, E. C., Waddington, C. J., *Phys. Rev. C (Nuclear Physics)*, 42, 6, 2530-2545 (1990b)

Dessart, L., Crowther, P.A., Hillier, D., Willis, A.J., Morris, P.W., van der Hucht, K.A., *Monthly Notices of the Royal Astronomical Society*, 315, 2, 407-422 (2000).

De Vries, H., C.W. de Japer and C. de Vries, *At Data Nucl. Data Tables*, 36, 495 (1987).

Domingo, C., A. Thompson, D. O'Sullivan, C. Baixeras, F. Fernandez and A. Vidal-Quadras, *Nucl. Inst. Meth.*, B51, 253-262 (1990).

Drury, L., *Space Science Reviews*, 36, 57-60 (1983).

Drury, L. O'C., Ellison, D. E., Aharonian, F. A., Berezhko, E., Bykov, A., Decourchelle, A., Diehl, R., Meynet, G., Parizot, E., Raymond, J., Reynolds, S., Spangler, S. *Space Science Reviews*, 99, 1/4, 329-352 (2001).

Du Vernois, M. A., Thayer, M. R., *ApJ*, 465, 982 (1996).

Ellison, Donald C., Reynolds, Stephen P., *ApJ*, 1, 382, 242-254 (1991).

Ellison, Donald C., Drury, Luke O'C., Meyer, Jean-Paul, *ApJ*, 487, 197 (1997).

Epstein, R. I. , *Royal Astronomical Society, Monthly Notices*, 193, 723-729 (1980).

Fermi, E., *Phys. Rev.*, 75, 1169 (1949).

Ferrando, P., *Proceedings of the 2nd International Symposium on Nuclear Astrophysics*, ed. F. Kaeppeler and K. Wisshak. Bristol: IOP Publishing, 79-90 (1993).

Fleishcher, R.L., Price, P.B., Walker, R.M., Hubbard, E.L., *Phys. Rev.*, 133, A1443 (1964).

Fleischer, R.L., Price, P.B., Walker, R.M., Maurette, M., *J. Geophys. Res.*, 72, 333-353 (1967).

Fleischer, R.L., Price, P.B., Walker, R.M., *University of California Press*, Berkeley (1975).

Fowler, P.H., Adams, R.A., Cowen, V.G., Kidd, J.M., *Proc. Roy. Soc. A.* 301, 39-45 (1967).

Fowler, P.H., Clapham, V.M., Cowen, V.G., Kidd, J.M., Moses, R.T., *Proc. Roy. Soc. Lond. A.*, 318, 1-43 (1970).

Fowler, W.A., in *Cosmology, Fusion & Other Matters*, ed. F. Reines (Boulder: Assoc. Univ. Press), 67 (1972).

Fowler, P.H., Alexandre, V.M., Clapham, V.M., Henshaw, D.L., O'Sullivan, D., Thompson, A., *Proc. 15th ICRC (Plovdiv, Bulgaria)*, 11, 165-173 (1977).

Fowler, P.H., Walker, R.N.F., Masheder, M.R.W., Moses, R.T., Worley, A., Gay, A.M., *ApJ*, 314, 739-746 (1987).

Freier, P., Lofgren, E.J., Ney E.P., Oppenheimer, F., Bradt, H.L., Peters, B., *Phys. Rev.*, 74, 7 (1948).

Geer, L.Y., J. Klarmann, B.S. Nilsen, C.J. Waddington, W.R. Binns, J.R. Cummings and T.L. Garrard, *Phys. Rev. C (Nuclear Physics)*, 52, 1, 334-345, (1995).

Gehrels, N., *ApJ*, 303, 336-346 (1986).

Goriely, S., Arnould, M., *Astron. Astrophys.*, 379, 1113-1122 (2001).

Greiner, D. E., Crawford, H., Lindstrom, P. J., Kidd, J. M., Olson, D. L., Schimmerling, W., Symons, T. J. M., *Phys. Rev. C (Nuclear Physics)*, 31, 2, 416-420 (1985).

Grevesse, N., Meyer, J. P., *Proc. 19th ICRC (La Jolla)*, 3, 5-8 (1985).

Grevesse, Nicolas, Anders, Edward, *Cosmic abundances of matter*, Proceedings of the AIP Conference, (Minneapolis, MN), New York, American Institute of Physics, 183, 1-8 (1989).

Grevesse, N., Sauval, A.J. Standard Solar Composition, *Space Science Reviews*, 85, 161-174 (1998).

Higdon, J. C., Lingenfelter, R. E., Ramaty, R., *ApJ*, 509, 1, L33-L36 (1998).

Hillas, A.M., *Ann. Rev. Astr. Astrophys.*, 22, 425 (1984).

Hizebruch, S.E., E. Becker, G. Hüntrup, T. Steibel, E. Winkel and W. Heinrich, *Phys. Rev. C (Nuclear Physics)*, 51, 4 (1995).

Kratz, K-L., Bitouzet, J-P., Thielemann, F-K., Moeller, P., Pfeiffer, B., *ApJ*, Part 1, 403, 1, p. 216-238 (1993).

Leske, R.A., *ApJ*, 405, 567 (1993).

Levine, A.S. (ed.) *LDEF-69 Months in Space, first post-retrieval symposium*, Part 1 (1991).

Lingenfelter, R.E., Ramaty, R., Kozlovsky, B., *ApJ*, 500, L153 (1998).

Lingenfelter, R. E., Higdon, J. C., Kratz, K.-L., Pfeiffer, B., *ApJ*, 591, 1, 228-237 (2003).

Lodders, Katharina, *ApJ*, 591, 2, 1220-1247 (2003).

Longair, M.S., *High Energy Astrophysics, vol. 2*, Cambridge University Press (1997).

Lukasiak, A., McDonald, F. B., Webber, W. R., Ferrando, P., *Adv. Space Res.*, 19, 747 (1997).

Mac Low, Mordecai-Mark, McCray, Richard, *ApJ*, Part 1, 324, 776-785 (1988).

Maeder, A., Meynet, G., *Astron. Astrophys.*, 278, 2, 406-414 (1993).

Maeder, A., Meynet, G. *Astron. Astrophys.* 287, 803-816 (1994).

Meyer, J.-P., *ApJ Supplement Series*, 57, 173-204 (1985).

Meyer, Jean-Paul, O'C. Drury, Luke, Ellison, Donald C., *Space Science Reviews*, 86, 1/4, 179-201 (1998).

Moseley, H., Dwek, E., Glaccum, W., Graham, J., Loewenstein, R., Silverberg, R., *Bulletin of the American Astronomical Society*, 21, 1215 (1989).

Moseley, S. H., Dwek, E., Glaccum, W., Graham, J. R., Loewenstein, R. F., *Nature*, 340, 697-699 (1989b).

Nilsen, B. S., Waddington, C. J., Cummings, J. R., Garrard, T. L., Klarmann, J., *Phys. Rev. C (Nuclear Physics)*, 52, 6, 3277-3290 (1995).

Olson, D.L., B. L. Berman, D.E. Greiner, H.H. Heckman, P.J. Lindstrom and H.J. Crawford, *Phys. Rev. C (Nuclear Physics)*, 28, 1602 (1983).

O'Sullivan, D., Thompson, A., *Nuclear Tracks and Radiation Measurements*, 4, 271-276 (1980).

Parizot, Etienne M. G., *Astron. Astrophys.*, 331, 726-736 (1998).

Parizot, E., Drury, L., *Astron. Astrophys.*, 349, 673-684 (1999).

Perelygin, V.P., Stetsenko, S.G., Lhagvasuren, D., Otgonsuren, O., Pellas, P., & Jakupi, B., *Proc. 15th ICRC (Plovdiv, Bulgaria)*, 1, (1977).

Peterson, D.D., *Rev. of Sci. Instr.*, 41, 1252-1253 (1970).

Pfeiffer, B., Kratz, K.-L., Thielemann, F.-K., *Z. Phys. A*, 357, 235-238 (1997).

Pierce, T.E. and Blann, M., *Phys. Rev.*, 173, 390 (1968).

Ramatay, R., Kozlovsky, B. and Lingenfelter, R., *Physics Today*, April, 30 (1998).

Salamon, M.H., Price, B.P. and Drach, J., *Nucl. Inst. Meth.*, B17, 173-176 (1986).

Sampair, T.R., *High-resolution study of Ultra-Heavy Cosmic-Ray Nuclei. A0178-UHCRE Postflight Thermal Analysis*. Lockheed Engineering & Sciences Co. (1991).

Shapiro, M. M., Silberberg, R., *Proc. 11th ICRC (Budapest)*, ed. A. Somogyi, Vol. 1. Acta Physica, Supplement to Vol. 29, 485 (1970).

Shirk, E.K., Price, P.B., *ApJ*, 220, 719-733 (1978).

Sihver, L., C.H. Tsao, R. Silberberg, T. Kanai, and A.F. Barghouty, *Phys. Rev. C (Nuclear Physics)*, 47, 1225 (1993).

Simpson, J.A., *Ann. Rev. Nucl. Part. Sci.*, 33, 326 (1983).

Simon, M., Heinrich, W. and Mathis, K.D., *ApJ*, 300, 32 (1986).

Simpson, J. A., *Space Science Reviews*, 86, Issue 1/4, 23-50 (1998).

Silberberg, R., Tsao, C. H., *ApJ Supplement*, 25, 315-333 (1973a).

Silberberg, R., Tsao, C. H., *ApJ Supplement*, 25, 335-367 (1973b).

Silberberg, R. and C.H. Tsao, *Phys. Rep.*, 191, 351 (1990).

Sneden, Christopher, McWilliam, Andrew, Preston, George W., Cowan, John J., Burris, Debra L., Armosky, Bradley J., *ApJ*, 467, 819 (1996).

Soutoul, A., Legrain, R., Lukasiak, A., McDonald, F. B., Webber, W. R., *Astron. Astrophys.*, 336, L61-L64 (1998).

Sternheimer, R.M. and Peierls, R.F., *Phys. Rev. B*, 3, 3681 (1971).

Thielemann, F.-K., Metzinger, J., Klapdor, H. V., *Astron. Astrophys.*, 123, 1, 162-169 (1983).

Thompson, A., O'Sullivan, D., Wenzel, K.-P., Domingo, C., O'Ceallaigh, C., Daly, J. & Smit, A., *Nucl. Tracks and Rad. Meas.*, 8, 1-4, 575-578 (1979).

Thompson, A. and O'Sullivan, D., *Nucl. Tracks and Rad. Meas.*, 8, 567-570 (1984).

Thompson, A., O'Sullivan, D., Wenzel, K.-P., Domingo, V., Domingo, C., Daly, J., Smit, A., *Proc. 21st ICRC (Adelaide)*, 441-444 (1990).

Thompson, A., O'Sullivan, D., Wenzel, K.-P., Bosch, J., Keegan, R., Domingo, C., Jansen, F., *Proc. 23rd ICRC (Calgary)*, 603-606 (1993).

Townsend, L. W., Khan, F., Tripathi, R. K., *Phys. Rev. C (Nuclear Physics)*, 48, 6, 2912-2919 (1993).

Tsao, C.H., R. Silberberg and A.F. Barghouty, L. Sihver and T. Kanai, *Phys. Rev. C (Nuclear Physics)*, 47, 1257 (1993).

Tsujimoto, Takuji, Shigeyama, Toshikazu *ApJ*, 561, 1, L97-L100. (2001)

Waddington, C. J., Binns, W. R., Brewster, N. R., Fixsen, D. J., Garrard, T. L., Israel, M. H., Klarmann, J., Newport, B. J., Stone, E. C., *Proc. 19th ICRC (La Jolla)*, vol. 9, 4 (1986).

Waddington, C. Jake, *ApJ*, 470, 1218 (1996).

Waddington, C. Jake, *Advances in Space Research*, 19, 5, 759-762 (1997).

Waddington, C.J., J.R. Cummings and B.S. Nilsen, *Proc. 26th ICRC (Salt Lake City)*, HE 1.1.15 (1999^{a}).

Waddington, C.J., J.R. Cummings, B.S. Nilsen and T.L. Garrard, *ApJ*, 519, 214-221, (1999^b)

Watson, A.A., *Proc. 19th ICRC (La Jolla)*, 9, 111 (1985).

Wdowczyk, J. and Wolfendale, A.W., *Ann. Rev. Nucl. Part. Sci.*, 39, 43 (1989).

Webber, W.R., *ApJ*, 179, 277 (1987).

Webber, W.R., *ApJ*, 402, 188 (1993).

Webber, W.R. and McDonald, F.B., *ApJ*, 435, 464 (1994).

Webber, W.R., *Publ. Astron. Soc. Pacific*, 18, 37 (1994).

Webber, W.R., *Space Science Reviews*, 81, 107-142 (1997).

Webber, W.R., J.C. Kish and D.A. Schrier, *Phys. Rev. C (Nuclear Physics)*, 41, 520 (1990).

Weidenbeck, M.E., Binns, W.R., Christian, E.R., Cummings, A.C., Dougherty, B.L., Hink, P.L., Klarmann, J., Leske, R.A., Lijowski, M., Mewaldt, R.A., Stone, E.C., Thayer, M.R., von Rosenvinge, T.T. and Yanasak, N.E., *ApJ*, 523, L61-L64 (1999).

Wenger, H.U., et al, *Ann. Nucl. Energy*, 26, 141 (1999).

Westfall, G.D., Wilson, L.W., Linstrom, P.J., Crawford, H.J., Greiner, D.E. and Heckman, H.H., *Phys. Rev. C (Nuclear Physics)*, 19, 4, 1309-1323 (1979).

Westphal A.J., Price P.B., Weaver B.A., Afanasiev V.G., Nature, 396, 50 (1998).

Wielen, R., Fuchs, B., Dettbarn, C. *Astron. Astrophys.*, 314, 438 (1996).

Willis, A., Dessart, L., Crowther, P., Morris, P., van der Hucht, K., Boulder-Munich II: Properties of Hot, Luminous Stars, ed. Ian Howarth, ASP Conference Series vol. 131, 66 (1998).

Woosley, S. E., Weaver, T.A., *ApJ Supplement* 101, 181 (1995).

Yanasak, N. E., Wiedenbeck, M. E., Mewaldt, R. A., Davis, A. J., Cummings, A. C., George, J. S., Leske, R. A., Stone, E. C., Christian, E. R., von Rosenvinge, T. T., Binns, W. R., Hink, P. L., Israel, M. H., *ApJ*, 563, 2, 768-792. (2001).

Appendix A: Mean Excitation Potential Calculations

The Bragg rule of additivity assumes that the value of I_{adj} (the mean excitation potential for electrons) of a molecular stopping material is computed from the I_{adj}'s of the individual constituent elements of the material. For the i^{th} constituent,

$$(I_{adj})_i = (12Z_i + 7)\ \text{eV for } Z < 13^{*}$$

and

$$(I_{adj})_i = \{(9.76Z_i + (58.8/Z_i^{0.19})\}\ \text{eV for } Z \geqslant 13$$

From Benton and Henke (1969), for a compound the I_{adj} is given by the individual values of I_{adj} of its component elements:

$$\ln I_{adj} = \langle A/Z \rangle \sum_i \{f_i Z_i / A_i\} \ln (I_{adj})_i$$

where f_i is the fraction by weight of the i^{th} component of the stopping material and A_i and Z_i are the atomic weight and atomic number of the i^{th} component.

Here, $\langle A/Z \rangle = \sum_i \mu_i A_i / \sum_i \mu_i Z_i = \left[\sum_j f_i (Z_i / A_i) \right]^{-1}$ and for a molecular material, $f_i = \mu_i A_i / \sum_j \mu_j A_j$, where μ_i is the formula number of the i^{th} component. The calculations for Lexan (stoichiometric formula $C_{16}H_{14}O_3$) are shown below:

	C	H	O		
μ	16	14	3		
A	12.0	1.0	16.0		
f	0.76	0.06	0.19		
Z	6	1	8	$\Sigma(fZ/A)\ln I_{adj}$	
$(fZ/A)\ln I_{adj}$	1.65	0.15	0.43	2.23	
I_{adj}	79	16.5	96		
μ / A	192.2	14.1	48.0	254.3	Σ(μ / A)
μ / Z	96.0	14.0	24.0	134.0	Σ(μ / Z)

Lexan

$C_{16}H_{14}O_3$

A / Z	$\Sigma\{(fZ/A)\ln I_{adj}\}$	I_{adj} (total)
1.90	2.23	69.5

---

[*] These empirical expressions of the experimental results are only approximate for $Z < 13$.

Appendix B: The Actinides

The measured data for all 35 UHCRE actinides are presented below. The events are labelled in the format STACK NUMBER/EVENT NUMBER. Stack locations on the LDEF spacecraft are detailed in Appendices C and D.

2σ error bars are shown on all plots and measurements marked in grey have been removed in quality control procedures. The assigned *Z* and estimates of the errors on this value due to errors in both V_{eff} and in gradient are stated. The remaining error of ±0.6e (due to the registration temperature effect) has been included in these error estimates. Note that the track-etch rates of these events have *not* been adjusted for etching variation. For each event, the time, bulk-etch rate and track-etch rate monitor (TERM) variation from the mean is also included.

Event	215 / 3	pathlength	V_T
Assigned Z	88.2	(g cm^{-2})	(microns hr^{-1})
error (+)	1.4	0.11	1.82
error (-)	1.3	0.13	1.86
		0.25	1.76
Etch Time (hrs)	48	0.28	1.82
Mean V_0 (μm hr^{-1})	0.164	0.57	1.83
TERM variation	5.5%	0.59	1.81
		1.07	1.83
		1.09	1.94
		1.61	1.96
		1.63	1.93
		1.96	1.84
		1.98	1.84
		2.14	1.84
		2.16	1.88
		2.24	2.08
		2.26	2.26
		2.42	2.20
		2.44	2.18
		2.49	1.94
		2.51	1.95

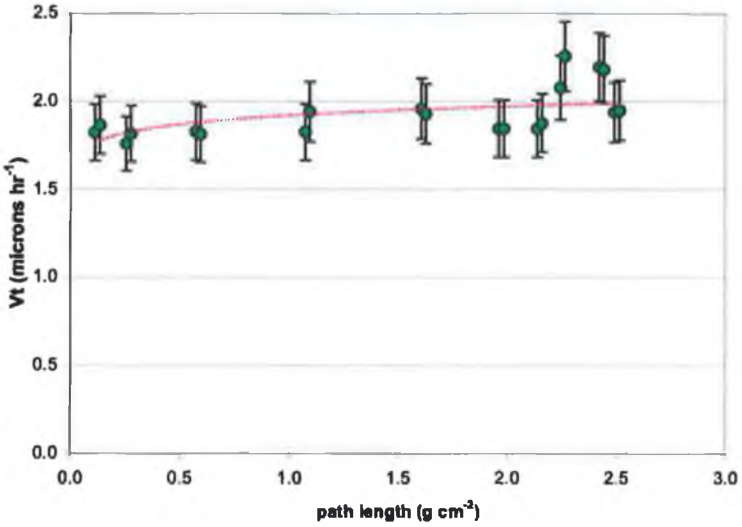

Event	215 / 14	pathlength	V_T
Assigned Z	87.9	(g cm^{-2})	(microns hr^{-1})
error (+)	2.0	0.10	1.38
error (-)	2.0	0.12	1.39
		0.23	1.36
Etch Time (hrs)	48	0.26	1.37
Mean V_0 (μm hr^{-1})	0.164	0.53	1.45
TERM variation	5.5%	0.55	1.56
		0.99	1.34
		1.01	1.37
		1.49	1.31
		1.51	1.35
		1.82	1.42
		1.84	1.37
		1.98	1.29
		2.00	1.32
		2.08	1.29
		2.10	1.36
		2.24	1.50
		2.26	1.58
		2.30	1.50
		2.32	1.57

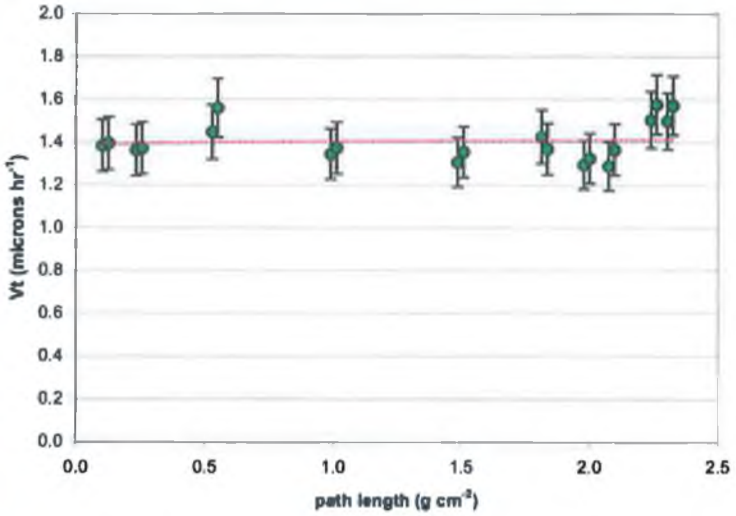

Event	24 / 7	pathlength	V_T
Assigned Z	90.1	(g cm^{-2})	(microns hr^{-1})
error (+)	1.3	0.04	1.54
error (-)	1.3	0.06	1.54
		0.10	1.55
Etch Time (hrs)	48	0.12	1.51
Mean V_G (μm hr^{-1})	0.153	0.23	1.58
TERM variation	0.4%	0.25	1.62
		0.78	1.59
		0.80	1.50
		1.23	1.49
		1.25	1.56
		1.75	1.59
		1.77	1.53
		2.79	1.41
		2.81	1.48
		3.72	1.51
		3.74	1.46
		3.94	1.50
		3.96	1.49
		4.04	1.52
		4.06	1.53

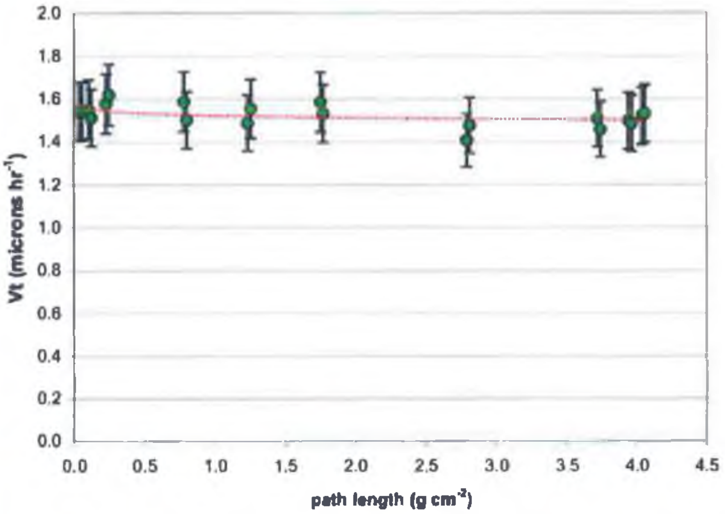

Event	24 / 8	pathlength	V_T
Assigned Z	93.1	(g cm^{-2})	(microns hr^{-1})
error (+)	1.0	0.04	1.83
error (-)	1.2	0.07	1.74
		0.11	1.75
Etch Time (hrs)	48	0.14	1.68
Mean V_G (μm hr^{-1})	0.153	0.26	1.77
TERM variation	0.4%	0.28	1.79
		0.90	1.88
		0.92	1.83
		1.42	1.93
		1.45	1.84
		2.02	1.67
		2.05	1.73
		3.22	1.81
		3.25	1.81
		4.30	1.79
		4.32	1.77
		4.55	1.87
		4.58	1.88
		4.66	1.86
		4.69	1.82

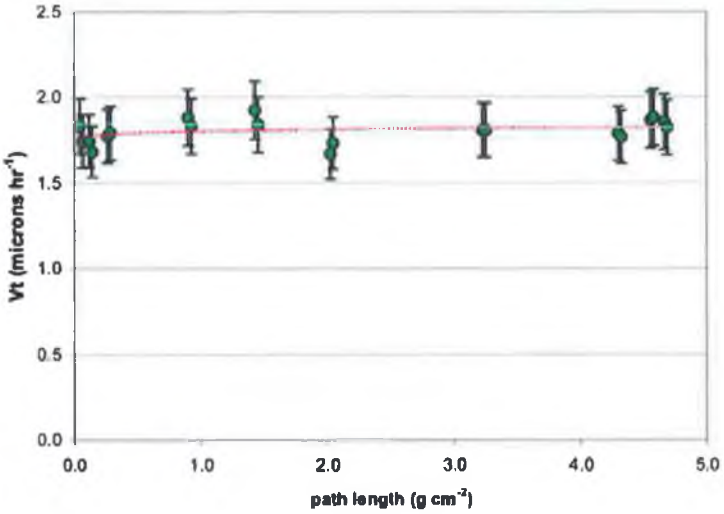

Event	27 / 17	pathlength	V_T
Assigned Z	92.3	(g cm^{-2})	(microns hr^{-1})
error (+)	0.8	0.08	1.71
error (-)	1.2	0.10	1.74
		0.19	1.67
Etch Time (hrs)	48	0.21	1.68
Mean V_G (μm hr^{-1})	0.153	0.30	1.64
TERM variation	0.4%	0.32	1.66
		0.93	1.63
		0.96	1.68
		2.06	1.69
		2.08	1.67
		2.62	1.72
		2.65	1.70
		3.82	1.57
		3.85	1.68
		4.33	1.55
		4.36	1.75
		4.52	1.61
		4.54	1.68
		4.66	1.64
		4.69	1.70

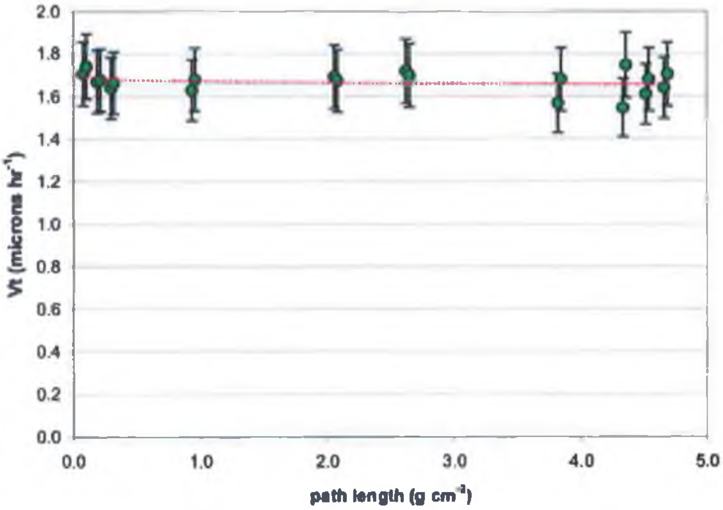

Event	45 / 16	pathlength	V_T
Assigned Z	91.3	(g cm^{-2})	(microns hr^{-1})
error (+)	1.3	0.08	1.51
error (-)	1.0	0.10	1.55
		0.23	1.59
Etch Time (hrs)	48	0.25	1.49
Mean V_G (μm hr^{-1})	0.153	0.85	1.63
TERM variation	0.4%	0.88	1.56
		1.43	1.54
		1.46	1.61
		1.98	1.62
		2.01	1.57
		3.26	1.68
		3.28	1.59
		4.03	1.50
		4.06	1.62
		4.44	1.58
		4.47	1.65
		4.70	1.56
		4.73	1.58
		4.85	1.71
		4.88	1.66

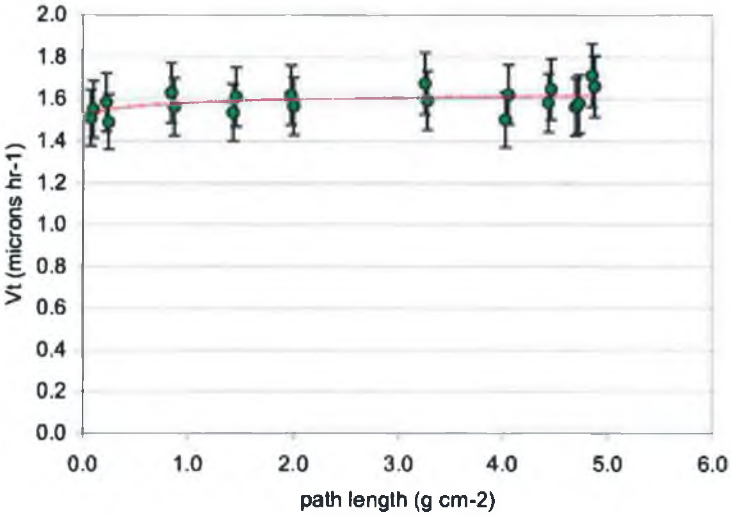

Event	58 / 3	pathlength	V_T
Assigned Z	89.8	(g cm^{-2})	(microns hr^{-1})
error (+)	1.0	0.20	2.44
error (-)	0.9	0.22	2.50
		1.76	2.23
Etch Time (hrs)	36.5	1.78	2.23
Mean V_G (μm hr^{-1})	0.159	2.72	2.21
TERM variation	-6.9%	2.74	2.23
		2.75	2.20
		2.77	2.14
		3.28	2.10
		3.31	2.12
		3.64	2.08
		3.66	2.07
		3.86	2.08
		3.88	2.08
		3.93	2.03
		3.95	2.04
		3.99	2.03
		4.01	2.09
		4.09	1.99
		4.11	1.95

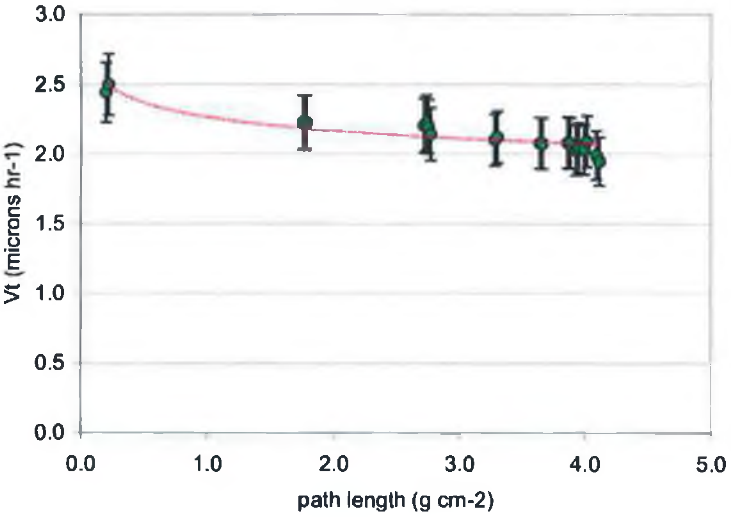

Event	103 / 14	pathlength	V_T
Assigned Z	90.5	(g cm^{-2})	(microns hr^{-1})
error (+)	1.1	0.23	1.77
error (-)	1.2	0.25	1.76
		1.36	1.66
Etch Time (hrs)	62	1.38	1.68
Mean V_G (μm hr^{-1})	0.137	1.96	1.69
TERM variation	-7.7%	1.99	1.67
		2.49	1.76
		2.51	1.72
		3.13	1.67
		3.15	1.74
		3.73	1.63
		3.76	1.62
		4.26	1.61
		4.28	1.63
		4.41	1.67
		4.43	1.73
		4.56	1.56
		4.59	1.54
		4.71	1.67
		4.73	1.67

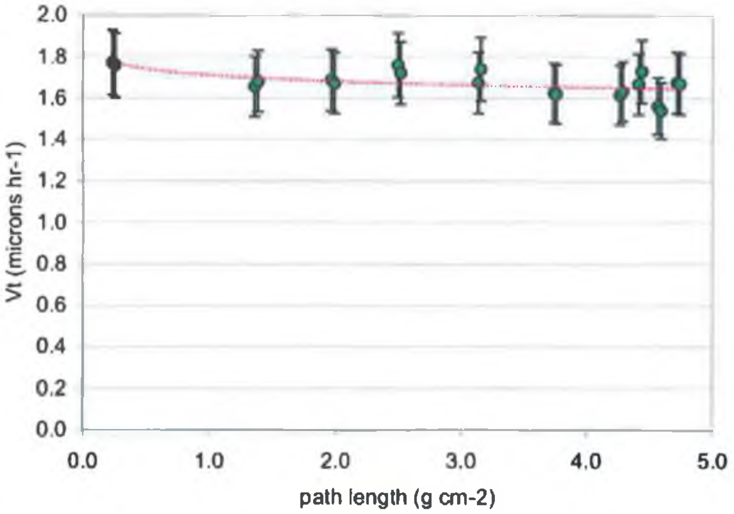

110 / 8	pathlength	V_T
91.2	(g cm^{-2})	(microns hr^{-1})
1.2	0.10	2.12
1.0	0.12	2.14
	0.19	2.18
42	0.21	2.18
0.144	0.74	2.30
6.7%	0.76	2.19
	1.19	2.07
	1.21	2.06
	1.64	2.20
	1.66	2.10
	2.16	2.11
	2.17	2.02
	3.15	2.12
	3.17	1.88
	3.66	1.90
	3.67	1.87
	4.03	1.93
	4.05	1.87
	4.13	1.89
	4.15	1.99

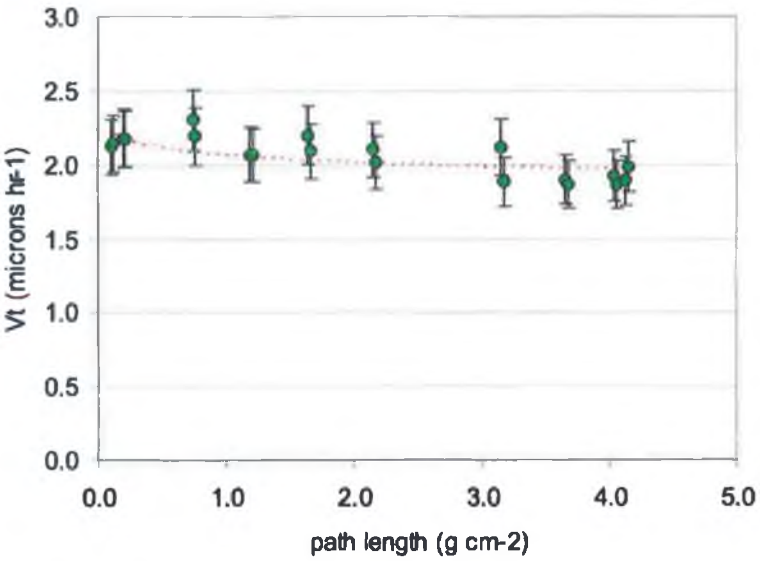

126 / 16	pathlength	V_T
95.9	(g cm^{-2})	(microns hr^{-1})
0.9	0.01	2.27
1.1	0.03	2.28
	0.21	2.33
41	0.23	2.39
0.164	0.32	2.39
5.4%	0.34	2.37
	0.78	2.28
	0.81	2.26
	1.32	2.42
	1.34	2.41
	1.86	2.47
	1.88	2.48
	2.43	2.35
	2.45	2.36
	2.93	2.50
	2.95	2.63
	3.50	2.42
	3.52	2.47
	3.67	2.57
	3.69	2.56
	3.85	2.58
	3.87	2.54
	4.05	2.40
	4.07	2.47
	4.23	2.41
	4.25	2.45
	4.43	2.55
	4.46	2.55
	4.54	2.45
	4.56	2.60

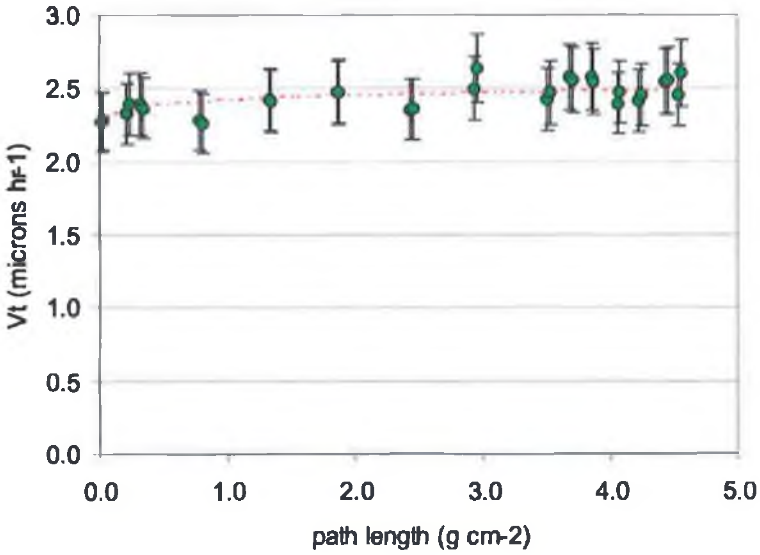

Event	166 / 15	pathlength	V_T
Assigned Z	92.9	(g cm^{-2})	(microns hr^{-1})
error (+)	0.9	1.24	4.26
error (-)	0.9	1.26	4.32
		1.73	4.20
Etch Time (hrs)	18	1.75	4.34
Mean V_G (μm hr^{-1})	0.159	2.19	3.86
TERM variation	-6.9%	2.21	3.82
		2.50	3.62
		2.52	3.51
		2.91	3.66
		2.93	3.65
		3.26	**3.90**
		3.28	**3.11**
		3.60	3.35
		3.63	3.27
		3.70	3.19
		3.72	3.33
		3.82	3.15
		3.85	3.27
		3.95	3.23
		3.97	3.17

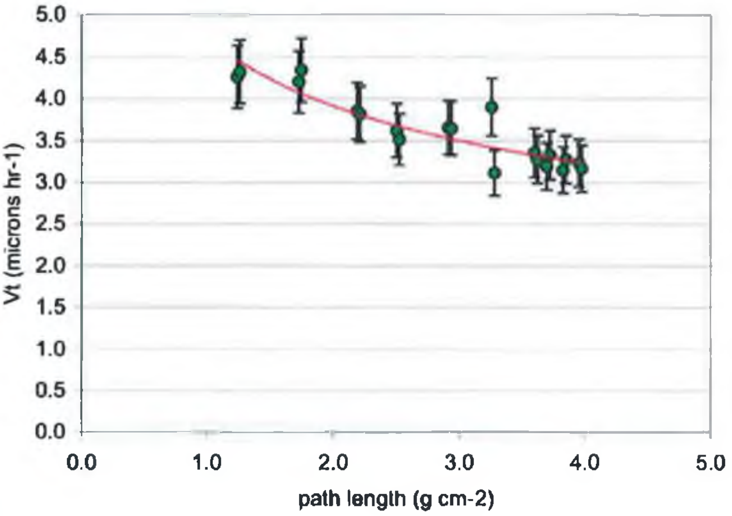

Event	158 / 32	pathlength	V_T
Assigned Z	90.1	(g cm^{-2})	(microns hr^{-1})
error (+)	1.4	0.12	1.50
error (-)	1.2	0.14	1.43
		0.27	1.46
Etch Time (hrs)	60	0.30	1.46
Mean V_G (μm hr^{-1})	0.167	0.31	1.46
TERM variation	7.6%	0.33	1.49
		0.89	1.47
		0.92	1.44
		2.06	1.44
		2.09	1.48
		3.03	**1.29**
		3.05	**1.36**
		3.75	1.42
		3.78	1.44
		4.44	1.40
		4.46	1.38
		4.67	1.43
		4.69	1.41

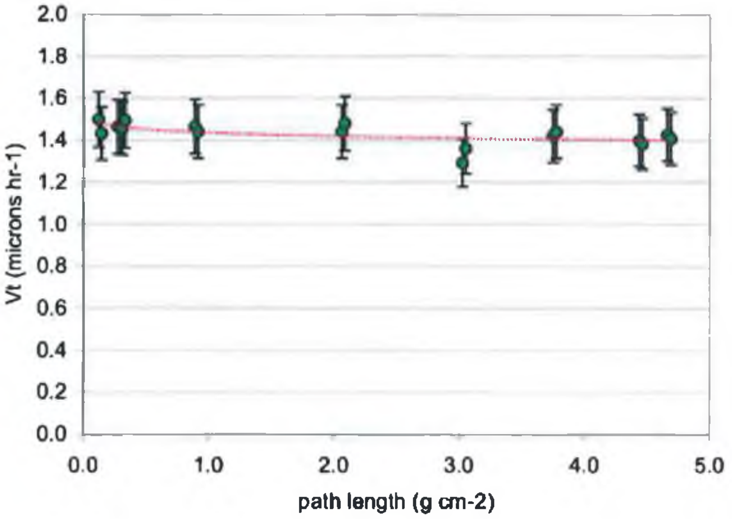

Event	161 / 14	pathlength	V_T
Assigned Z	91.6	(g cm^{-2})	(microns hr^{-1})
error (+)	1.2	0.10	1.62
error (-)	1.3	0.12	1.75
		0.20	1.75
Etch Time (hrs)	48	0.22	1.72
Mean V_G (μm hr^{-1})	0.164	0.72	1.59
TERM variation	5.5%	0.74	1.72
		1.24	1.70
		1.26	1.79
		1.70	1.67
		1.72	1.68
		2.23	**1.88**
		2.25	**1.76**
		2.70	1.57
		2.72	1.63
		3.18	1.58
		3.20	1.64
		3.50	1.65
		3.52	1.76
		3.82	1.65
		3.84	1.70

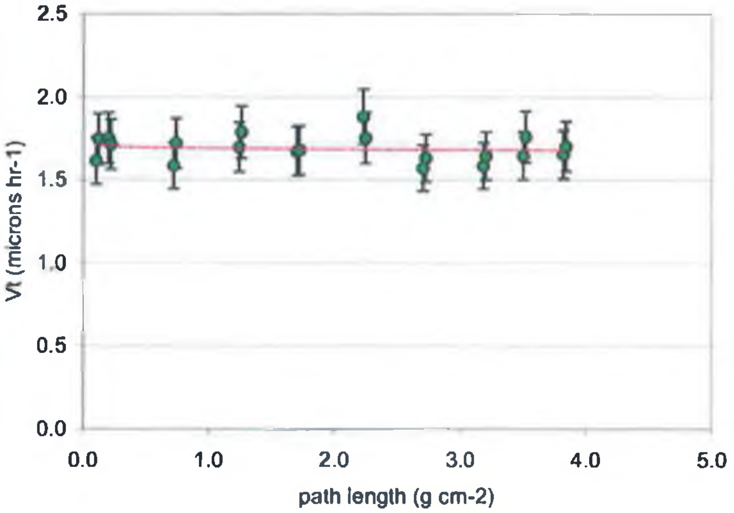

Event	202 / 3	pathlength	V_T
Assigned Z	89.2	(g cm^{-2})	(microns hr^{-1})
error (+)	0.7	0.18	1.27
error (-)	1.9	0.19	1.41
		0.24	1.30
Etch Time (hrs)	72.5	0.26	1.41
Mean V_G (μm hr^{-1})	0.142	1.21	1.22
TERM variation	-7.8%	1.24	1.23
		1.28	1.20
		1.30	1.26
		1.70	1.23
		1.72	1.35
		2.32	1.32
		2.34	1.39
		2.46	1.32
		2.48	1.36
		2.59	1.29
		2.62	1.37
		2.66	1.25
		2.68	1.40
		2.73	1.27
		2.75	1.38

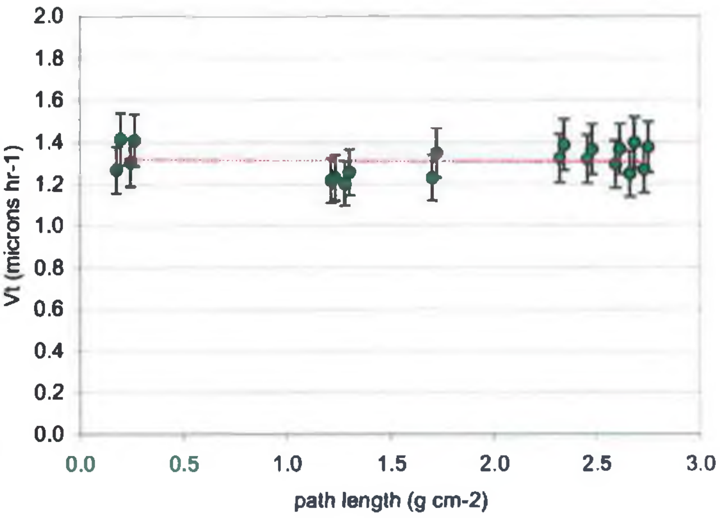

Event	40 / 10	pathlength	V_T
Assigned Z	89.7	(g cm^{-2})	(microns hr^{-1})
error (+)	0.9	1.89	1.32
error (-)	1.4	1.91	1.33
		2.28	1.36
Etch Time (hrs)	72	2.30	1.37
Mean V_G (μm hr^{-1})	0.158	2.81	1.34
TERM variation	4.8%	2.83	1.40
		2.88	1.36
		2.90	1.36
		3.37	1.32
		3.39	1.36
		3.75	1.31
		3.77	1.38
		3.78	1.36
		3.80	1.39
		3.85	1.31
		3.87	1.35
		4.05	1.38
		4.07	1.41

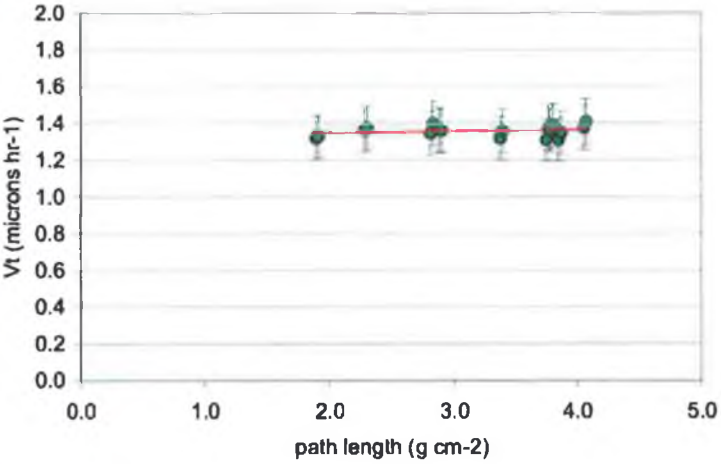

Event	202 / 10	pathlength	V_T
Assigned Z	90.0	(g cm^{-2})	(microns hr^{-1})
error (+)	0.9	0.24	1.45
error (-)	1.4	0.27	1.46
		0.34	1.41
Etch Time (hrs)	72.5	0.37	1.48
Mean V_G (μm hr^{-1})	0.142	1.70	1.37
TERM variation	-7.8%	1.73	1.42
		1.79	1.36
		1.82	1.44
		2.38	1.37
		2.41	1.41
		3.25	1.44
		3.28	1.38
		3.44	1.41
		3.47	1.47
		3.63	1.50
		3.66	1.49
		3.72	1.44
		3.75	1.45
		3.82	1.45
		3.85	1.46

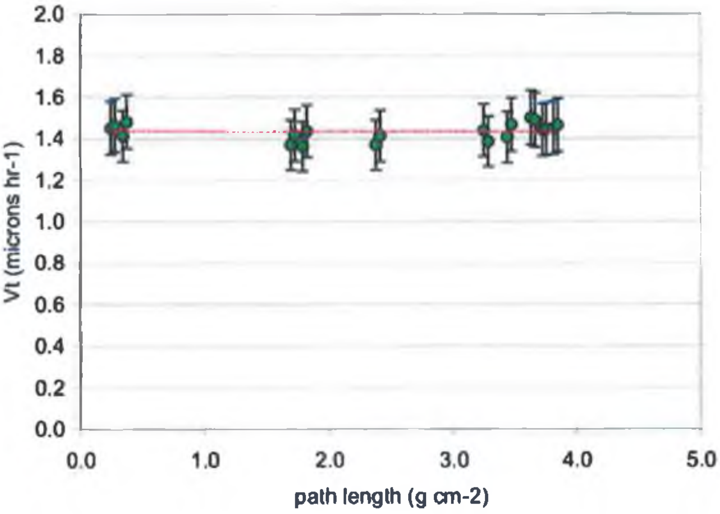

Event	190 / 3
Assigned Z	91.5
error (+)	1.2
error (-)	1.6
Etch Time (hrs)	46
Mean V_G (μm hr^{-1})	0.137
TERM variation	-6.3%

pathlength (g cm^{-2})	V_T (microns hr^{-1})
0.21	1.64
0.23	1.66
0.48	1.65
0.51	1.65
0.58	1.61
0.61	1.65
0.86	1.65
0.88	1.63
1.27	1.67
1.29	1.72
1.75	1.72
1.77	1.65
2.16	1.60
2.18	1.64
2.53	1.73
2.55	1.68
2.67	1.65
2.69	1.64
2.84	1.66
2.86	1.72

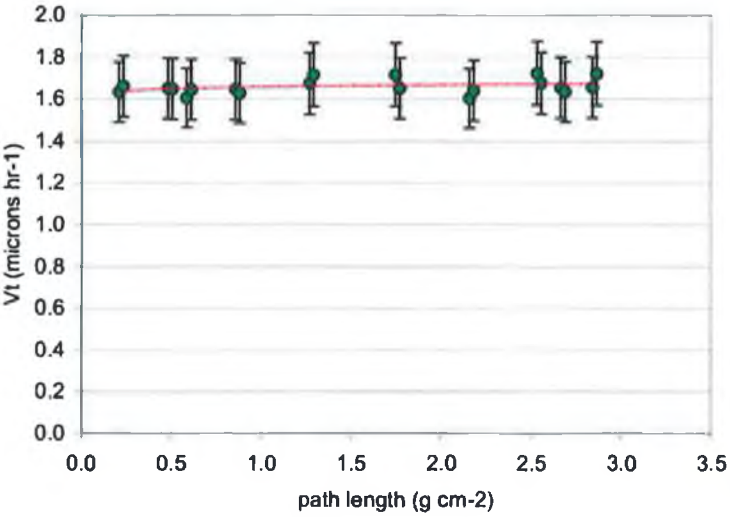

Event	196 / 12
Assigned Z	89.6
error (+)	1.7
error (-)	1.3
Etch Time (hrs)	46
Mean V_G (μm hr^{-1})	0.137
TERM variation	-6.3%

pathlength (g cm^{-2})	V_T (microns hr^{-1})
0.26	1.69
0.29	1.69
0.49	1.63
0.51	1.71
0.64	1.54
0.66	1.55
0.97	1.67
1.00	1.68
1.34	1.84
1.37	1.69
1.90	1.76
1.92	1.77
2.38	1.86
2.41	1.82
2.75	1.69
2.78	1.72
2.90	1.64
2.92	1.74
3.05	1.76
3.07	1.82

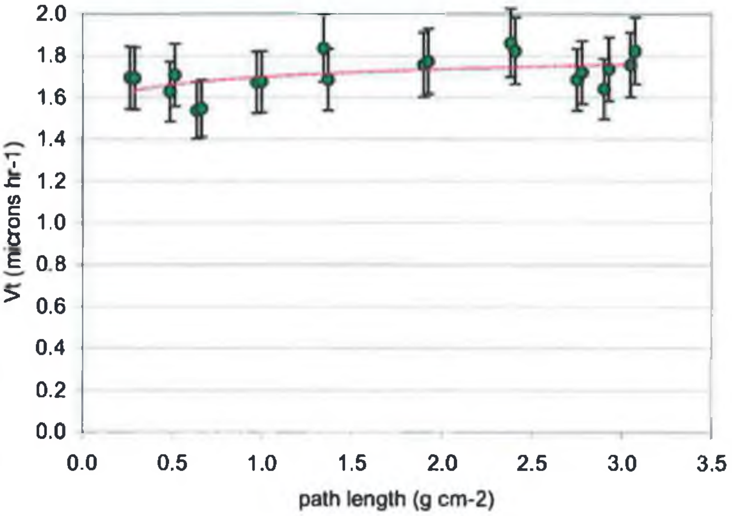

Event	196 / 18
Assigned Z	88.2
error (+)	0.7
error (-)	1.6
Etch Time (hrs)	72.5
Mean V_G (μm hr^{-1})	0.142
TERM variation	-7.8%

pathlength (g cm^{-2})	V_T (microns hr^{-1})
0.26	1.16
0.28	1.20
0.47	1.14
0.50	1.19
0.62	1.20
0.64	1.31
0.94	1.17
0.97	1.24
1.31	1.18
1.33	1.19
1.85	1.23
1.87	1.24
2.32	1.18
2.34	1.21
2.68	1.17
2.70	1.23
2.82	1.15
2.85	1.22
2.97	1.17
2.99	1.23

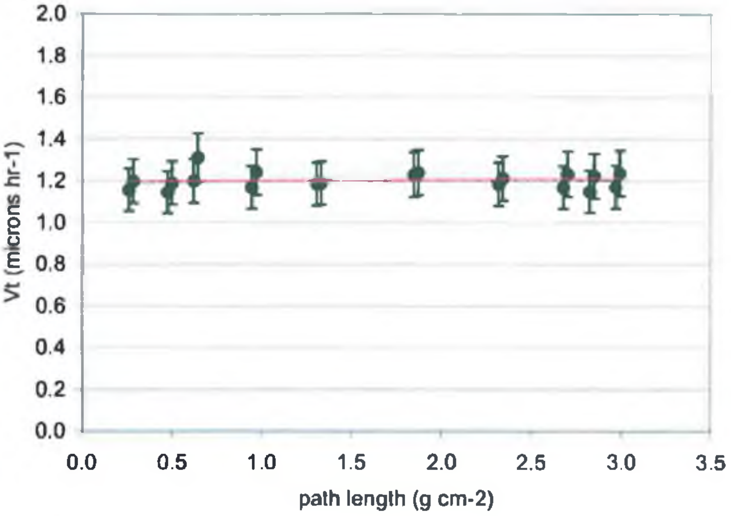

Event	29 / 13	pathlength	V_T
Assigned Z	93.6	(g cm^{-2})	(microns hr^{-1})
error (+)	0.9	2.07	1.84
error (-)	1.2	2.09	1.78
		2.62	1.85
Etch Time (hrs)	42	2.65	1.73
Mean V_G (μm hr^{-1})	0.165	3.22	1.90
TERM variation	1.0%	3.24	2.03
		3.70	1.88
		3.72	1.93
		3.81	1.89
		3.83	1.67
		4.03	1.98
		4.05	2.00
		4.17	1.76
		4.19	1.81
		4.31	1.83
		4.34	1.82
		4.46	1.86
		4.48	1.79
		4.64	1.94
		4.66	1.89

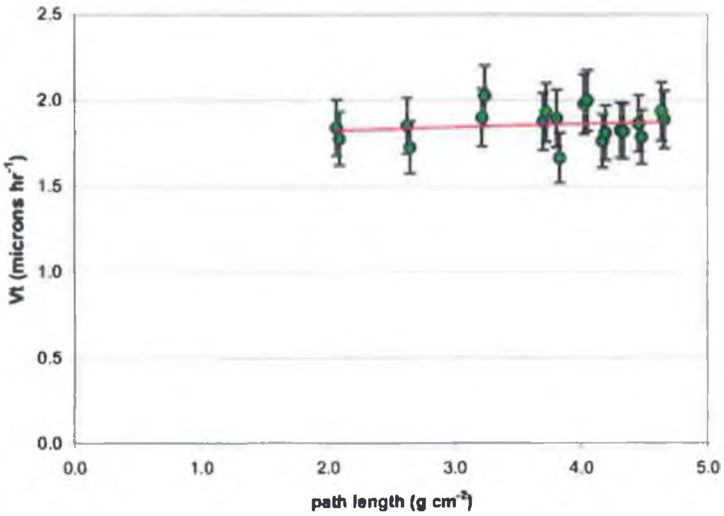

Event	29 / 19	pathlength	V_T
Assigned Z	89.8	(g cm^{-2})	(microns hr^{-1})
error (+)	1.2	1.74	1.33
error (-)	1.5	1.77	1.21
		2.21	1.37
Etch Time (hrs)	42	2.23	1.43
Mean V_G (μm hr^{-1})	0.165	2.71	1.44
TERM variation	1.0%	2.73	1.55
		3.12	1.41
		3.14	1.47
		3.21	1.43
		3.23	1.28
		3.39	1.50
		3.41	1.49
		3.51	1.46
		3.54	1.40
		3.64	1.41
		3.66	1.29
		3.76	1.37
		3.78	1.39
		3.91	1.46
		3.93	1.43

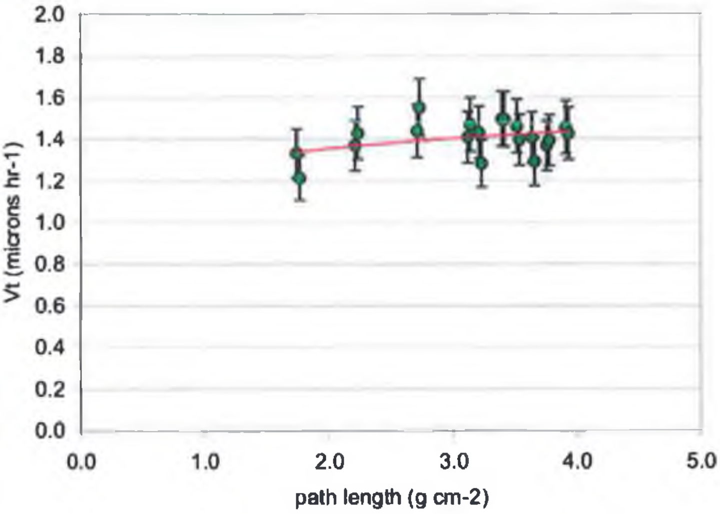

Event	40 / 9	pathlength	V_T
Assigned Z	88	(g cm^{-2})	(microns hr^{-1})
error (+)	1.1	2.11	1.58
error (-)	1.0	2.13	1.71
		2.55	1.63
Etch Time (hrs)	72	2.57	1.66
Mean V_G (μm hr^{-1})	0.158	3.14	1.64
TERM variation	4.8%	3.16	1.69
		3.21	1.61
		3.23	1.58
		3.76	1.53
		3.79	1.58
		4.18	1.52
		4.20	1.54
		4.22	1.56
		4.24	1.58
		4.30	1.48
		4.32	1.56
		4.53	1.55
		4.55	1.55

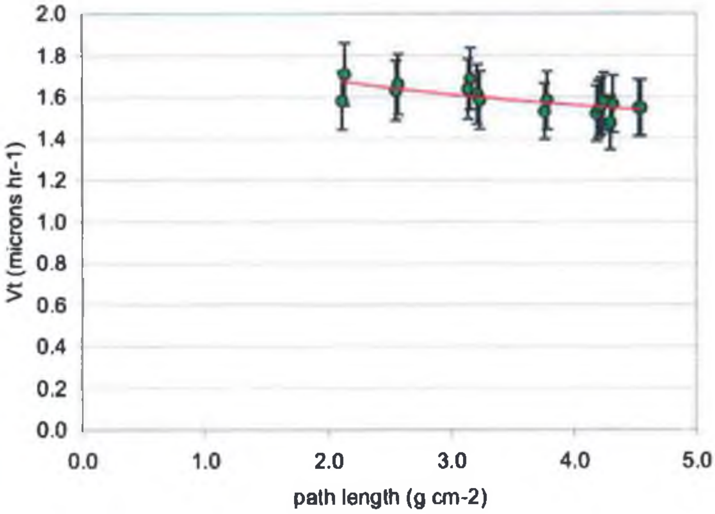

Event	79 / 6	pathlength	V_T
Assigned Z	90.4	(g cm^{-2})	(microns hr^{-1})
error (+)	0.8	0.15	1.36
error (-)	1.0	0.17	1.37
		0.29	1.33
Etch Time (hrs)	72	0.32	1.34
Mean V_0 (μm hr^{-1})	0.158	1.19	1.47
TERM variation	4.8%	1.22	1.39
		3.34	1.41
		3.37	1.38
		4.05	1.41
		4.08	1.44
		5.38	1.35
		5.41	1.33
		5.75	1.33
		5.78	1.36
		5.89	1.41
		5.92	1.41
		5.98	1.40
		6.01	1.40
		6.07	1.49
		6.10	1.42

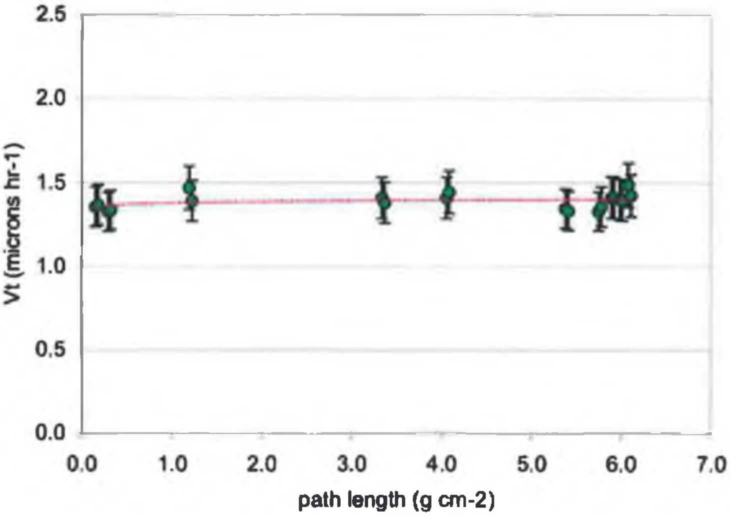

Event	87 / 1	pathlength	V_T
Assigned Z	92.2	(g cm^{-2})	(microns hr^{-1})
error (+)	1.3	0.05	1.85
error (-)	1.0	0.08	1.93
		0.14	1.70
Etch Time (hrs)	68	0.17	1.79
Mean V_0 (μm hr^{-1})	0.144	0.32	1.65
TERM variation	-13.4%	0.35	1.84
		2.31	1.82
		2.34	1.85
		3.03	1.72
		3.06	1.95
		3.67	1.76
		3.70	1.91
		4.88	1.74
		4.91	1.81
		5.64	1.66
		5.67	1.75
		5.82	1.56
		5.85	1.74
		5.86	1.64
		5.89	1.84

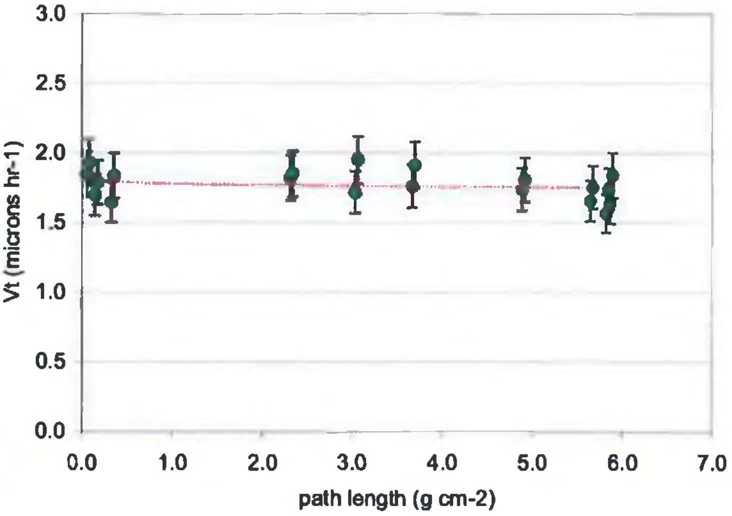

Event	142 / 11	pathlength	V_T
Assigned Z	91.5	(g cm^{-2})	(microns hr^{-1})
error (+)	1.3	0.07	1.72
error (-)	1.1	0.09	1.76
		0.17	1.84
Etch Time (hrs)	42	0.19	1.79
Mean V_0 (μm hr^{-1})	0.144	0.73	1.85
TERM variation	6.7%	0.75	1.79
		1.23	1.72
		1.25	1.73
		1.74	1.83
		1.76	1.83
		2.21	1.84
		2.23	1.85
		3.37	1.93
		3.39	1.92
		3.79	1.98
		3.81	1.98
		4.08	2.03
		4.10	2.04
		4.21	1.86
		4.23	1.84

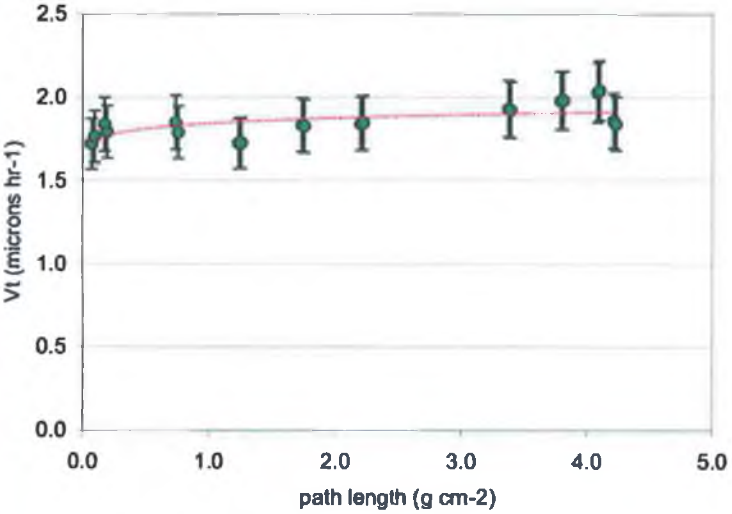

Event	87 / 9	pathlength	V_T
Assigned Z	90.3	(g cm^{-2})	(microns hr^{-1})
error (+)	0.9	0.04	1.50
error (-)	1.4	0.05	1.52
		0.10	1.56
Etch Time (hrs)	68	0.12	1.45
Mean V_G (μm hr^{-1})	0.144	0.22	1.41
TERM variation	-13.4%	0.24	1.40
		1.59	1.50
		1.61	1.39
		2.09	1.53
		2.10	1.45
		2.52	1.49
		2.54	1.47
		3.36	1.42
		3.38	1.48
		3.88	1.45
		3.90	1.50
		4.01	1.44
		4.02	1.44
		4.04	1.48
		4.06	1.34

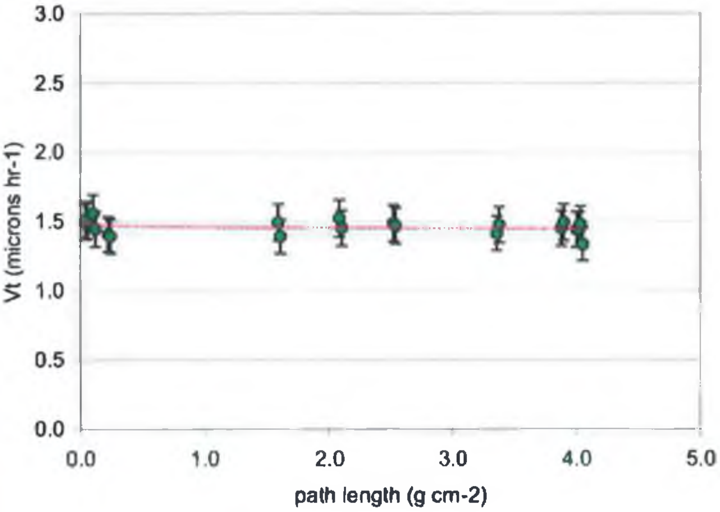

Event	105 / 15	pathlength	V_T
Assigned Z	91.2	(g cm^{-2})	(microns hr^{-1})
error (+)	1.3	0.04	1.57
error (-)	1.2	0.06	1.71
		3.15	1.64
Etch Time (hrs)	42	3.17	1.81
Mean V_G (μm hr^{-1})	0.165	3.21	1.59
TERM variation	1.0%	3.23	1.66
		3.28	1.66
		3.30	1.64
		3.41	1.61
		3.43	1.72
		3.66	1.57
		3.68	1.84
		3.73	1.58
		3.75	1.66
		3.89	1.64
		3.91	1.84
		4.21	1.60
		4.23	1.73
		4.24	1.66
		4.26	1.75

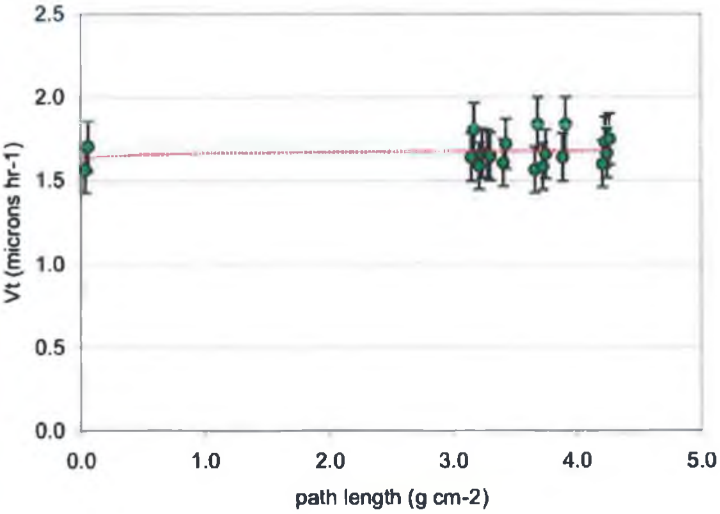

Event	106 / 2	pathlength	V_T
Assigned Z	87.8	(g cm^{-2})	(microns hr^{-1})
error (+)	0.8	1.19	1.98
error (-)	0.9	1.21	1.97
		1.63	2.20
Etch Time (hrs)	24	1.66	1.98
Mean V_G (μm hr^{-1})	0.160	2.16	1.98
TERM variation	-6.0%	2.17	2.03
		2.63	2.35
		2.65	2.31
		3.11	2.59
		3.13	2.40
		3.24	2.57
		3.26	2.68
		3.46	2.39
		3.48	2.38
		3.55	2.46
		3.58	2.39
		3.84	2.43
		3.86	2.48
		3.93	2.57
		3.95	2.52
		3.99	2.82
		4.02	2.91
		4.12	2.90
		4.14	2.77

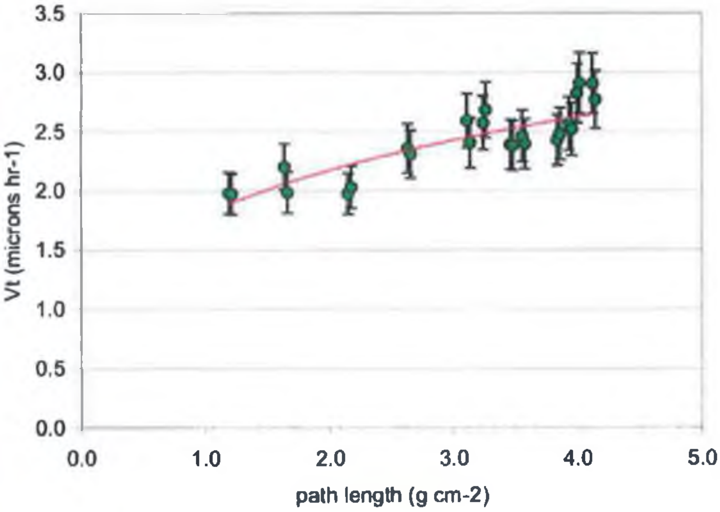

Event	146 / 10	pathlength	V_T
Assigned Z	89.1	(g cm^{-2})	(microns hr^{-1})
error (+)	1.2	3.18	1.57
error (-)	1.2	3.20	1.58
		3.22	1.64
Etch Time (hrs)	62	3.24	1.59
Mean V_G (μm hr^{-1})	0.152	3.77	1.61
TERM variation	3.3%	3.79	1.61
		3.84	1.60
		3.86	1.73
		3.88	1.62
		3.90	1.65
		4.03	1.70
		4.05	1.91
		4.10	1.58
		4.12	1.57
		4.18	1.61
		4.20	1.60
		4.33	1.67
		4.35	1.60
		4.40	1.71
		4.42	1.66

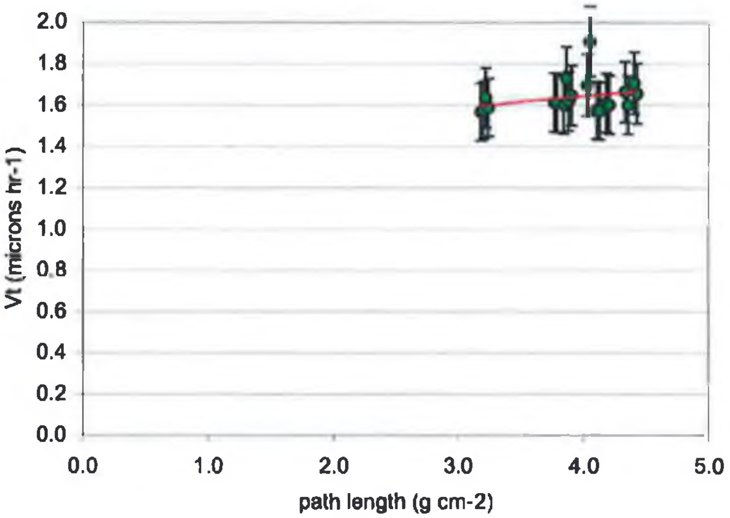

Event	175 / 8	pathlength	V_T
Assigned Z	93	(g cm^{-2})	(microns hr^{-1})
error (+)	0.9	0.19	1.85
error (-)	0.9	0.23	1.78
		3.37	1.93
Etch Time (hrs)	72	3.41	2.03
Mean V_G (μm hr^{-1})	0.158	4.35	1.87
TERM variation	4.8%	4.39	2.01
		4.47	1.76
		4.51	1.84
		4.53	1.76
		4.57	1.84
		5.73	2.01
		5.76	1.98
		5.79	1.88
		5.82	1.91
		5.85	1.82
		5.88	1.91
		5.97	1.99
		6.00	2.04
		7.28	2.02
		7.31	1.94

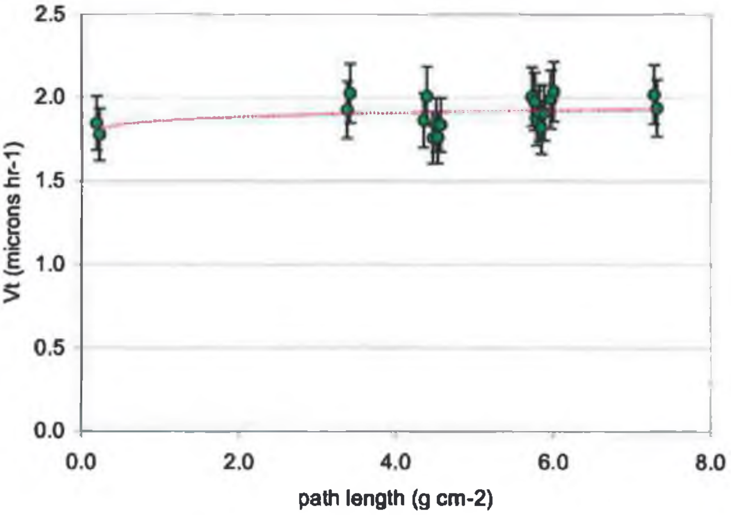

Event	209 / 3	pathlength	V_T
Assigned Z	90.3	(g cm^{-2})	(microns hr^{-1})
error (+)	0.7	0.78	1.31
error (-)	2.0	0.80	1.35
		0.85	1.35
Etch Time (hrs)	62	0.86	1.45
Mean V_G (μm hr^{-1})	0.152	1.69	1.18
TERM variation	3.3%	1.71	1.20
		1.91	1.23
		1.93	1.33
		2.04	1.37
		2.06	1.44
		2.34	1.21
		2.36	1.16
		2.59	1.27
		2.61	1.30
		2.68	1.32
		2.70	1.31
		2.72	1.41
		2.73	1.40
		2.87	1.33
		2.89	1.39

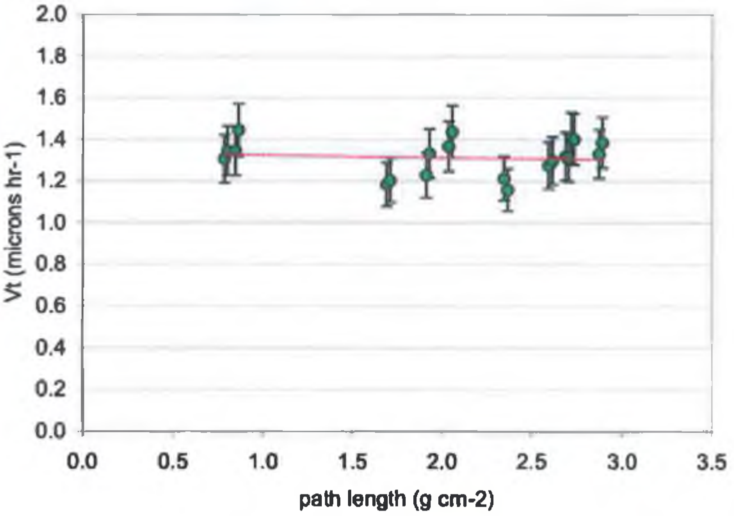

Event	127 / 12	pathlength	V_T
Assigned Z	90.2	(g cm^{-2})	(microns hr^{-1})
error (+)	1.1	3.32	1.54
error (-)	1.0	3.35	1.63
		4.91	1.42
Etch Time (hrs)	62	4.94	1.60
Mean V_G (μm hr^{-1})	0.152	5.05	1.45
TERM variation	3.3%	5.09	1.56
		5.25	1.49
		5.29	1.60
		5.65	1.56
		5.68	1.60
		5.69	1.52
		5.73	1.59
		5.84	1.52
		5.88	1.64
		6.14	1.43
		6.17	1.54
		6.58	1.62
		6.61	1.64

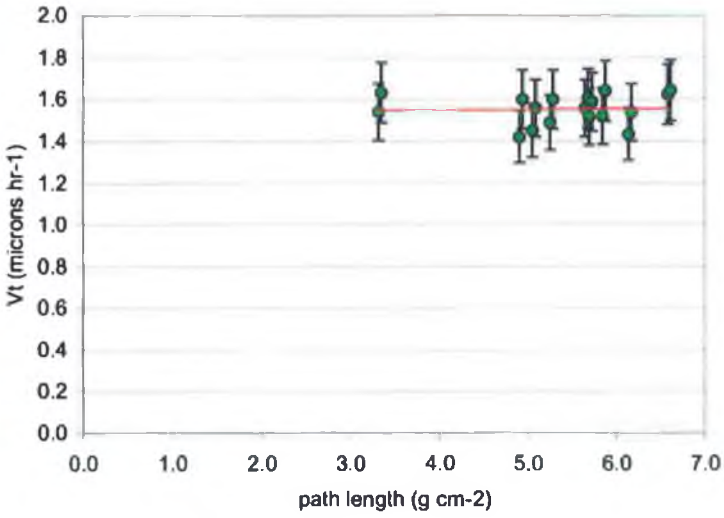

Event	127 / 18	pathlength	V_T
Assigned Z	91.7	(g cm^{-2})	(microns hr^{-1})
error (+)	1.0	2.26	1.68
error (-)	1.2	2.27	1.64
		3.33	1.60
Etch Time (hrs)	62	3.35	1.73
Mean V_G (μm hr^{-1})	0.152	3.43	1.62
TERM variation	3.3%	3.45	1.58
		3.56	1.67
		3.58	1.65
		3.83	1.70
		3.85	1.66
		3.87	1.64
		3.88	1.65
		3.97	1.64
		3.99	1.61
		4.17	1.52
		4.19	1.61
		4.47	1.63
		4.49	1.70

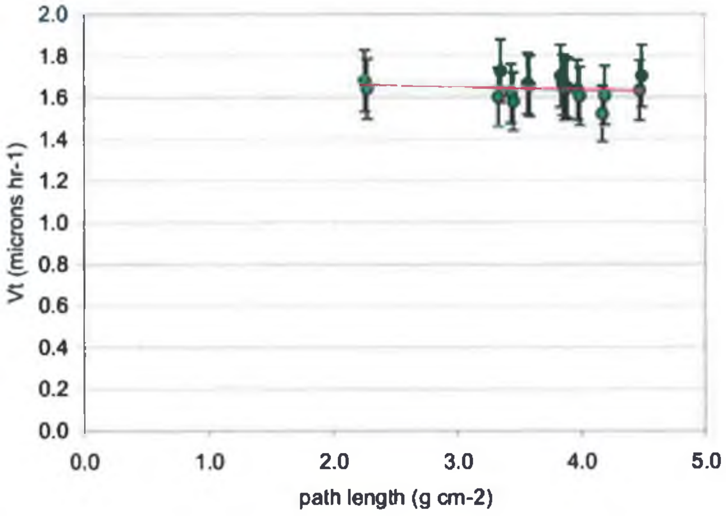

Event	130 / 16	pathlength	V_T
Assigned Z	87.7	(g cm^{-2})	(microns hr^{-1})
error (+)	0.9	0.11	1.22
error (-)	1.3	0.13	1.21
		0.17	1.19
Etch Time (hrs)	72	0.19	1.24
Mean V_G (μm hr^{-1})	0.161	0.24	1.20
TERM variation	2.6%	0.26	1.16
		0.77	1.19
		0.79	1.22
		1.29	1.27
		1.31	1.28
		1.85	1.19
		1.87	1.21
		2.87	1.16
		2.89	1.20
		3.49	1.18
		3.51	1.18
		3.69	1.20
		3.71	1.16
		4.27	1.19
		4.29	1.20

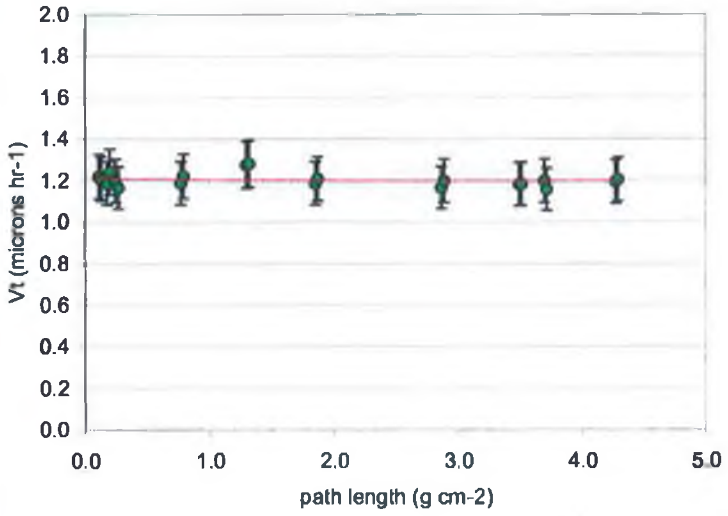

Event	23 / 18	pathlength	V_T
Assigned Z	91.9	(g cm^{-2})	(microns hr^{-1})
error (+)	0.8	0.13	2.01
error (-)	0.7	0.15	2.12
		0.21	1.98
Etch Time (hrs)	48	0.23	2.08
Mean V_G (µm hr^{-1})	0.152	0.29	2.05
TERM variation	-	0.31	2.09
		0.97	2.06
		1.00	2.26
		1.05	2.13
		1.08	2.45
		1.53	2.11
		1.56	2.24
		2.78	2.29
		2.80	2.35
		2.90	2.36
		2.92	2.40
		3.42	2.36
		3.45	2.51
		3.50	2.44
		3.52	2.52
		4.07	2.56
		4.09	2.66
		4.46	2.45
		4.49	2.52
		4.54	2.51
		4.57	2.63
		4.58	2.46
		4.61	2.63
		4.67	2.66
		4.69	2.69
		4.75	2.56
		4.77	2.72
		4.83	2.73
		4.85	2.89
		4.87	2.60
		4.89	2.50
		4.95	2.55
		4.97	2.65
		5.03	2.50
		5.05	2.55

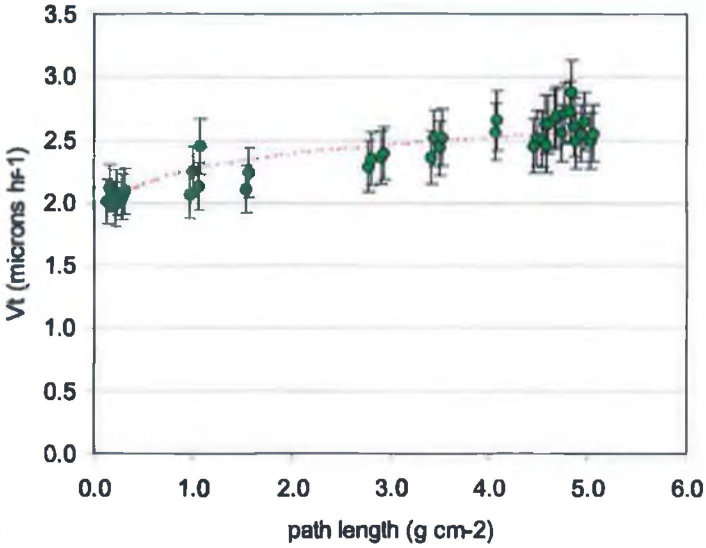

Appendix C: UHCRE Stack Locations

Tray Location	Tray Number	Cylinder Number	Stack Labels			
A2	A29	43	039A	037A	035A	036A
		50	153B	204C	186C	152B
		40	034A	033A	032A	031A
A4	A18	36	141A	209A	142A	138A
		04	169B	195C	194C	168B
		21	100A	102A	095A	099A
A10	A6	22	085A	084A	082A	083A
		07	165B	206C	200C	164B
		23	075A	076A	079A	081A
B5	A13	29	030A	028A	027A	029A
		11	151B	185C	184C	150B
		30	026A	025A	023A	024A
B7	A22	38	086A	087A	088A	093A
		39	166B	198C	199C	167B
		37	096A	089A	090A	094A
C5	A15	31	019A	020A	021A	022A
		12	148B	183C	203C	149B
		32	015A	016A	017A	018A
C6	A11	25	146A	064A	058A	055A
		09	157B	217C	205C	159B
		24	050A	061A	062A	054A
C8	A27	46	145A	135A	134A	143A
		56	181B	220C	218C	179B
		47	147A	212A	211A	144A
C11	A20	51	112A	115A	116A	118A
		41	172B	213C	214C	174B
		48	110A	113A	114A	111A
D1	A17	06	108A	106A	107A	109A
		01	170B	201C	207C	171B
		05	101A	103A	105A	104A
D5	A16	08	047A	051A	049A	046A
		02	156B	197C	196C	155B
		14	052A	057A	056A	048A
D7	A26	45	066A	072A	068A	065A
		55	161B	219C	190C	160B
		44	060A	067A	063A	059A
D11	A5	57	133A	131A	130A	132A
		42	177B	004C	216C	176B
		52	129A	128A	127A	125A
E2	A21	17	124A	126A	123A	122A
		03	175B	215C	202C	173B
		53	121A	120A	117A	119A
E10	A24	54	080A	078A	077A	073A
		13	163B	193C	192C	162B
		34	071A	074A	070A	069A
F4	A23	27	043A	042A	053A	044A
		10	154B	187C	188C	158B
		26	040A	038A	045A	041A

Appendix D: UHCRE Tray Locations

Table C.1 Modal temperatures of UHCRE experimental trays during the LDEF mission.

Tray	*T* (°C)	Tray	*T* (°C)	Tray	*T* (°C)	Tray	*T* (°C)
A2	-20	B7	-25	C11	-24	D11	-25
A4	-17	C5	-24	D1	-28	E2	-24
A10	-17	C6	-27	D5	-25	E10	-21
B5	-24	C8	-22	D7	-27	F4	-19